Alexander Steiner, BSc

Magnetic Tuning of Nanoporous Palladium by Surface Charging: Influence of Electrolyte and of Coarsening

MASTER'S THESIS

to achieve the university degree of

Diplom-Ingenieur

Master's degree programme: Technical Physics

submitted to

Graz University of Technology

Supervisor

Univ.-Prof. Dipl.-Phys. Dr.rer.nat. Roland Würschum

Institute of Materials Physics

Graz, February 2020

Affidavit

I declare that I have authored this thesis independently, that I have not used other than the declared sources/resources, and that I have explicitly marked all material which has been quoted either literally or by content from the used sources. The text document uploaded to TUGRAZonline is identical to the present master‘s thesis.

Date	Signature

Abstract

Voltage-induced manipulation of magnetic properties has been a topic of increasing interest over the last years. Within this work, nanoporous Pd samples were produced by electrochemical dealloying and were investigated with focus on the modification of their magnetic properties upon a surface charging process. Due to its unique magnetic properties and its high surface area, nanoporous Pd represents a promising material, suitable for magnetisation-altering charging applications.

The ambition of this work, was the study of the modification of magnetic properties of nanoporous Pd(Co) upon surface charging and the influence of electrolytes and of thermal coarsening. During the dealloying process, a CoPd alloy (75:25 at%) is decomposed, by the dissolution of the lesser noble element Co, to a nanoporous Pd structure with residual Co content. To study the influence of the nanoporous structure, thermal treatment methods were performed. Samples were annealed to, each 373 K, 573 K, 773 K, and 973 K. Additionally, an unannealed sample was investigated. An electrochemical cell was built, in which the different samples were charged in two different electrolytes by means of cyclic voltammetry. As electrolytes an organic one, $LiPF_6$ in EC/EMC (1:1), and an aqueous one, KOH were chosen. The charging was performed in the pseudocapacitive regime. Furthermore, an additional potential range in KOH, which is known for hydrogen adsorption, was inspected. Thermal coarsening resulted in a larger ligament size and a consequently lower surface area. Additionally, it changed the Co distribution within the sample, which affected magnetic properties. The coarsening procedure influenced the charging in the electrolytes differently. While in $LiPF_6$/EC/EMC coarser samples exhibited a higher change in relative magnetisation, but a lower absolute change of magnetisation, a charging in KOH showed no clear dependence on the coarsening. In $LiPF_6$/EC/EMC, the highest relative change was about 0.65 % and was reached by the coarsest sample. The largest relative change (about 0.64 %)

in the pseudocapacitive potential range in KOH was obtained by lesser coarse samples. The highest relative magnetisation change in general, was reached by a charging in the hydrogen-adsorption regime, which achieved a top value of about 4.6 %. The results were discussed in terms of different magnetoelectric mechanisms, i.e. band filling, chemical surface reactions, variation of the magnetocrystalline anisotropy, and magnetoelastic effects.

Contents

Chapter 1

Introduction

Modification of magnetic properties by means of electric fields is a known subject to the scientific community and was the centre of interest of several works[1–7]. Besides its general scientific interest, the control of magnetisation without flowing currents or any external magnetic field would be an energy-efficient way to store magnetic information. Thereby, an energy loss due to heat dissipation, by necessary high currents to generate magnetic fields, might become a thing of the past.

Since Pd has a maximum of the density of states near the Fermi level, it is almost ferromagnetic. This gives rise to the consideration, if it can be influenced strong enough, by changing the electron density, to change its magnetic properties. The basic idea is to charge the surface of Pd by an applied voltage in an electrolyte to modify the density of states and thus alter the magnetisation of the material. This inevitably poses two questions: How strong one can influence the magnetisation in a reversible way, and which is the underlying process of this effect?

To investigate these questions, the material has to fulfill other requirements as well, rather than the magnetic state. Because of effective screening within metals, an electric field does not propagate far into the material and a high surface area becomes an essential feature of possible materials. This gives the consideration of using nanoscaled materials, such as nanoparticles or nanocrystalline, or nanoporous (np), structures. These materials have a very high surface-to-volume ratio and thus fulfill the requirements of a large surface. Due to the possibility of electrochemical dealloying a CoPd alloy, a nanoporous Pd structure can be

obtained[8]. The high surface area of this structure and the interesting magnetic properties of Pd, as described before, make Pd to a promising material for observing alterations of magnetic properties by charging experiments.

The aim of this thesis is the systematic study of the magnetic tuning of np-PdCo via electrochemical bias with a special focus on the influence of a surface rearrangement by thermal coarsening. Furthermore, understanding the influence of electrolyte and charging in different electrochemical regimes is of central interest in this work. These investigations promise insight in underlying mechanisms of charging-induced variation of magnetic properties.

Chapter 2

Fundamentals

2.1 Fundamentals of Electrochemistry

Electrochemistry studies the relation between electrical and chemical processes at the interface of an electrode and a electrolyte[9]. The electrode can be any electron-conductive material, usually metal, and the electrolyte can be an aqueous or organic solution, in which the ions are dissolved, or an ionic liquid, which consists of ions. Solid electrolytes are also a possibility. Since a difference in chemical potential μ occurs, the system compensates this difference and equalises the energy levels. If $\mu_{\text{electrode}} > \mu_{\text{electrolyte}}$, the electrode is negatively and the electrolyte positively charged, free electrons from the electrode are transferred in the electrolyte where the conducting species take up these electrons (reduction) to match the chemical potential. Here the electrode serve as an electron donor. If $\mu_{\text{electrode}} < \mu_{\text{electrolyte}}$, the electrode is positively charged and the electrolyte negatively. The electrolyte oxidises and gives electrons to the electrode. In this case the electrode acts like an acceptor. Since the electrolyte is an ionic conductor, in opposite to the electrode, which is a electronic conductor, there are always chemical reactions to provide electron transfer. Due to charge conservation these reductions and oxidations take always place pairwise. Reduction and oxidation are known as electrochemical half reactions. With a suitable applied voltage, the charge carrier transfer across the interface can be avoided. In this case, the applied potential difference induces only a charge carrier movement in both, metal and electrolyte, and the electrode-electrolyte interface acts like a capacitor. This behaviour in a certain voltage range, without

chemical reactions, is called capacitive or pseudocapacitive behaviour.

The potential difference between the electrode and electrolyte is known as the Galvani potential. Since there is no easy way to measure this potential, a standard hydrogen electrode (SHE) is typically used as a reference potential. The SHE, which has actually a potential of $4.44\,\mathrm{V}$[9,10] with respect to the vacuum level, is defined arbitrarily as zero and corresponds to the half reaction $2\,\mathrm{H}^{+}_{(\mathrm{aq})} + 2\,\mathrm{e}^{-}_{(\mathrm{g})} \rightleftharpoons \mathrm{H}_{2(\mathrm{g})}$[9,10]. With the SHE the Galvani potential can be determined by the Nernst equation[9]:

$$E = E^0 + \frac{RT}{zF} \ln \frac{a_{\mathrm{ox}}}{a_{\mathrm{red}}} \,. \tag{2.1}$$

Here, E is the Galvani potential, E^0 is the standard Galvani potential difference, R the gas constant, T the temperature, z the number of transferred electrons, F is the Faraday constant and a_{ox} and a_{red} the activity of the oxidised and reduced species. An applied voltage to the electrode-electrolyte interface shifts the equilibrium and causes a charge transfer.

Usually electrolytes are good conductors but their conductivity still ranges several orders of magnitude below the conductivity of metals. The weaker conductivity is a consequence of the lower charge carrier concentration, which leads to a much wider charge carrier distribution in the electrolyte. This expanded space, consists of two differently sized zones of equal but opposite charge, is known as the electric double layer. The double layer acts like a capacitor with the length of the double layer extension. This layer extends usually from 5 to $20\,\text{Å}$ into the electrolyte, while in a metal the charges spread over a surface region of about $1\,\text{Å}$, known as the Thomas–Fermi screening length δ. The length of the charge carrier layer in the electrolyte depends on how much charge is needed to compensate the charge in the metal. This layer is referred to as the Helmholtz layer. The Helmholtz layer consists of specific adsorbents and weakly bound ions further away from the electron surface[9]. A simplified illustration is pictured in figure 2.1. Pure electrochemical double layer corresponds to a certain voltage range in which applied voltages do not cause chemical reactions nor a charge carrier transfer across the interface. In this voltage range only capacitive charging at the interface is responsible for currents, which are considered reversible.

The observed interface of interest is the one between the electrolyte and the working electrode (WE). In addition to this, a reference electrode (RF) is required, like the SHE, to measure

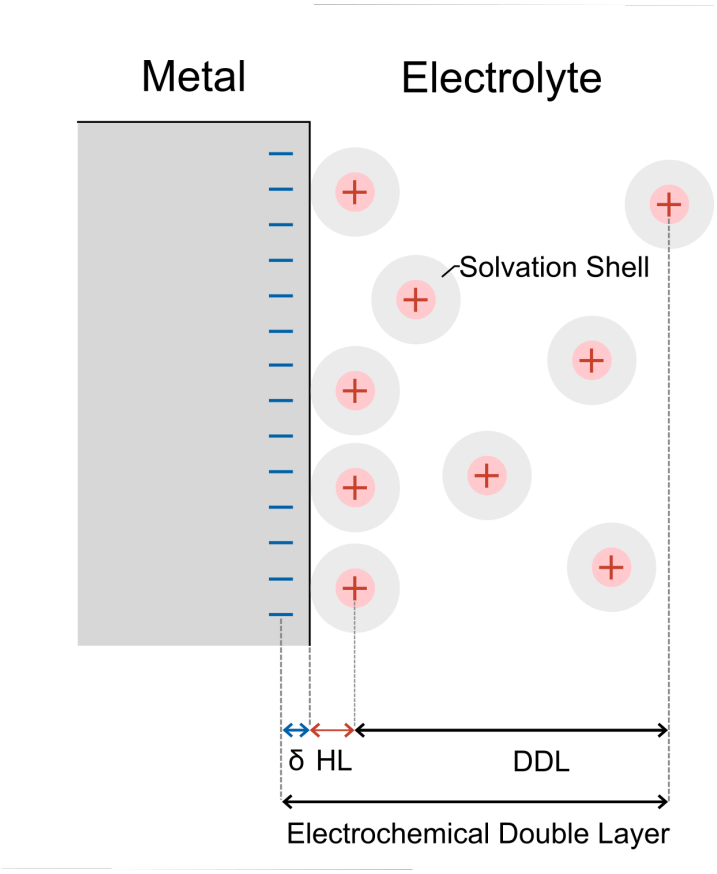

Figure 2.1: Illustrated schematics of the electrochemical double layer upon negative charging, whereas δ is the Thomas-Fermi screening length, HL the Helmholtz layer and DDL the diffuse double layer.

the correct potential of the WE. In practice the SHE is rarely used because of its hydrogen gas. Instead commercially secondary reference electrodes are used. These are electrodes for which the potential difference to the SHE is well known. One of the most commonly used reference electrodes is the Ag/AgCl electrode, which shows the half reaction:

$$\mathrm{Ag} + \mathrm{Cl}^- \rightleftharpoons \mathrm{AgCl} + \mathrm{e}^- . \tag{2.2}$$

Finally a third electrode closes the circuit to the WE. This is the counter electrode (CE), which enables a current flow due to an external potential. This system is called a three-electrode configuration and represents the typical construction of an electrochemical cell.

2.2 Cyclic Voltammetry

Cyclic voltammetry (CV) is an electrochemical technique in which a time-dependent voltage, between CE and WE, is applied. It is one of the most commonly used techniques in electrochemistry. The applied voltage increases linearly from a suitable chosen starting point to the upper limit and then decreases linearly until it reaches the lower limit. A suitable starting point means that the current at this potential is negligible small. This condition is satisfied near the open circuit potential U_{OCP}, which is the difference in electrical potential without a voltage applied. As the voltage reaches the starting point again, one cycle has been completed. This process can be repeated several times, dependent on how many cycles are needed. The voltage in dependence of time has a triangular like shape as seen in figure 2.2.

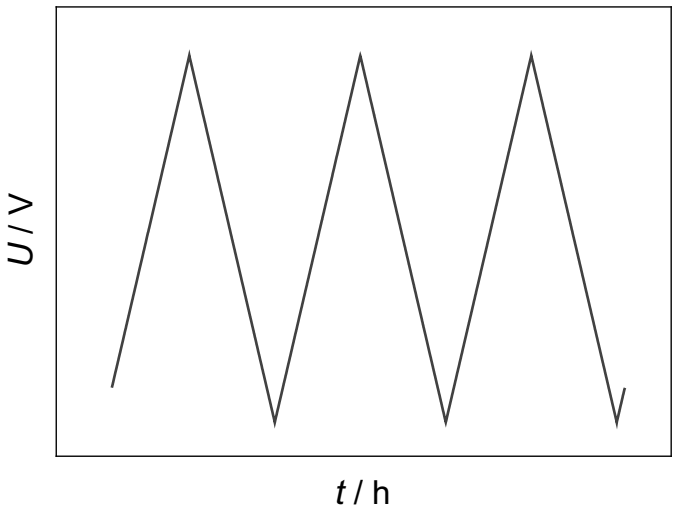

Figure 2.2: Three cycles of a voltage versus time curve for a typical CV measurement.

The slope of the curve represents the scan rate sr. It is stated as the increase in voltage per time ($\mathrm{mV\,s^{-1}}$) and also determines how much current will flow. Higher scan rates mean higher currents. In the double layer regime the current would be proportional to the scan rate ($I \propto sr$), and if chemical reactions occur, it is typically proportional to the square root of the scan rate ($I \propto \sqrt{sr}$)[11]. By measuring the current in dependence of the applied voltage, electrochemical processes within the applied voltage range can be studied. The shape of the voltammogram reflects the reactions at the electrode-electrolyte interface. A CV within the voltage range of the double layer regime shows no peaks and a rectangular shape, similar to the ideal capacitor. In reality the shape is only almost rectangular because of the ohmic

resistance of the double layer, as seen in figure 2.3.

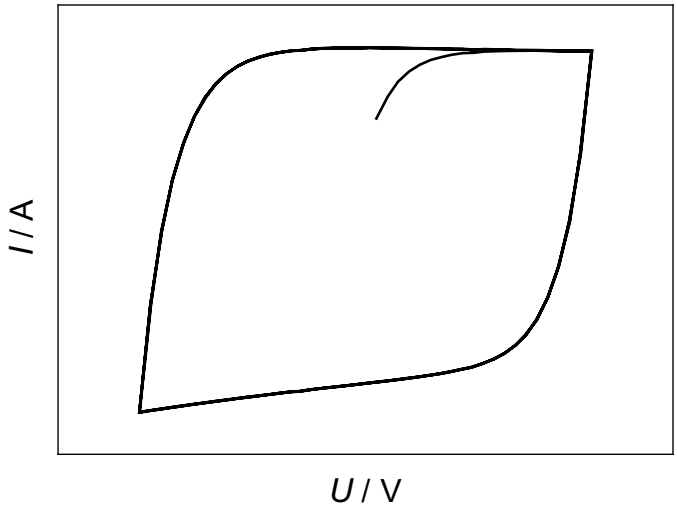

Figure 2.3: Current versus voltage curve in the double layer regime for a typical CV measurement with five cycles.

One cycle, which runs clockwise in time, can be split into an upper branch at positive currents, the anodic half cycle, and a lower branch at negative currents, known as the cathodic half cycle. If one would go to higher and lower voltage ranges, peaks would appear, each representing a certain chemical reaction. These peaks usually come in pairs while one peak is related to a specific reaction while the other is related to the reverse reaction of this specific reaction. If the distance between these peaks is lower than 57 mV at 298 K the reaction is considered as reversible[11].

2.3 Dealloying

Dealloying is a method to gain nanoporous materials in which one or more compounds can be chemically or electrochemically dissolved from an alloy. In electrochemical dealloying an alloy of different noble materials can be selectively separated by immersing it in an electrolyte and applying a potential, the dealloying voltage U_{d}. Due to the different electrochemical standard potential of the materials, in case of a binary alloy, the lesser noble component is dissolved, while the diffusivity of the other increases. The dealloying potential has to be sufficiently high enough to remove the atoms of the lesser noble species from high-coordination sites which leads to diffusion of the remaining noble species atoms from low to high concentration regions. Atom rearrangement of the more-noble component causes clustering of the more-

noble atoms and the exposition of more atoms to the electrolyte which lets the dealloying process continue. This leads to a formation of a nanoporous network with a drastically increased surface area and thus a high surface-to-volume ratio. If the diffusivity is not high enough, the surface covers with more and more noble species atoms and passivation hinders the process from continuing. A simulation of a dealloying process is displayed in figure 2.4.

A key quantity of nanoporous structures, which determines the amount of surface area, is the ligament size w. It is the mean diameter of these produced nanoscaled struts. Besides the dealloying voltage, the composition of the alloy, especially the melting temperature of the noble metal, and also the temperature during the dealloying process determines this property. A method which is able to modify this property via a solid state process is thermal coarsening[8]. It allows to control the ligament size from nanoscale to microns, dependent on the requirement. Upon heating the dealloyed sample, thermally activated diffusion changes the nanoporous structure. As a result of diffusion the ligament size grows and coarsens the whole structure, which leads to a higher surface. The diffusion causes also a redistribution of the internal residual atoms of the lesser noble alloy component. This leads to a homogenisation of the distribution of the lesser noble atom species and transports more of these atoms to the surface. This can also be seen in figure 2.4.

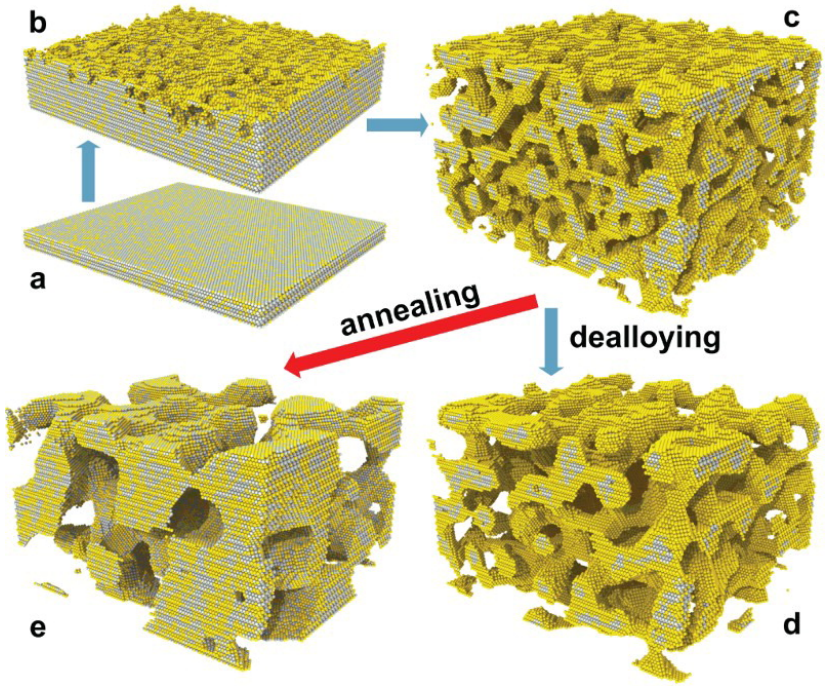

Figure 2.4: Schema of the dealloying and coarsening process on a AuAg alloy from kinetic Monte Carlo (KMC) simulations of Krekeler et al.[12]

2.4 Superparamagnetism

Superparamagnetism is a magnetic phenomenon which appears in sufficiently small ferromagnetic or ferrimagnetic particles. It expresses as the property, that at temperatures below the Curie temperature the ensemble of these particles show no macroscopic magnetisation if a, first turned on, magnetic field turns off. The decisive factors for superparamagnetism are the measurement time τ_{m}, which it takes to measure the magnetisation, the temperature T, the anisotropy constant K and, as mentioned, the size of the particles V.

While the magnetostatic energy of a particle is proportional to the volume of the particle, the domain wall energy increases proportionally to the surface. This means that if a particle is small enough, a critical size is reached where the formation of a domain wall is not energetically favourable anymore and the particle consists of only one single magnetic domain. Single domain particles have in the most cases only two stable orientations, which lie antiparallel to each other. They are called the easy axes. The energy needed to flip the magnetic moment out of its easy axis is called the anisotropy energy E_{A} which is directly proportional to the volume. Thus the smaller the particle, the higher is the probability for the particles to flip their magnetic moments out of favourable direction.

Up on here a second factor becomes important, i.e., the temperature. In an assembly of very small particles and sufficiently high temperatures, the anisotropy energy may be in range of the thermal energy. Since enough energy is provided, the probability for the spins to flip is enhanced.

Finally a third factor comes in consideration which is the measurement time. If the measurement time is longer than a certain time period, called the Néel relaxation time τ_{N}, a particle can flip its spins during measurement which gives a different result depending on how much time the measurement takes. The Néel relaxation time is the average duration between two flips of a particle. If the measurement time is much longer than the Néel relaxation time ($\tau_{\mathrm{m}} >> \tau_{\mathrm{N}}$), a particle flips its spins multiple times during measurement. In an assembly of particles, the net magnetisation is on average zero, which results in paramagnetic behaviour.

With this knowledge a critical temperature for a certain measurement time and particle size can be defined above which the thermal energy is sufficient high enough to flip the orientation. This temperature is known as the blocking temperature T_{B}. Above, the spins of the particles flip multiple times and appear paramagnetic in the measurement time and below they are locked in their spin state, which is called blocked. Blocked particles behave ferromagnetically. A relation between the size of the particle, the anisotropy energy and the blocking temperature is given by:

$$E_{\mathrm{A}} = KV = 25 k_{\mathrm{B}} T_{\mathrm{B}} \,. \tag{2.3}$$

Here, K is the anisotropy constant, V the volume, k_{B} the Boltzmann constant and T_{B} the blocking temperature. For both regimes, the superparamagnetic and the blocked, the magnetic moment, m_{SPM} and m_{B}, can be defined via:

$$m_{\mathrm{SPM}} = \frac{\mu_0 {M_{\mathrm{S}}}^2 V^2 H}{3 K_{\mathrm{B}} T} \,, \tag{2.4}$$

and

$$m_{\mathrm{B}} = \frac{\mu_0 {M_{\mathrm{S}}}^2 V H}{3K}\,, \tag{2.5}$$

where μ_0 denotes the permeability in vacuum, M_{S} the saturation magnetisation and T the temperature.

2.4.1 Zero Field Cooling and Field Cooling

Zero Field Cooling (ZFC) and Field Cooling (FC) are measurement techniques which are used to investigate time-dependent effects of magnetic properties. They are very useful to determine the temperature range in which systems are irreversible. Irreversibility is indicated by the bifurcation of the ZFC and FC curves. This happens for sufficiently small particles, as their anisotropy energy E_{A} according to equation 2.3 is in the range of thermal energy. The Néel relaxation time τ_{N}:

$$\frac{1}{\tau_{\mathrm{N}}} = \frac{1}{\tau_0} \exp\left(-\frac{KV}{k_{\mathrm{B}}T}\right), \tag{2.6}$$

which is the time in which a particle flips its spins successfully, scales with the volume and thus, with the power of three of the diameter. If the particles are sufficiently large, the Néel relaxation time becomes so large that the system is irreversible which manifests itself as ferromagnetism. The irreversible regime lies in the temperature range below the bifurcation of the ZFC and FC curves, while above the the system is reversible. In equation 2.6, the time between two attempts to flip the particle moments is τ_0 and $\frac{1}{\tau_0}$ is the attempt frequency.

ZFC and FC curves consist of magnetic moment measurements in dependence of temperature. During ZFC measurements, the sample is cooled down to a certain low temperature (4.2 K, in this work), while no magnetic field H is applied ($\mu_0 H = 0$). Due to cooling, the magnetic state at room temperature "freezes" and the atomic magnetic moments get locked in their orientation. Then, a magnetic field is applied ($\mu_0 H = 5\,\mathrm{mT}$, in this work) and the sample is annealed up to a certain temperature (here, 300 K). During annealing, the magnetic moment is measured as a function of temperature. A typical ZFC curve of a ferromagnetic nanoparticle is shown in figure 2.5. For a ferromagnetic material the magnetic moment in the ZFC curve will rise up to a certain point and then decreases with increasing

temperature. This is because more and more atomic magnetic moments are thermally activated and flip their orientation in the field direction. The developing peak can be seen as the blocking temperature. For the FC curve, which is measured directly after the ZFC curve, sample is cooled down to the lower temperature limit. At the same applied field, during the cooling, the magnetic moment as a function of temperature is measured. A typical FC curve for a ferromagnetic nanoparticle can be seen in figure 2.5. As the sample cools down, thermal energy decreases and atomic magnetic moments begin to flip progressively in their favourable direction (influenced by the applied field) and the magnetic moment increases.

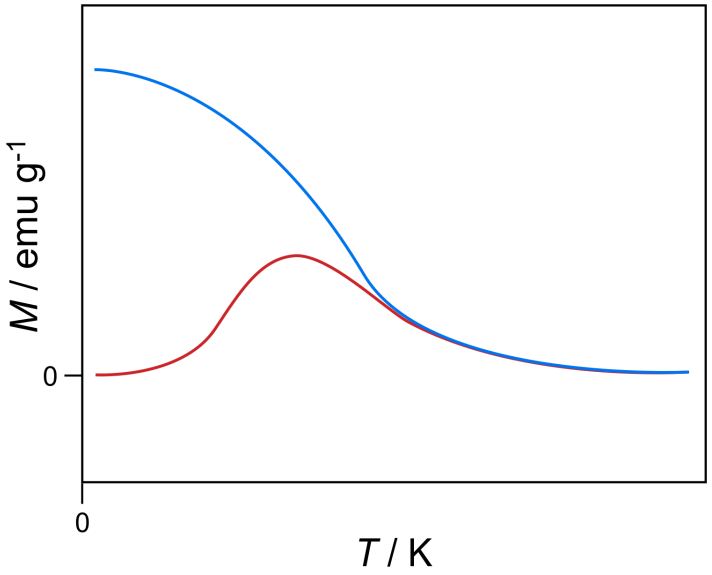

Figure 2.5: Typical curves for ZFC (red) and FC (blue) measurements of ferromagnetic nanoparticles.

2.5 Magnetism in the Cobalt-Palladium System

In this work the material for tuning was chosen to be a palladium-cobalt alloy. These elements were used because of their magnetic properties. Cobalt is ferromagnetic at room temperature, while the susceptibility of palladium is easily influenced because of it's Fermi level, which lies close to the maximum of the density of states[13].

In a cobalt-palladium alloy the magnetic interaction between the atoms is described by the Ruderman–Kittel–Kasuya–Yosida exchange (RKKY exchange). This interaction provides the coupling of localised moments over relatively large distances (in order of nanometers) and is a consequence of the wave nature of the conduction electrons. The RKKY interactions is transmitted via the conduction electrons. When these quasi "free" electrons are scattered at an atom, a rearrangement of these electrons occur in order to minimise the caused disturbance. This leads to oscillations in the spin density around the scattering centre. A related effect, named Friedel oscillations, also exists for the charge density[14]. The inducing of a spin polarisation in the surrounding conduction electrons via a local moment was first put in consideration by Ruderman and Kittel[15]. The polarised spins can now induce, dependent on their spin orientation, a magnetic moment in surrounding Pd atoms. The spin polarisation of the conduction electrons oscillates in sign as a function of distance from the localised magnetic moments of the atoms[16,17]. This oscillation is damped and has (at large distances) the form[18]:

$$J(R) = \frac{2A^2 m_\mathrm{e} k_\mathrm{F}}{(2\pi)^3 \hbar^2} \, \frac{\cos(2k_\mathrm{F}R)}{R^3} \,. \tag{2.7}$$

Here, $J(R)$ is the RKKY exchange coefficient, A is the intra-atomic exchange parameter, m_e is the mass of an electron, k_F is Fermi wave vector which is related to the Fermi energy via $E_\mathrm{F} = \frac{\hbar^2 k_\mathrm{F}^2}{2m_\mathrm{e}}$, $\hbar$ is the reduced Planck's constant and R is the distance from the localised magnetic moment. A graphical representation of the RKKY function is shown in figure 2.6.

In a PdCo alloy, the magnetic Co atoms induce a spin polarisation in the conduction electrons which polarise other surrounding Co atoms via the RKKY interaction. Additionally, Co atoms polarise also the surrounding Pd atoms, which is described by the exchange-enhanced

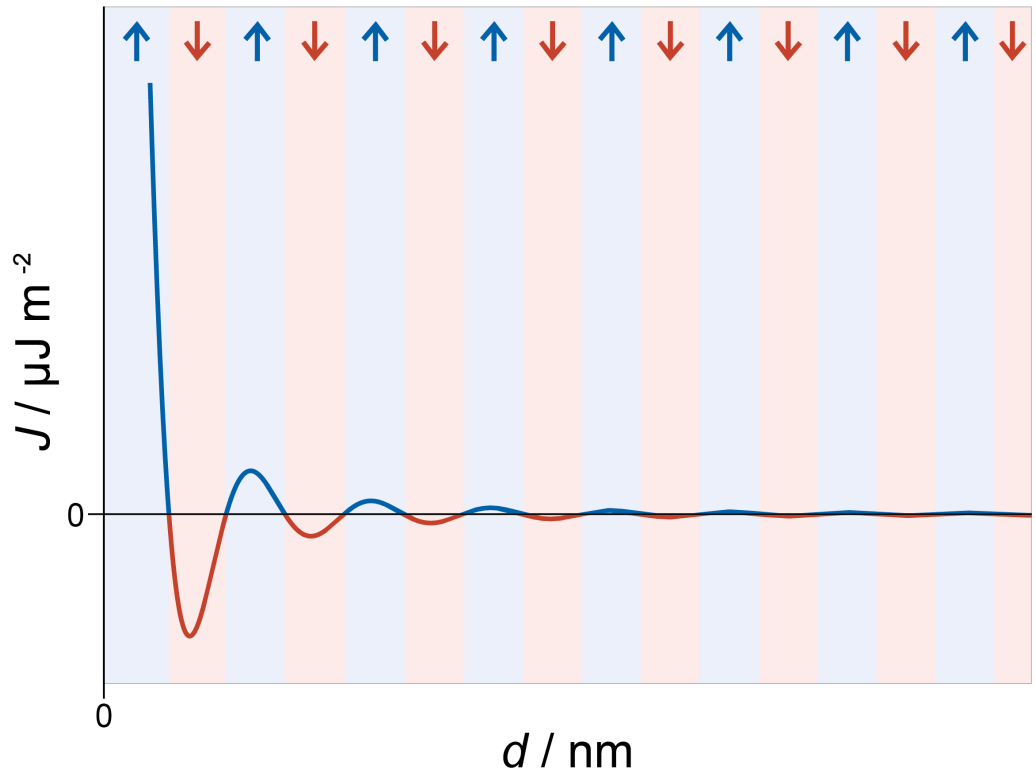

Figure 2.6: Exchange coupling strength J between two atoms magnetic atoms in dependence of their distance d. The arrows and the corresponding colours present the type of coupling. (Blue for ferromagnetic and red for antiferromagnetic coupling.)

RKKY interaction[19]. This results in a parallel or antiparallel alignment of magnetic moments, dependent of their distance to a Co atom. So, depending on the space between them, the magnetic coupling between a Co atom and a Pd atom, or between two Co atoms, can be ferromagnetic or antiferromagnetic. Constant[20] and Gerstenberg[21] reported, that dilute solutions of Co in Pd are ferromagnetic (working above 80 K with 5 at% Co in Pd). Furthermore, the magnetic moment per Co atom is larger than the atomic moment of pure Co. Additionally Bozorth et al. found out that even a dilute solution of 0.1 at% Co in Pd is ferromagnetic and 8 to 10 at% Co and above is ferromagnetic at room temperature[22].

2.6 Magnetic Tuning

The concept of magnetic tuning by electric fields is an efficient way to process magnetic information without heat dissipation due to the need of flowing currents. Materials which serve as the basis for controlling the magnetisation by an applied electric field usually are

multiferroics[23,24], magnetic semiconductors[25,26] or, as used in this work, (magnetic) metals. However the work with multiferroics turns out to be difficult, since they are usually rare and hard to synthesise, furthermore no known ferromagnetic multiferroic shows only a single phase at room temperature[27] and usually high voltages are necessary to obtain reasonable high electric fields, needed for the magnetic bias[5,28]. Also semiconductors have their disadvantages. The typical low Curie temperature T_C of magnetic semiconductors limits the application of magnetic tuning to low temperatures. Metals allow to overcome of these disadvantages. However, metals show a small Thomas–Fermi screening length δ, which means that only a small part of the atoms of the material is affected by the applied electric field. The small penetration depth of electric fields can be compensated by the use of large surface-to-volume ratios for the electrodes and the application of high voltages. Large electric fields are attainable via the use of solid dielectrics[29–31] or via electrolyte gating, which is the approach in this work. With the help of an electrolyte, the appearance of a high electric field within the electrochemical double layer between the metal and the electrolyte can be exploited. Furthermore chemical reactions in the electrolyte (redox reactions and ad- or desorption of ions) can be used to alter the elctronic structure further. To affect the magnetisation as much as possible, one would maximise the charge transfer. In terms of a capacitor the charge Q can be written as:

$$\Delta Q = C \cdot \Delta U \tag{2.8}$$

It is seen, that in order to get a high charge density, the capacity C and the voltage U should be as high as possible. To attain a large voltage, electrolytes in organic solvents can be used, in order to avoid the limitation by water decomposition. A large capacity is obtained by a high surface area. High surface-area electrodes in the present work are obtained by fabricating a nanoporous structure by dealloying.

2.7 Superconducting Quantum Interference Device

For all magnetic measurements in this work, a superconducting quantum interference device (SQUID) was used, namely, a MPMS®-XL-7 magnetometer (Quantum Design Inc., San Diego, CA, USA). The SQUID is a highly sensitive magnetometer which enables reliable

measurements of changes in the magnetic moment down to $4 \cdot 10^{-7}$ emu[32]. In this section, the MPMS® SQUID magnetometer system of Quantum Design Inc. is described[33], which is the most common commercially-used used SQUID system[34].

A measurement is performed by moving the sample through a set of superconducting detection coils, which lie outside the sample chamber at the centre of a magnet. These detection coils consist of a single piece of superconducting wire wound to three coils, configured as a second-order gradiometer[33]. The configuration of the coils can be seen in figure 2.7.

The top coil and the bottom coil are wound clockwise and have one meander, while the middle coil is wound counter-clockwise and has two meanders. The gradiometer configuration is used to minimise noise in the circuit, produced by the fluctuations in the high magnetic field of the magnet. The coils are connected to the SQUID.

Before the measurements starts, a magnetic field of 500 mT is applied to find the position of the sample, so it can be adjusted to the middle of the coils. This procedure is called centring. As the sample is moved through the coils during the measurement, the magnetic moment of the sample induces an electric current into the coils. Since, the wire of the coils forms a closed loop with the SQUID input coil, any change in the magnetic flux in the detection coils will create a change in the continuous current in the detection circuit. This change in current is proportional the change in magnetic flux. Since, the current in the detection coils is coupled to the SQUID sensor, because of the connected superconducting wire, a change in current will result in a change in the output voltage of the SQUID. So, if properly adjusted, the SQUID produces an output voltage, which is strictly proportional to the magnetic flux in the detection coils. Calibration is done via a piece of material, whose mass and susceptibility is known. Magnetic moments are obtained by fitting the response of a magnetic dipole to the measured signal.

Since, the magnet is formed as a superconducting closed loop, once charged, the magnet can operate without any power supply or external current source. For generating a specific current or changing an applied current, the superconducting loop has to be electrically opened to allow charge to flow in or out. This is accomplished by placing a heater around a small fraction of the superconducting wire. The heater heats the fraction of the superconducting wire, so that this segment loses its superconducting property, which electrically opens the

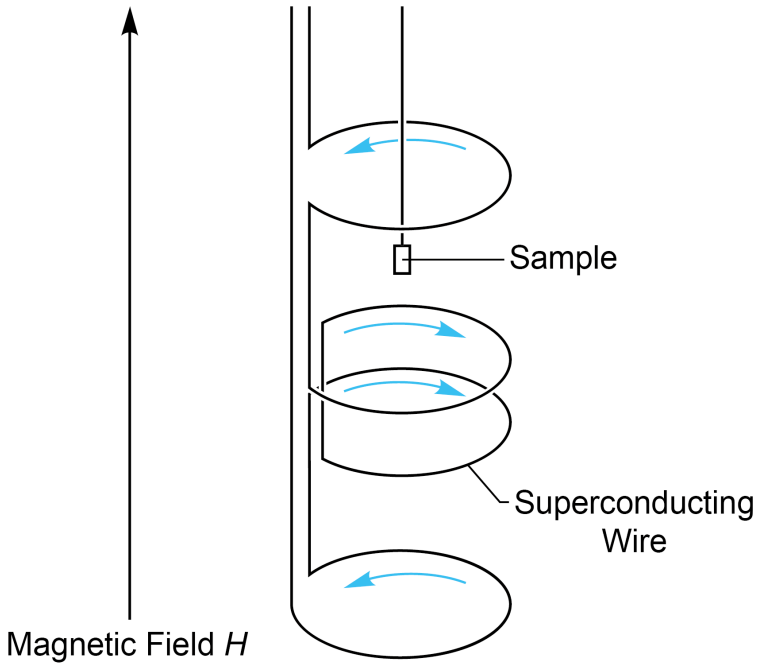

Figure 2.7: Graphical representation of the detection coils of the SQUID.[33]

superconducting loop. The use of a power supply, connected to each side of the heater, allows to change the current in the superconducting loop. Since, liquid helium is used for cooling, which slowly vaporises, helium needs to be refilled from time to time.

Chapter 3

Experimental

3.1 Dealloying and Annealing

The CoPd alloy was prepared by electrochemical arc melting at the Institute of Materials Physics of TU Graz. All samples were cut from exactly the same master alloy to avoid microstructural differences between the samples. For dealloying CoPd into np-Pd(Co) an electrochemical etching process, proposed by Hakamada and Mabuchi [8], was used. In their work, $0.1\,\mathrm{mol\,L^{-1}}$ H_2SO_4 was used as an electrolyte, a saturated calomel electrode as reference electrode and $+0.500\,\mathrm{V}$ as constant working electrode potential. This configuration corresponds to $+0.550\,\mathrm{V}$ with Ag/AgCl as a reference electrode. In this work, Ag/AgCl (3M KCl/3M KNO_3) was used as reference electrode. The standard electrode potential of this reference electrode is $+0.197\,\mathrm{V}$ versus the standard hydrogen electrode at room temperature. A wound platinum wire served as counter electrode. To connect the CoPd-working electrode with the potentiostat, a Au wire was used. A picture of a sample, attached to a Au wire can be seen in figure 3.1.

The dealloying process was performed until a residual current, lower than $10\,\mu\mathrm{A}$ was measured. During the dealloying, the electrolyte turned dilute pink, indicating the dissolution of Co as Co^{2+}. All electrochemical measurements in this work were performed by an Autolab potentiostat (PGSTAT128N or PGSTAT204), controlled by the NOVA software by Metrohm Autolab BV.

After dealloying the sample was soaked in distilled water to remove remnants of the elec-

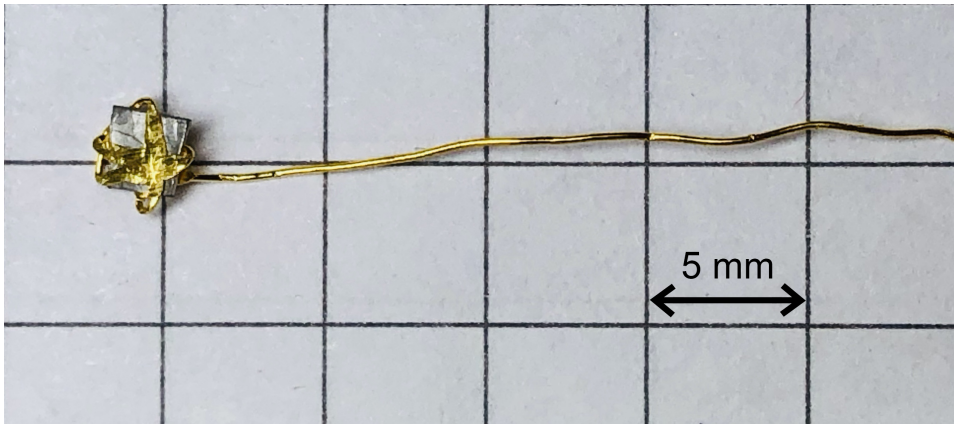

Figure 3.1: CoPd sample attached to an Au wire.

trolyte from the sample. The sample was immersed at least for 1.5 h. Then the sample was taken out and the remaining water was carefully dabbed with use of laboratory paper. The influence of coarsening was studied by thermal treatment. For each measurement series, five sample were prepared. One sample was not subjected to a thermal treatment, while the other four were annealed to a certain annealing temperature in a vacuum furnace with a heating rate of $20\,\mathrm{K\,min^{-1}}$. The following annealing temperatures were chosen: 373 K, 573 K, 773 K, and 973 K. At the respective temperature, the samples were hold for 10 min until subsequently the furnace was turned off and the samples slowly cooled down in the furnace. The annealing temperatures are much lower than the melting temperatures of Pd (ca. 1828.0 K) or Co (ca. 1768.0 K)[35], avoiding structural changes due to melting.

3.2 Determination of Cobalt Concentration

To determine the residual cobalt content in the samples, a concentration measurement was performed by a X-ray fluorescence (XRF) at the Institute of Solid State Physics of TU Graz. For XRF, the spectrometer Epsilon 1 (Malvern Panalytical Comp.) with the corresponding software was used. From each thermal treatment, one sample was investigated. The residual cobalt content for all samples was determined to about 5.5 wt% which corresponds to about 8.7 at%.

3.3 Cell Construction

In this work, three measurement series were accomplished, one of which was performed *ex situ*, the other *in situ*. Within each series, five samples, annealed at different temperatures (none, 373 K, 573 K, 773 K, 973 K) were measured.

In order to get information about the magnetic properties and how they change, magnetisation measurements with changing magnetic field were performed for the five different *ex situ* samples of nanoporous palladium. The samples were put in plastic capsules and carefully fixed with cotton. The capsules were sewn, by use of a thread, at a certain distance into a plastic straw to investigate them in the SQUID. For every sample the magnetisation was measured as a function of the magnetic field within the applied field ranges from -3 to 3 T at two temperatures, 4.2 and 300 K. Additionally ZFC and FC measurements were performed.

The *in situ* measurements of the nanoporous palladium samples were performed by CV-cycling in dependence of an applied constant magnetic field. All *in situ* measurements were carried out at around 298 K (room temperature). The working electrode was put, together with the reference and counter electrode in a narrow but high cylindrical tube with an outer diameter of 5 mm. The electrode lie one above the other, as seen in figure 3.2. The distance from the working electrode to the reference electrode and to the bottom of the tube has to be at least 4 cm to prevent noises. To prevent a short circuit, the wires were mounted in a fine polyethylene tube. At the top of the tube, a plug with three small feed-throughs, for the wires, was used to close the tube. The plug was glued into the tube with a two components epoxy adhesive (UHU plus endfest 300, binder and hardener). As a precaution, a second two components epoxy adhesive (Loctite 1C Hysol, resin and hardener) was used on top of the closed tube. The protruding wires were connected to the SQUID for measurements. Two different setups were used to study the behaviour of the nanoporous samples in different electrolytes.

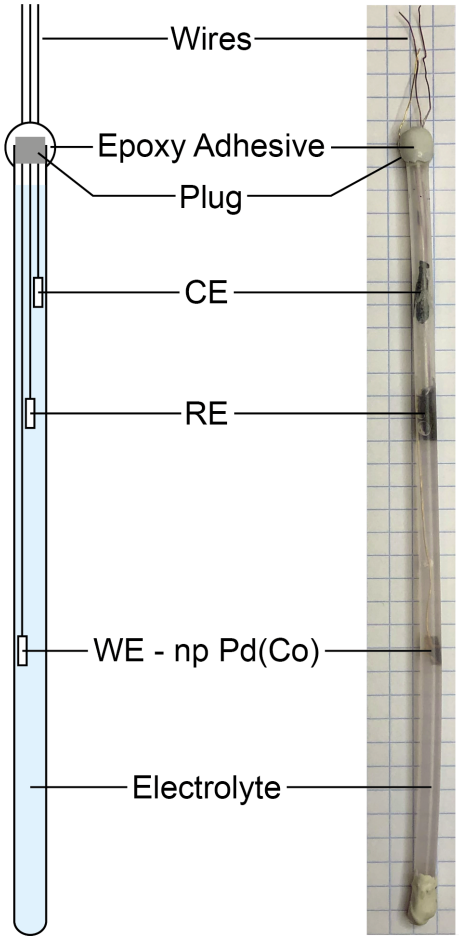

Figure 3.2: Schematics of the electrochemical cell design used for the *in situ* measurements in the SQUID.

For the first of the *in situ* measurement series, nanoporous palladium (on a gold wire) was used as working electrode, $LiPF_6$ in ethylene carbonate (EC) and ethyl methyl carbonate (EMC) as electrolyte (EC/EMC 1:1), and two lithium electrodes on a copper wire as counter and reference electrodes. This electrolyte provides a large voltage window for CVs which is suitable for charging applications and which is associated to a high charge density. Additionally $LiPF_6$ has stable ions (Li^+ and PF_6^-) without H_2O and it is the most common Li salt in batteries. Non-aqueous electrolytes are well suited because they lack of hydrogen evolution reactions. The cell had to be build in an argon chamber in order to avoid, that lithium is disposed to oxygen. Inside the SQUID, CV measurements for surface charging were performed, while the magnetisation under an applied field of 500 mT was measured. In order to avoid voltage jumps, a linear voltage sweep was applied at the start of the measurement when necessary. The CVs were carried out in the voltage range from 3.1 to 4.2 V, which is a suitable range for double layer charging experiments[36]. For the first sample, the unannealed one,

five cycles with an applied field of 500 mT and a scan rate of 0.1 mV s^{-1} were performed. For each of the following samples, two cycles with a scan rate of 0.1 mV s^{-1} and three cycles with a scan rate of 0.5 mV s^{-1}, both under an applied field of 500 mT were measured. Additionally for these samples, six cycles with 50 mT and a scan rate of 0.5 mV s^{-1} were accomplished. All the *ex situ* and *in situ* measurements, which were performed, are summarised in tables 3.1 and 3.2. With exception of the as-dealloyed sample, for this measurement series (np-Pd(Co) in $LiPF_6$/EC/EMC) only the measurements with a scan rate of 0.5 mV s^{-1} will be discussed in this work.

The second measurement series was carried out in KOH dissolved in H_2O (1 mol L^{-1}). Au wires served both as reference and counter electrode. The working electrode was again the np-Pd(Co) sample on a Au wire. As a container, a borosilicate glass tube, free of magnetic impurities, was used. Inside the SQUID several CVs were measured under an applied field of 500 mT. In the beginning, two cycles of a CV over a wide potential range (0.3 to −0.9 V) were performed to remove possible oxides from the surface. Then multiple CVs with different scan rates and/or potential limits were accomplished. An overview of all *ex situ* and *in situ* measurements can be seen in table 3.1 and table 3.3.

Table 3.1: List of accomplished *ex situ* measurements in chronological order. (Note: Green highlighted measurements are the one which will be discussed in this work.)
T_A.....Annealing temperature
Type...Type of measurement
$\mu_0 H$....Magnetic field
T_M.....Measurement temperature
Fig....Figure

Ex situ

T_A / K	Type	$\mu_0 H$ / mT	T_M / K	Fig.
RT	ZFC	5	4.2-300	4.3
	FC	5	300-4.2	4.3
	Hysteresis	-5000-5000	4.2	4.1
	Hysteresis	-5000-5000	300	4.2
373	ZFC	5	4.2-300	4.3
	FC	5	300-4.2	4.3
	Hysteresis	-5000-5000	4.2	4.1
	Hysteresis	-5000-5000	300	4.2
573	ZFC	5	4.2-300	4.3
	FC	5	300-4.2	4.3
	Hysteresis	-5000-5000	4.2	4.1
	Hysteresis	-5000-5000	300	4.2
773	ZFC	5	4.2-300	4.3
	FC	5	300-4.2	4.3
	Hysteresis	-5000-5000	4.2	4.1
	Hysteresis	-5000-5000	300	4.2
973	ZFC	5	4.2-300	4.3
	FC	5	300-4.2	4.3
	Hysteresis	-5000-5000	4.2	4.1
	Hysteresis	-5000-5000	300	4.2

Table 3.2: List of accomplished *in situ* measurements in $LiPF_6$/EC/EMC in chronological order. (Note: Green highlighted measurements are the one which will be discussed in this work.)
T_A.....Annealing temperature
Type.....Type of measurement
$\mu_0 H$.....Magnetic field
U_{bottom}...Lower potential limit
U_{top}.....Upper potential limit
sr.....Scan rate
n.....Number of cycles
Fig.....Figure

In situ: in $LiPF_6$/EC/EMC

T_A / K	Type	$\mu_0 H$ / mT	U_{bottom} / V	U_{top} / V	sr / mV s^{-1}	n	Fig.
RT	CV	500	3.1	4.2	0.5	5	4.7
373	CV	500	3.1	4.2	0.1	2	/
	CV	500	3.1	4.2	0.5	3	4.8
	CV	50	3.1	4.2	0.5	6	4.11
573	CV	500	3.1	4.2	0.1	2	/
	CV	500	3.1	4.2	0.5	3	4.9
	CV	50	3.1	4.2	0.5	6	4.12
773	CV	500	3.1	4.2	0.1	2	/
	CV	500	3.1	4.2	0.5	3	4.10
	CV	50	3.1	4.2	0.5	6	4.13
973	CV	500	3.1	4.2	0.1	2	/
	CV	500	3.1	4.2	0.5	3	/
	CV	50	3.1	4.2	0.5	6	/

Table 3.3: List of accomplished *in situ* measurements in KOH in chronological order. (Note: Green highlighted measurements are the one which will be discussed in this work.)
T_A.....Annealing temperature
Type.....Type of measurement
$\mu_0 H$.....Magnetic field
U_{bottom}...Lower potential limit
U_{top}.....Upper potential limit
sr.....Scan rate
n.....Number of cycles
Fig.....Figure

In situ: KOH

T_A / K	Type	$\mu_0 H$ / mT	U_{bottom} / V	U_{top} / V	sr / mV s^{-1}	n	Fig.
RT	CV	500	-0.9	0.3	0.1	2	/
	CV	500	-0.5	-0.4	0.1	10	4.14
	CV	500	-0.5	-0.4	0.5	20	/
	CV	500	-0.5	-0.4	1.0	20	/
	CV	500	-0.6	-0.4	0.5	10	/
	CV	500	-0.7	-0.4	0.5	10	4.18
373	CV	500	-0.9	0.3	0.1	2	/
	CV	500	-0.5	-0.4	0.1	10	4.15
	CV	500	-0.5	-0.4	0.5	20	/
	CV	500	-0.5	-0.4	1.0	20	/
	CV	500	-0.6	-0.4	0.5	10	/
	CV	500	-0.7	-0.4	0.5	10	4.19
573	CV	500	-0.9	0.3	0.1	2	/
	CV	500	-0.5	-0.4	0.1	10	4.16
	CV	500	-0.5	-0.4	0.5	20	/
	CV	500	-0.5	-0.4	1.0	20	/
	CV	500	-0.6	-0.4	0.5	10	/
	CV	500	-0.7	-0.4	0.5	10	4.20
773	CV	500	-0.9	0.3	0.1	2	/
	CV	500	-0.5	-0.4	0.1	10	4.17
	CV	500	-0.5	-0.4	0.5	20	/
	CV	500	-0.5	-0.4	1.0	20	/
	CV	500	-0.6	-0.4	0.5	10	/
	CV	500	-0.7	-0.4	0.5	10	4.21

Chapter 4

Results

4.1 Intrinsic Magnetic Properties of Nanoporous Palladium

4.1.1 Hysteresis Measurements

The magnetisation measurement at 4 K are shown in figure 4.1. All five samples exhibit hysteresis and saturation. The hysteresis loop for the as-dealloyed sample has a saturation magnetisation of about $10\,\mathrm{emu\,g^{-1}}$ at a field of 3 T. Magnetisation slowly decreases towards lower fields, then starts to fall drastically, followed by another slope, until it saturates at nearly $-10\,\mathrm{emu\,g^{-1}}$. For the path from -3 T to 3 T the same behaviour is observed. This for ferromagnetic materials, typical hysteresis loop leads to a coercivity of about 160 mT. The annealed samples also exhibit a non-zero coercivity. The values for the coercivity, saturation magnetisation and remanent magnetisation, determined from the hysteresis loops, are summarised in table 4.1. It can be seen, that the magnitude of the saturation magnetisation decreases with annealing temperature and becomes noticeable lower beyond an annealing temperature of 773 K ($\sim$4.5 $\mathrm{emu\,g^{-1}}$), until it almost vanishes at 937 K ($\sim$0.7 $\mathrm{emu\,g^{-1}}$). The area within the curves becomes visible smaller with higher annealing temperature, which is a result of the decreasing coercivity and remanent magnetisation. The coercivity remains at first roughly constant and decreases perceptibly beyond 773 K coarsening temperature. The remanent magnetisation shows the same decreasing behaviour for higher temperatures.

The slope at lower fields decreases with higher annealing temperature, which results in a flattening of the hysteresis loops. The slope at larger fields becomes also successively flatter until it is nearly constant at 973 K. Due to this flattening the magnetisation starts to saturate earlier, at lower fields. These effects become also stronger noticeable beyond 773 K annealing.

Table 4.1: Coercivity, saturation magnetisation, remanent magnetisation measured at 4.2 and 300 K for different annealed nanoporous palladium samples (cf. figure 4.1 and 4.2).
T_A.....Annealing temperature
$H_{C,\,4\,K}$.....Coercivity at 4.2 K
$M_{S,\,4\,K}$.....Saturation magnetisation at 4.2 K
$M_{r,\,4\,K}$.....Remanent magnetisation at 4.2 K
$H_{C,\,300\,K}$...Coercivity at 300 K

T_A / K	$\mu_0 H_{C,\,4\,K}$ / mT	$M_{S,\,4\,K}$ / emu g^{-1}	$M_{r,\,4\,K}$ / emu g^{-1}	$\mu_0 H_{C,\,300\,K}$ / mT
RT	158 ± 2	10.565 ± 0.001	6.89 ± 0.03	0 ± 2
373	158 ± 2	9.3520 ± 0.0006	5.60 ± 0.03	1 ± 2
573	163 ± 2	8.050 ± 0.001	4.41 ± 0.03	2 ± 2
773	107 ± 2	4.4025 ± 0.0004	2.31 ± 0.02	5 ± 2
973	54 ± 2	0.7296 ± 0.0003	0.223 ± 0.004	9 ± 2

The magnetisation measurements at 300 K are displayed in figure 4.2. It is seen that we have no clear "open" hysteresis loop and the magnetisation passes almost through its origin. Therefore we observe a remanent magnetisation and a coercivity of nearly zero. Although the coercivity is near zero for the as-dealloyed and 373 K-annealed sample, it can be seen that with rising annealing temperature the coercivity becomes larger and a value of 5 mT is reached at 773 K annealing temperature, which makes the sample weakly ferromagnetic. The values for the coercivity are displayed in table 4.1. A saturation, identified as a relative change in magnetisation lower than 5 % for a minimal range of 2 T, is only attained, beyond 773 K, which speaks also for the ferromagnetic nature of these samples. It is also visible that the centre of the different hysteresis curves is slightly shifted from the origin. Because the curves are not shifted in the same direction, this may be a measurement inaccuracy due to trapped fluxes which origin from the experimental history of the measurement device [32]. Like in the measurements at 4.2 K, we can see here also a flattening of the slope, up to an annealing temperature of 573 K, in the centre and at the edges which leads to a nearly constant magnetisation at 973 K, with a saturation magnetisation near zero. The saturation magnetisation again exhibits the trend to decrease with increasing annealing temperature. As well

here, the effects become more noticeable beyond an annealing temperature of 773 K.

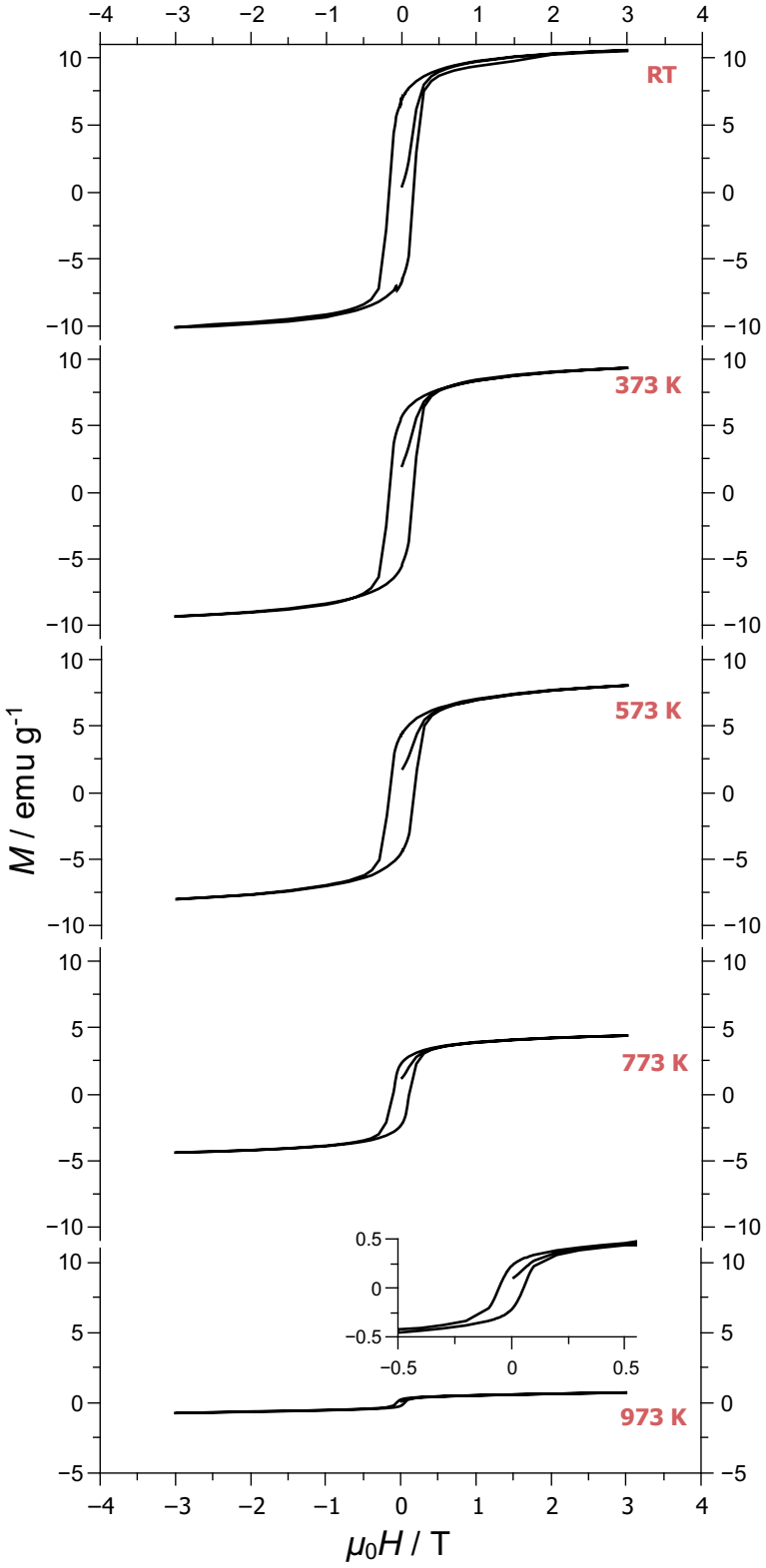

Figure 4.1: Magnetisation in dependence of magnetic field at 4.2 K for nanoporous palladium, thermal coarsened with different annealing temperatures. Inset: enlarged view of sample 973 K.

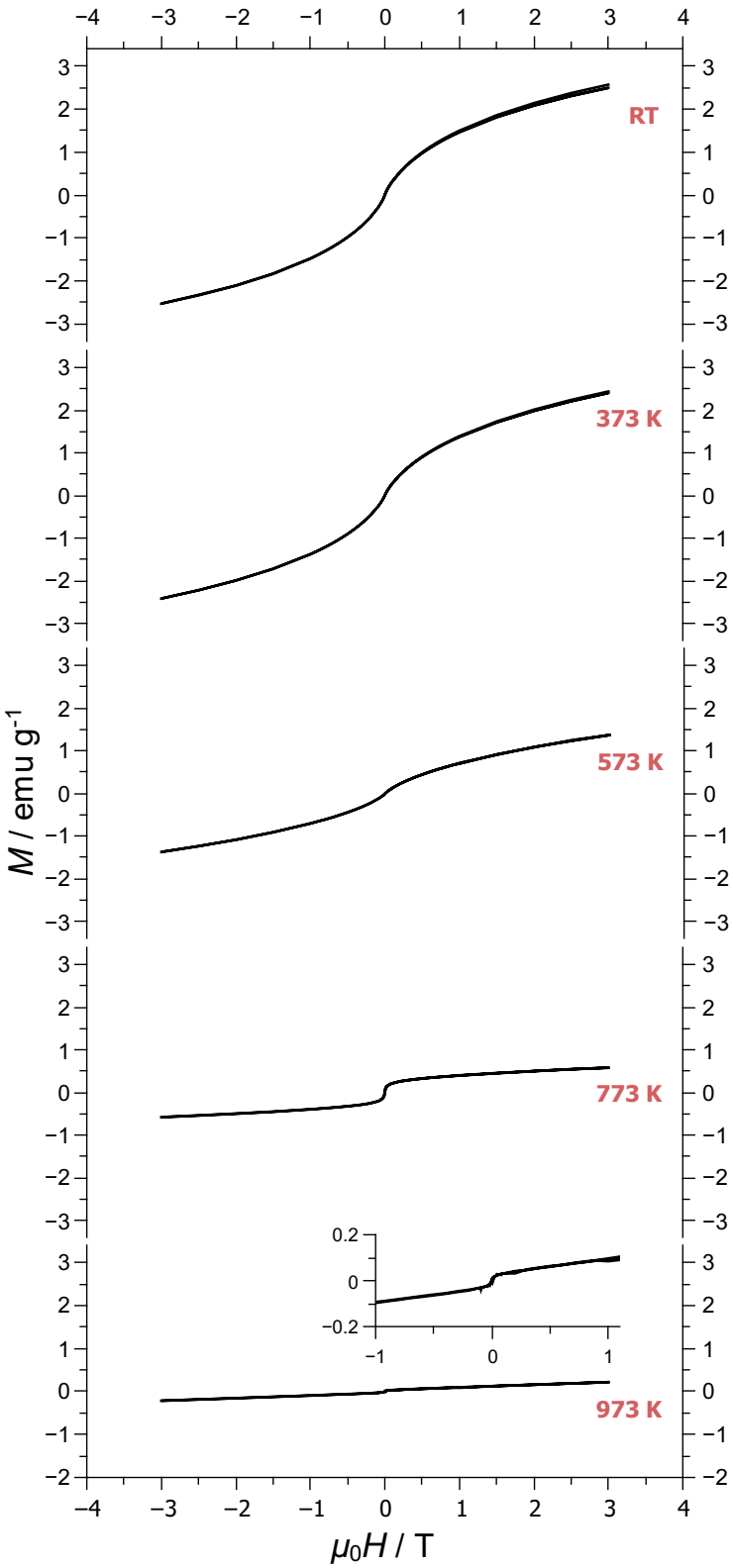

Figure 4.2: Magnetisation in dependence of magnetic field at 300 K for nanoporous palladium, thermal coarsened with different annealing temperatures. Inset: enlarged view of sample 973 K.

4.1.2 Zero Field Cooling and Field Cooling

Zero field cooled (ZFC) and field cooled (FC) modes of temperature dependent magnetisation curves were measured at an applied magnetic field of 5 mT in the temperature range from 4.2 to 300 K. The curves for samples with different temperatures of thermal coarsening, including a sample which is not coarsened, are displayed in figure 4.3.

The ZFC curve (red) of the non-coarsened sample starts with a magnetisation of around 0.7 emu g^{-1} at 4.2 K and shows a slow increase in magnetisation with increasing temperature until a maximum is reached at ∼100 K. This maximum is identified as the blocking temperature T_B. With rising temperature the magnetisation starts to decrease and eventually converges to zero at 300 K. The FC curve (blue) starts at 300 K and follows at first the path of the ZFC curve, as temperature decreases, until it slowly begins to separate and rises, with a stronger increase, beyond the ZFC curve, until the increase in magnetisation reduces and ends at ∼2.5 emu g^{-1} at 4.2 K. The curves of the samples, annealed to 373 K and 573 K, are quite similar. We can see that the curves bifurcate at higher temperatures for higher annealing temperatures. Also the blocking temperature starts to shift to lower temperatures and the peak reduces in magnetisation. The blocking temperature can be determined to ∼75 K for an annealing to 373 K and to 60 K for 573 K. It is also noticeable that with a higher blocking temperature, a wider ZFC peak is developed. The magnetisations at 4.2 K for the ZFC curves decreases, while the magnetisation at 4.2 K for the FC curve increases with annealing temperature. Therefore, both values are getting closer to zero and the gap between them becomes narrower. Beyond 773 K annealing temperature, these effects become stronger and the curves start to look different. For the sample annealed to 773 K the separation starts almost at 300 K, the magnetisation of the FC curve at 4.2 K has reduced to ∼1.2 emu g^{-1} and the blocking temperature is at ∼35 K. It is also noticeable that both branches of the curve have become flatter. This effect clearly dominates the curves of the sample heated to 973 K. The curves have become so flat that a curvature is barely recognisable anymore and so the blocking temperature is not clearly definable. The gap between the magnetisations at 4.2 K is about 0.1 emu g^{-1} and the division between the two curves resembles two straight lines with an angle to each other. For all measurement a magnetisation below zero is observed for low temperatures.

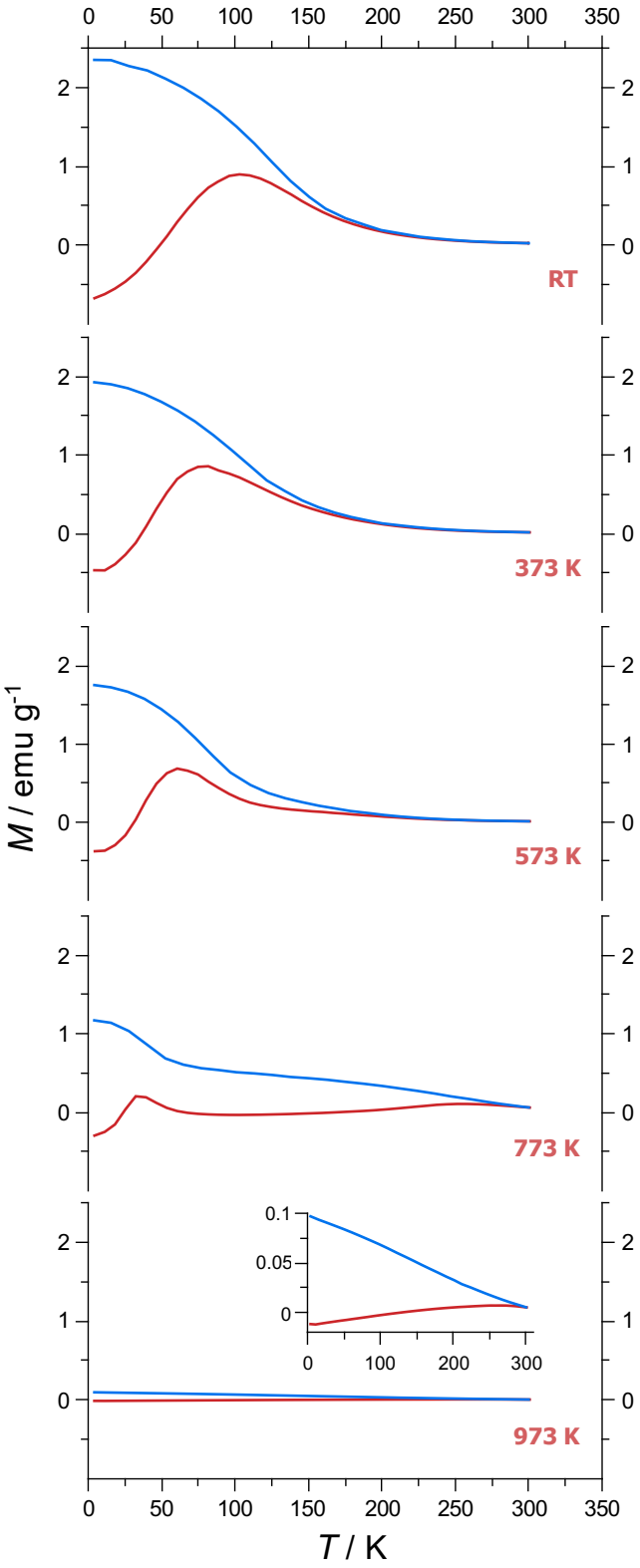

Figure 4.3: Zero field cooled (red) and field cooled (blue) magnetisation curves versus temperature at 5 mT for nanoporous palladium, thermal coarsened with different annealing temperatures. Inset: enlarged view of sample 973 K.

4.1.3 Surface Area Determination

To determine the specific surface area per mass of the nanoporous palladium samples, two different procedures were selected which were adopted from Fang[37]. In the first procedure the double layer capacitance was measured by multiple cyclic voltammetry experiments (CVs) with varying scan rates. The capacitance measured in this way allows to calculate the surface area. In the second procedure the upper limit of the CV potential was varied and the charge from the developed palladium oxide monolayer was determined. By means of this charge the surface area can also be evaluated. Both measurements were performed in $0.5\,\mathrm{mol\,L^{-1}}$ H_2SO_4, a carbon cloth on a platinum wire was used as counter electrode and Ag/AgCl (3M KCl/3M KNO_3) was used as reference electrode. The nanoporous palladium sample, the working electrode, was connected with a gold wire to the circuit.

For the first method based on the double layer, the scan rates for the CVs were chosen to be 5, 6, 7, 8, 9 and $10\,\mathrm{mV\,s^{-1}}$. The double layer capacitance can be defined by plotting the double layer current I_{DL} of a plateau over the scan rate sr which was used. The double layer current was determined by picking the value of the current in the middle of the voltage range. For the unannealed sample and the samples annealed to 373 K and 573 K, this corresponds to the current at 0.25 V and for the sample annealed to 773 K to the current at 0.3 V. The slope from a plotted regression line then determines the capacitance C_{DL} via:

$$C_{\mathrm{DL}} = \frac{\mathrm{d}Q}{\mathrm{d}U} = \frac{I_{\mathrm{DL}}\mathrm{d}t}{\mathrm{d}U} = \frac{I_{\mathrm{DL}}}{sr}\,. \tag{4.1}$$

With the known capacitance, the mass of the sample after dealloying m, and a reference capacitance of $(23.1 \pm 0.4)\,\mathrm{\mu F\,cm^{-2}}$ for a smooth palladium electrode[37], the surface area A_{DL} and the specific surface area SSA can be calculated:

$$A_{\mathrm{DL}} = \frac{C_{\mathrm{DL}}}{23.1\,\mathrm{\mu F\,cm^{-2}}}\,, \tag{4.2}$$

$$SSA = \frac{A_{\mathrm{DL}}}{m}\,. \tag{4.3}$$

It is noted that the value for the reference capacitance is only an estimation, since the refer-

ence value is for a smooth palladium sheet electrode, while we use a nanoporous palladium electrodes in the pesent work. In addition to the values for the specific surface area, the bulk density of palladium ρ, which is $12\,\mathrm{g\,cm^{-3}}$ [35] and a dimensionless constant C for disordered nanoporous structures, which can be determined to 3.7[38], is used to calculate the ligament size of the nanoporous samples[38]:

$$w = \frac{C}{\rho SSA}\,. \tag{4.4}$$

Note: The constant C should not be intermixed with the capacitance. All evaluated values are summarised in table 4.2 and the CVs in the double layer region and the associated I_{DL}-sr curves are shown in figure 4.4.

In the CV curves, the habitual deviation from the ideal behaviour as a electrochemical double layer can be seen due the ohmic resistance of the double layer. The expected linear relationship between the average of the current plateau and the scan rate in the I_{DL}-sr curves is clearly visible. For the measurement of the sample annealed at 773 K the voltage range was shifted by 0.05 V to 0.25-0.3 V in order to obtain typical double layer behaviour. The method was also carried out for a 973 K-annealed sample, but the currents were too small to identify clear plateaus, which suggests a very low surface area, or bad electrical contact between the gold wire and the sample after heat treatment.

The second procedure makes use of the fact, that a Pd^{2+} oxide monolayer forms on a clean palladium surface. The charge of this oxide monolayer can be used to calculate a reference charge per unit area. A reference charge of $424\,\mu\mathrm{C\,cm^{-2}}$ [39] corresponds to the adsorption on a Pd(100) plane and to a charge transfer of two electrons per adsorbed atom. To determine the charge, multiple CVs with a scan rate of $0.2\,\mathrm{mV\,s^{-1}}$ were performed in which the upper potential limit in the oxide region was increased by each CV. Since a parallel running process of oxygen development dominates at higher voltages, the direct adsorption current can not be used for the charge determination and instead the current from oxygen desorption is used. This current was integrated, which leads to the charge corresponding to the oxygen desorption. By plotting the evaluated charge over the upper potential limit a nearly linear relationship can be expected, including a point on a certain voltage, on which the slope becomes steeper. This circumstance is due to the fact that if one monolayer of Pd^{2+} oxide is

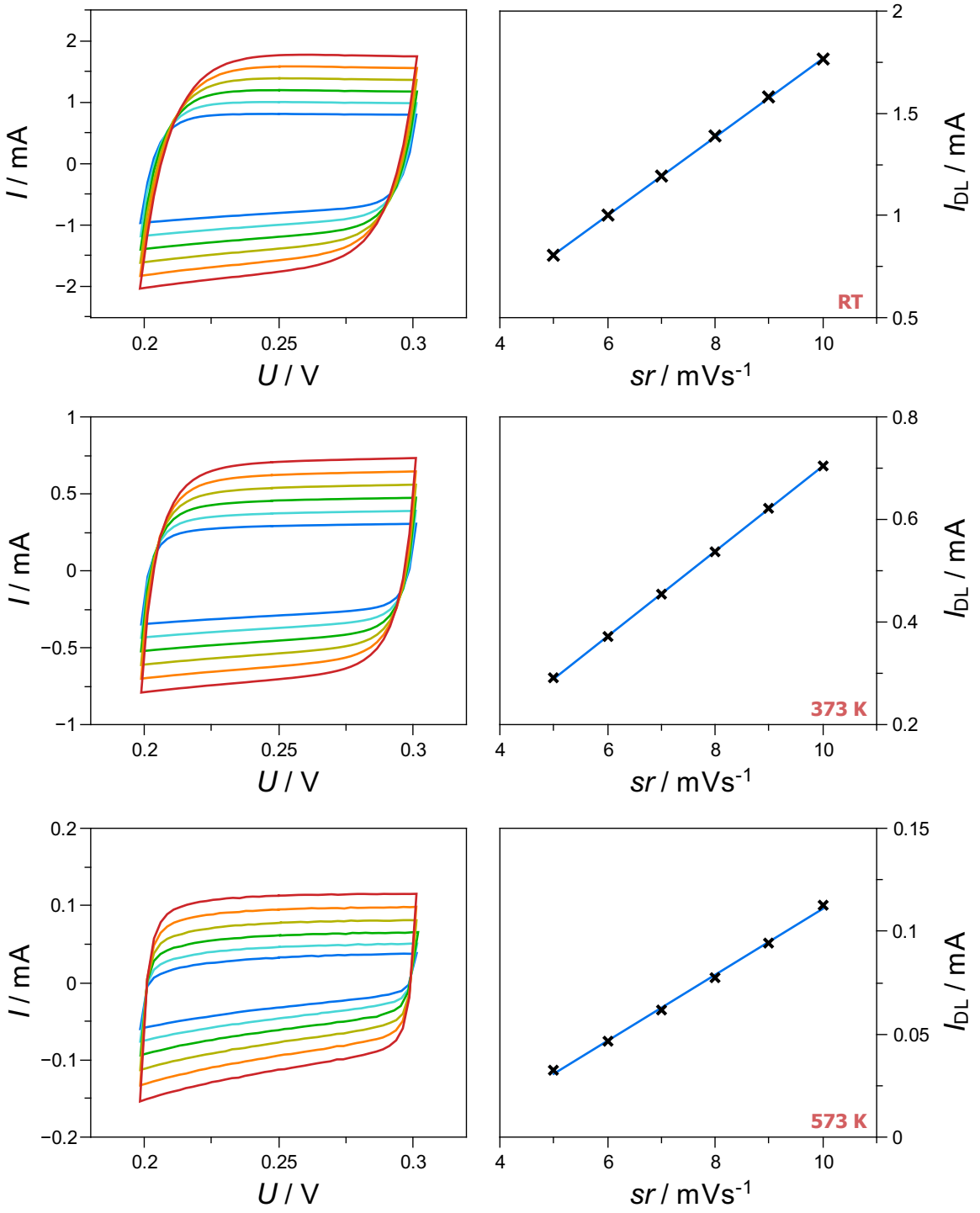

Figure 4.4: Cyclic voltammetry in the double layer range via scan rates from 5 (blue) to 10 mV s^{-1} (red) and corresponding I_{DL}-sr curves for nanoporous palladium without (RT) and after annealing at 373 K, 573 K and 773 K.

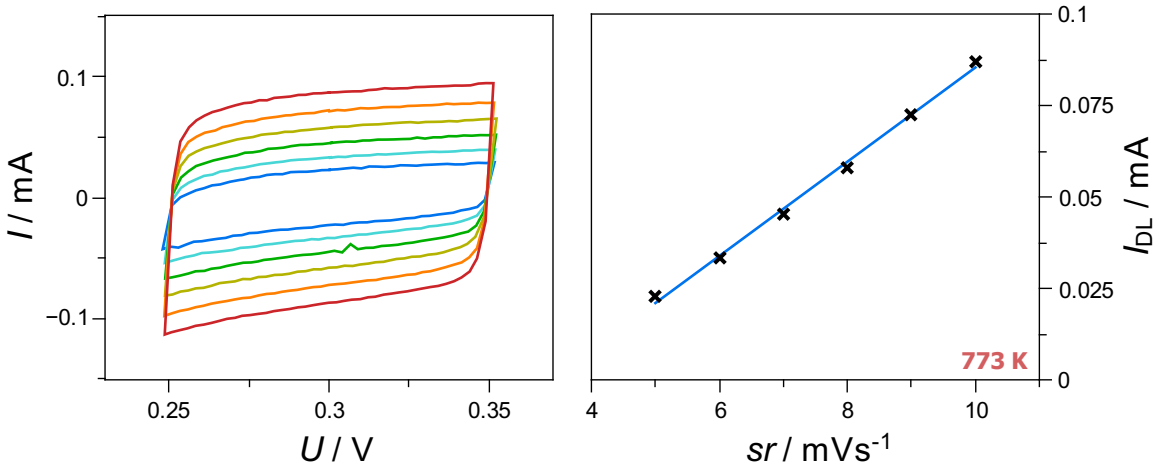

Figure 4.4 (Continued)

grown, a second layer of higher valency oxides, in particular Pd^{4+} begins to form[37,39–41]. The formation and reduction of this oxide layer are visible as peaks in the CVs. Figure 4.5 displays the CV measurements with varying maximal potentials and the evaluated charges versus these upper potential limits. Peak A marks the reduction of Pd^{2+} and peak B the reduction of Pd^{4+}. It is visible that peak B is only developed if the maximum potential is beyond 1.3 V, which underlines the formation of higher valency oxides above this voltage.

As can be seen in the Q-U diagrams (figure 4.5, right), the expected increase of the slope is barely visible and the last point at 1.35 V seems to decrease again. The charge, in the Q-U diagrams, at the point where the slope becomes steeper, here referred simply as Q, would be used to calculate the surface area via:

$$A_{\mathrm{DL}} = \frac{Q}{424\,\mu\mathrm{C\,cm^{-2}}}\,. \tag{4.5}$$

This value, together with the mass of the sample after dealloying, allows a calculation of specific surface area and ligament size, according to equation (4.3) and (4.4). Because of the non visible increase of the slope, it was not possible to define the certain point in which the reduction of Pd^{4+} begins and a surface area could not be evaluated. This unexpected behaviour could be due to the fact that this method is designated for a pure palladium area. Since the sample contains palladium and a certain residual amount of cobalt, depending on the dealloying potential and dealloying time, the cobalt atoms could contribute to the oxidation charge and the method might not work for the samples. Since the experiment did

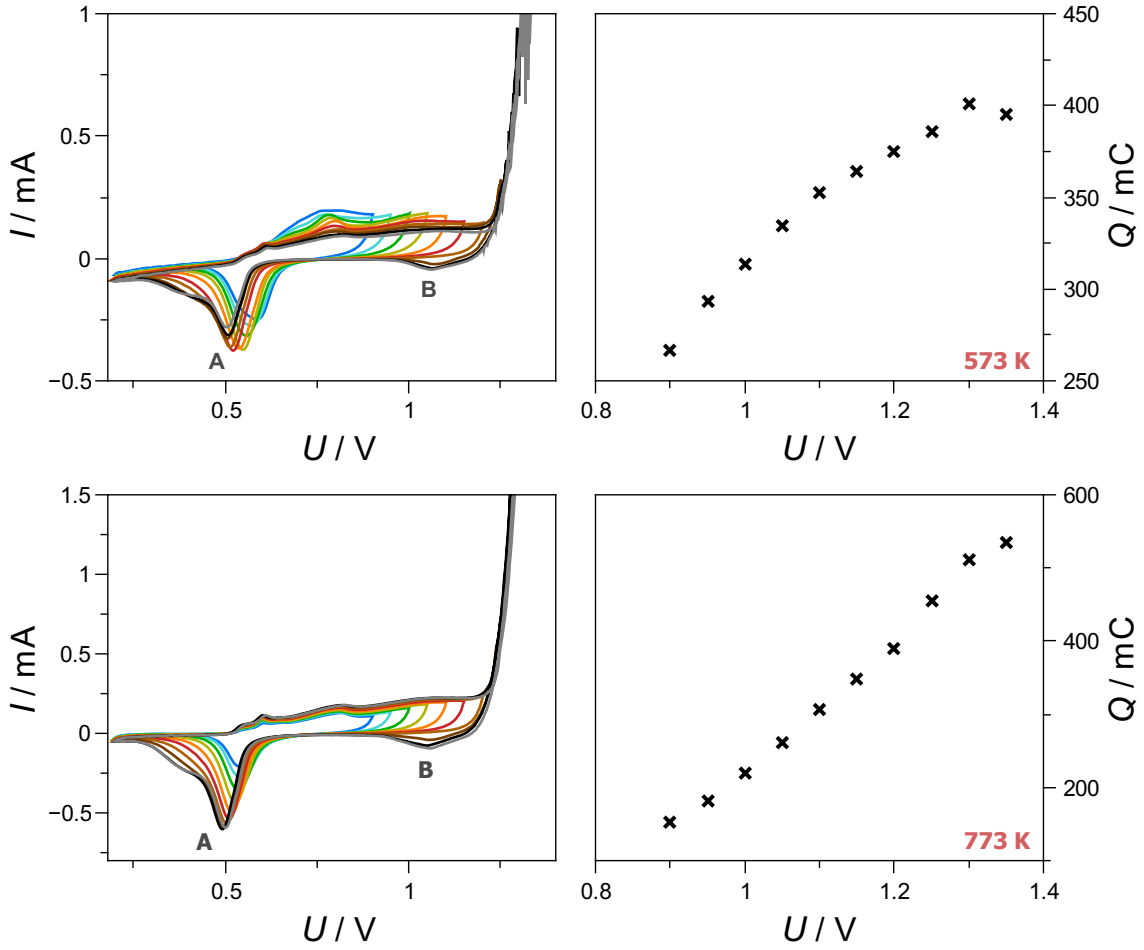

Figure 4.5: Cyclic voltammetry with a scan rate of $0.5\,\mathrm{mV\,s^{-1}}$ and with varying upper potential limit and corresponding Q-U curves for different annealing temperatures of nanoporous palladium.

not work out, measurements for other annealing temperatures were not performed.

The calculated values of specific surface area and ligament size in dependence of the annealing temperature are shown in figure 4.6. It is seen that with rising annealing temperature the ligament size of the nanoporous palladium increases, as already reported by McCue et al.[42]. This process leads to a reduction of the surface area and consequently of the specific surface area. While for the unannealed sample (data points corresponding to 298 K), a ligament size of 4 nm and a specific surface area of almost $70\,\mathrm{m^2\,g^{-1}}$ is observed, the ligament size of a sample annealed to 773 K is almost 6 × higher and it has about a 6 × smaller specific surface area. It is also seen that the trend of ligament size and specific surface area is almost linear with the temperature.

A comparison to the surface area determination of np-Pd(Co) from a previous work of

Table 4.2: Specific surface area and ligament size of nanoporous palladium samples, annealed with different temperatures.
T_A.....Annealing temperature
C_{DL}...Double layer capacitance
A_{DL}...Surface area determined via double layer capacitance (eq. 4.2)
SSA...Specific surface area (eq. 4.3)
w.....Calculated ligament size (eq. 4.4)

T_A / K	C_{DL} / F	A_{DL} / cm^2	SSA / $m^2\,g^{-1}$	w / nm
RT	0.1919 ± 0.0008	8310 ± 180	69.8 ± 1.6	4 ± 1
373	0.0830 ± 0.0003	3590 ± 80	54.4 ± 1.3	6 ± 1
573	0.0160 ± 0.0004	690 ± 30	15.7 ± 0.7	20 ± 3
773	0.0129 ± 0.0004	560 ± 30	11.9 ± 0.7	26 ± 5
973	/	/	/	/

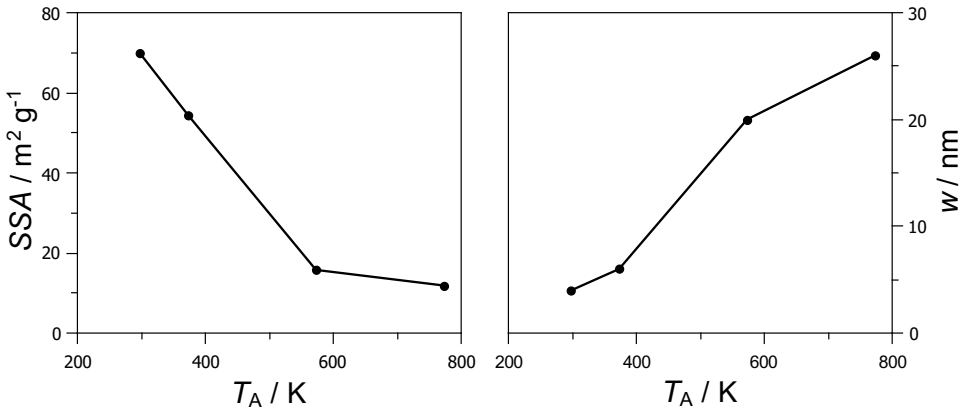

Figure 4.6: Specific surface area SSA and ligament size w according to table 4.2, plotted over annealing temperature.

Gößler[43] shows a similar magnitude of the specific surface area. In his work the master alloy consisted, just like here, out of CoPd (75:25 at%) and a dealloying potential of 0.550 V, the same as in this work, was used. Gößler reported a specific surface area of $13.4\,m^2\,g^{-1}$ for an unannealed sample, while here a specific surface area of about $70\,m^2\,g^{-1}$ was calculated. The difference of about $57\,m^2\,g^{-1}$ can be explained with the residual current. In the work of Gößler[43], the dealloying process was stopped at a residual dealloying current of 100 µA, while here the process went on, down to a residual current of only 10 µA. It can be assumed that the longer dealloying process applied here, is responsible for the higher surface area. A more similar result (50-70 $m^2\,g^{-1}$) to the received value of $70\,m^2\,g^{-1}$ was reported by Kong et al.[44], according to BET measurements for np-Pd prepared by dealloying PdAl.

4.2 Magnetic Tuning Measurements

Magnetic measurements in dependence of charging in the double layer regime were performed with non-aqueous Li-based electrolyte (section 4.2.1) and with aqueous KOH-electrolyte (section 4.2.2).

4.2.1 Lithium-Based Electrolyte

For the as-dealloyed sample, five cycles with an applied field of 500 mT were performed. For the thermal treated samples, three cycles with an applied field of 500 mT and six cycles with 50 mT were accomplished. For the sample annealed to 973 K, currents (in range of nA) were too small in order to give a reliable measurement. These small currents could be a consequence of a very low surface area or a bad electrical contact between the gold wire and the sample after the annealing. In the following the samples, which were annealed to 973 K were not considered. The measured alteration of the voltage, charge and magnetisation over the cycle for the different samples are shown in figures 4.7 to 4.13.

Figure 4.7 shows the triangular shape of the voltage versus time curve which was chosen for the present measurements. The charge is seen to increase by building up the voltage. After the upper potential limit is reached and the voltage decreases, the charge follows, after a small delay of ∼10 min. When the voltage approaches its lower limit, the charge shows a minimum, with the same 10 min delay. The voltage increases again and so does the charge. The next cycles follow this behaviour. An increase in charge is associated with an electron depletion at the surface in the double layer regime (positively charged electrode attracts negatively charged ions). It is visible that the maxima and minima shift over time, e.g. the first minimum is about 0.03 A s higher than the starting value and the second minimum about 0.02 A s higher than the first one. This relative shift decreases over time.

A shift like this can also be seen in the magnetisation, which is plotted as percentage change in relation to the value of the first magnetisation minimum. Charge maxima are associated with relative magnetisation minima, and vice versa. Relative maxima of the magnetisation coincide with the minima in the charge curve. The shift occurs consequently in the opposite direction. The curves for other annealing temperatures and for measurements with 50 mT show similar trends. The measurements at 500 mT are displayed in figures 4.7 to 4.10 and

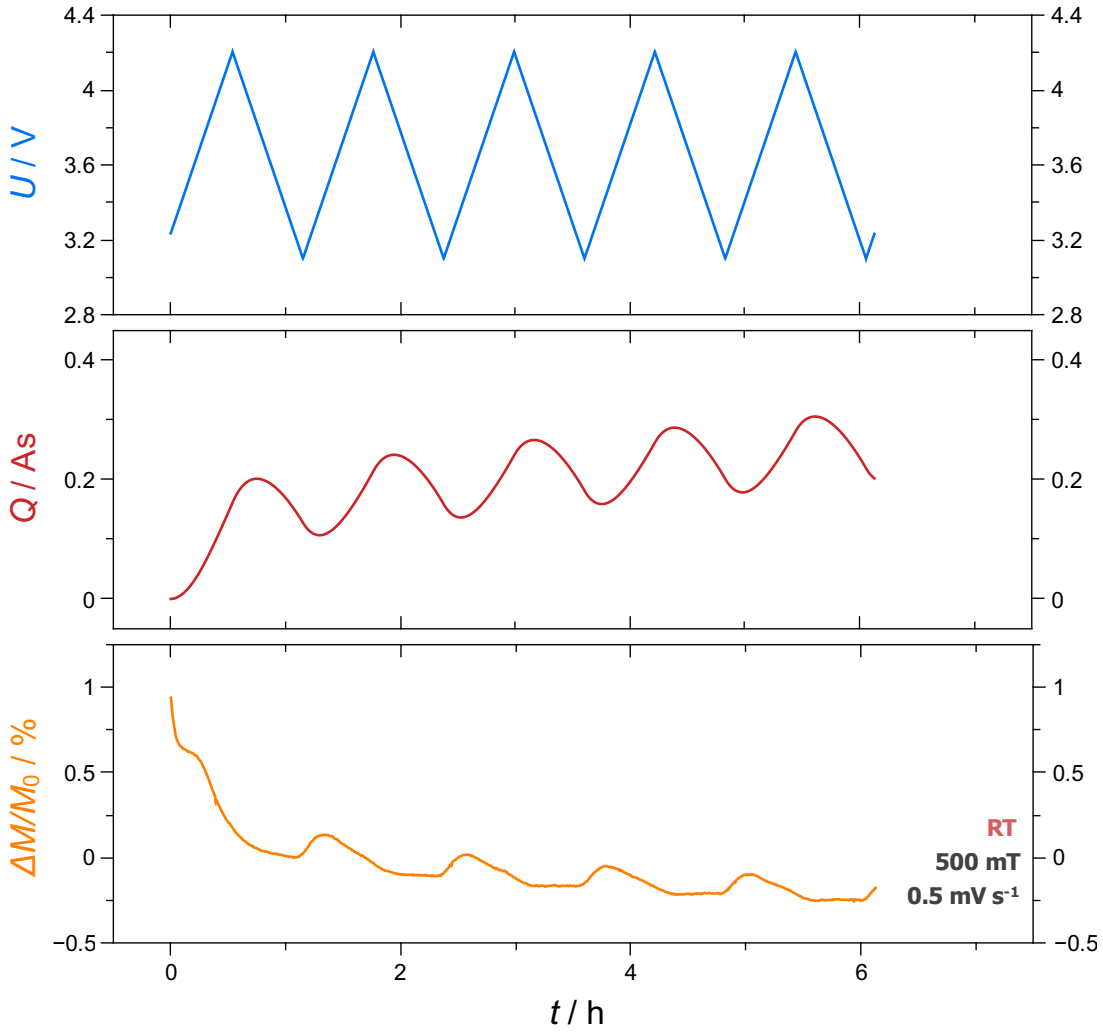

Figure 4.7: Voltage U, charge Q, and corresponding relative change in magnetisation $\frac{\Delta M}{M_0}$ as a function of time t upon *in situ* cycling, for as-dealloyed nanoporous palladium in the pseudocapacitive regime of $LiPF_6$/EC/EMC. Magnetic field: 500 mT, scan rate: 0.5 mV s^{-1}.

the measurements at 50 mT in figures 4.11 to 4.13. It is seen that the direction and steepness of the shift varies over the measurements. In figure 4.7 and figures 4.9, 4.10, 4.12 and 4.13, the charge shifts to higher values during the measurement process and the magnetisation to lower values. The measurements for the sample annealed to 373 K and measured in a 500 mT strong magnetic field shows the opposite behaviour (figure 4.8). However for the measurements on the same sample but with a 50 mT strong field (figure 4.11), there is almost no shift visible.

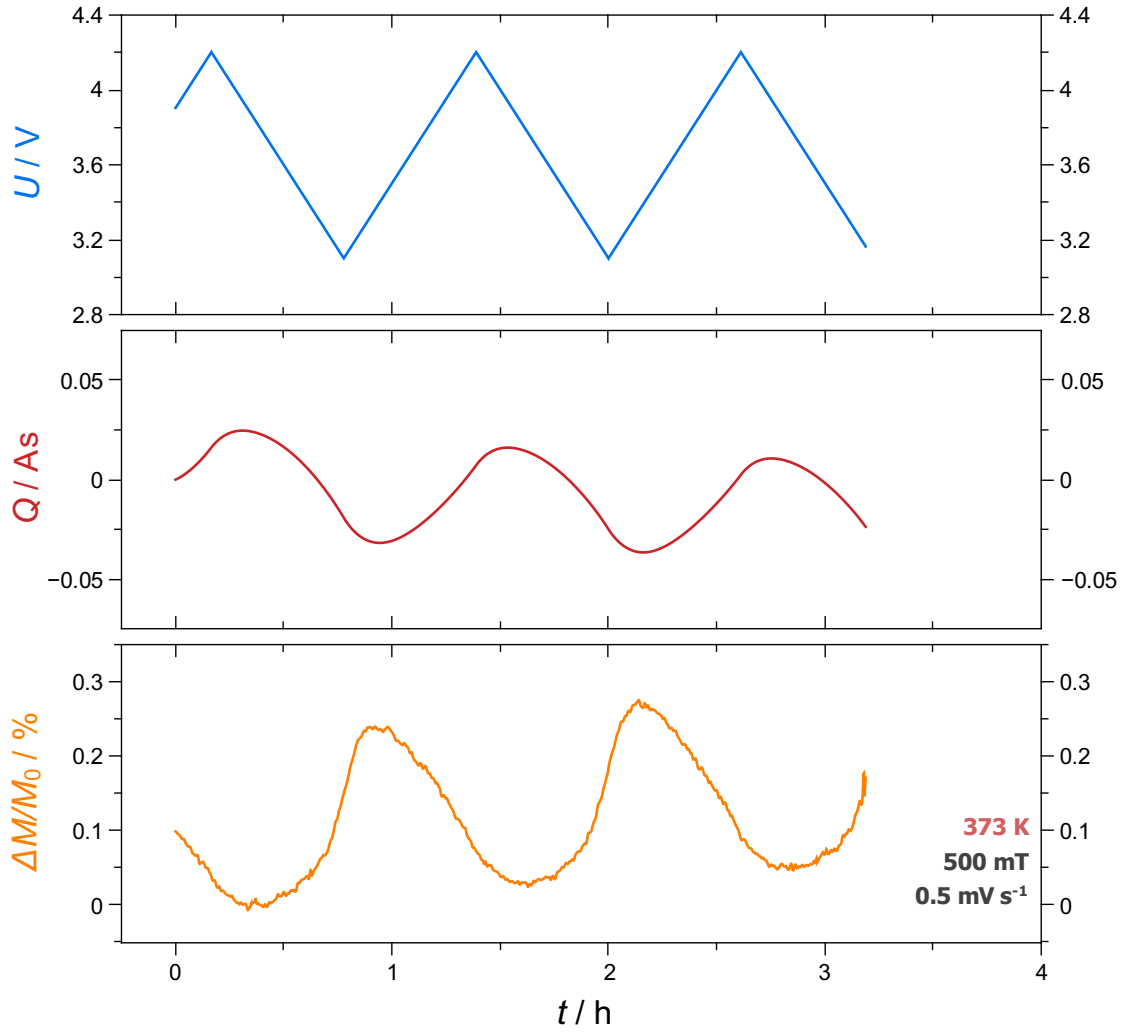

Figure 4.8: Voltage U, charge Q, and corresponding relative change in magnetisation $\frac{\Delta M}{M_0}$ as a function of time t upon *in situ* cycling, for nanoporous palladium, annealed to 373 K, in the pseudocapacitive regime of $LiPF_6$/EC/EMC. Magnetic field: 500 mT, scan rate: 0.5 mV s^{-1}.

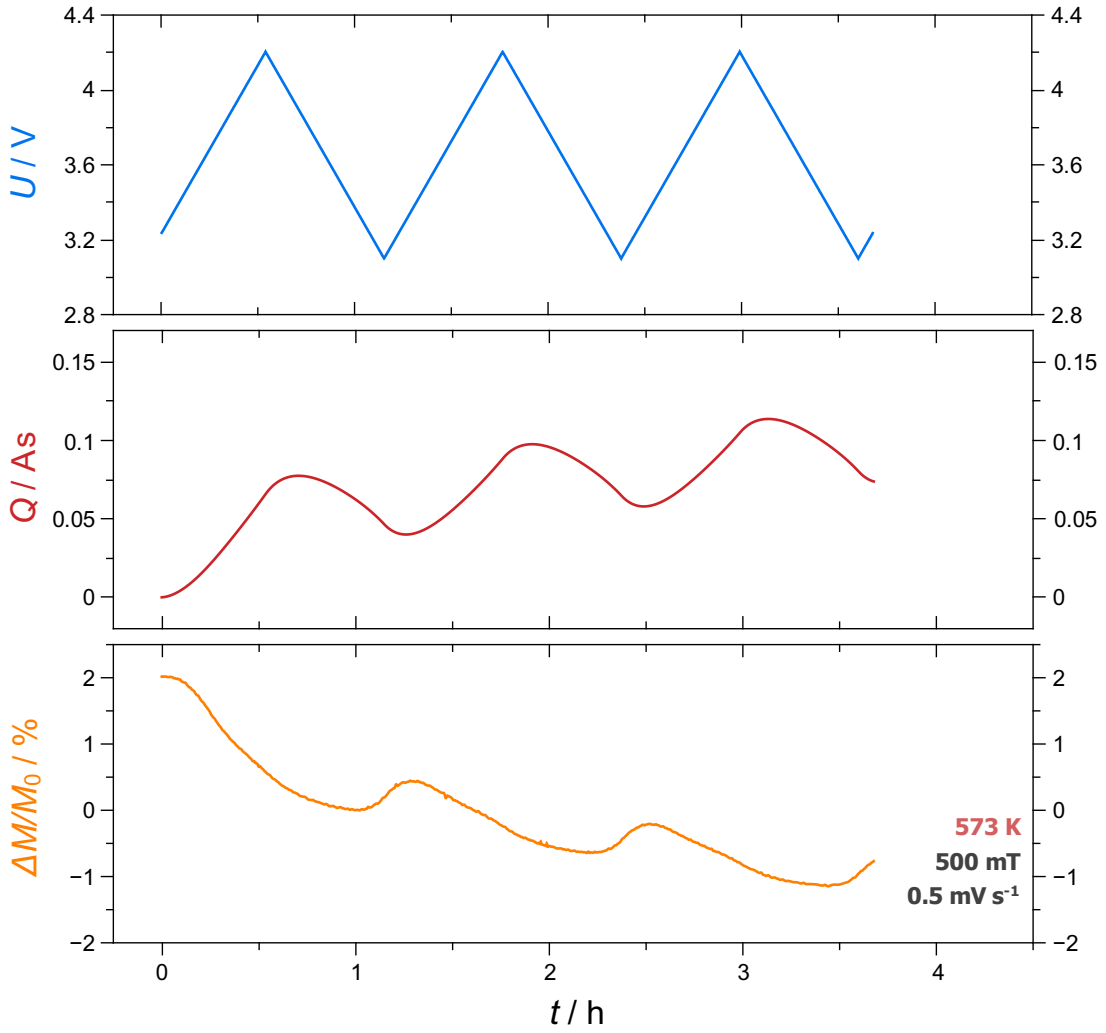

Figure 4.9: Voltage U, charge Q, and corresponding relative change in magnetisation $\frac{\Delta M}{M_0}$ as a function of time t upon *in situ* cycling, for nanoporous palladium, annealed to 573 K, in the pseudocapacitive regime of $LiPF_6$/EC/EMC. Magnetic field: 500 mT, scan rate: 0.5 mV s^{-1}.

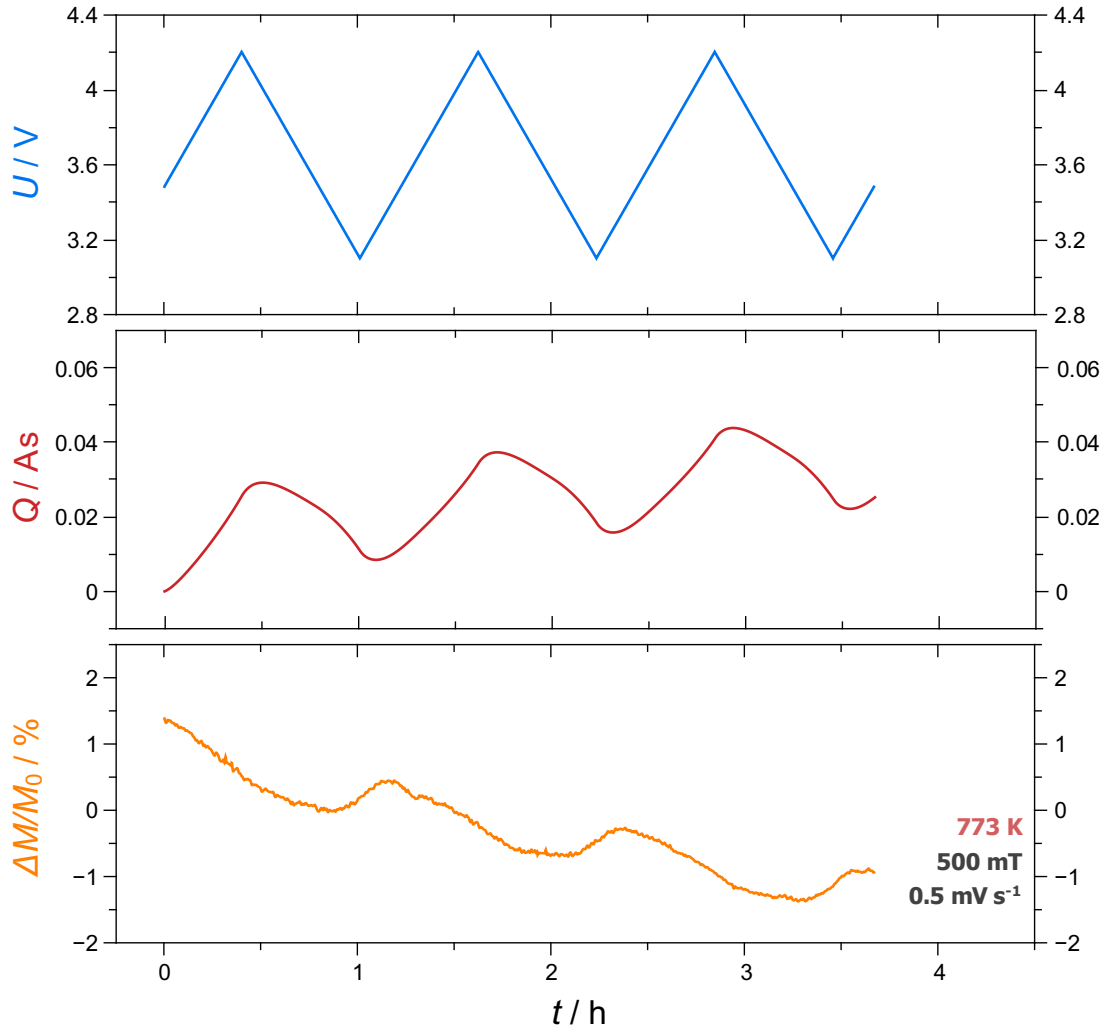

Figure 4.10: Voltage U, charge Q, and corresponding relative change in magnetisation $\frac{\Delta M}{M_0}$ as a function of time t upon *in situ* cycling, for nanoporous palladium, annealed to 773 K, in the pseudocapacitive regime of $LiPF_6$/EC/EMC. Magnetic field: 500 mT, scan rate: 0.5 mV s^{-1}.

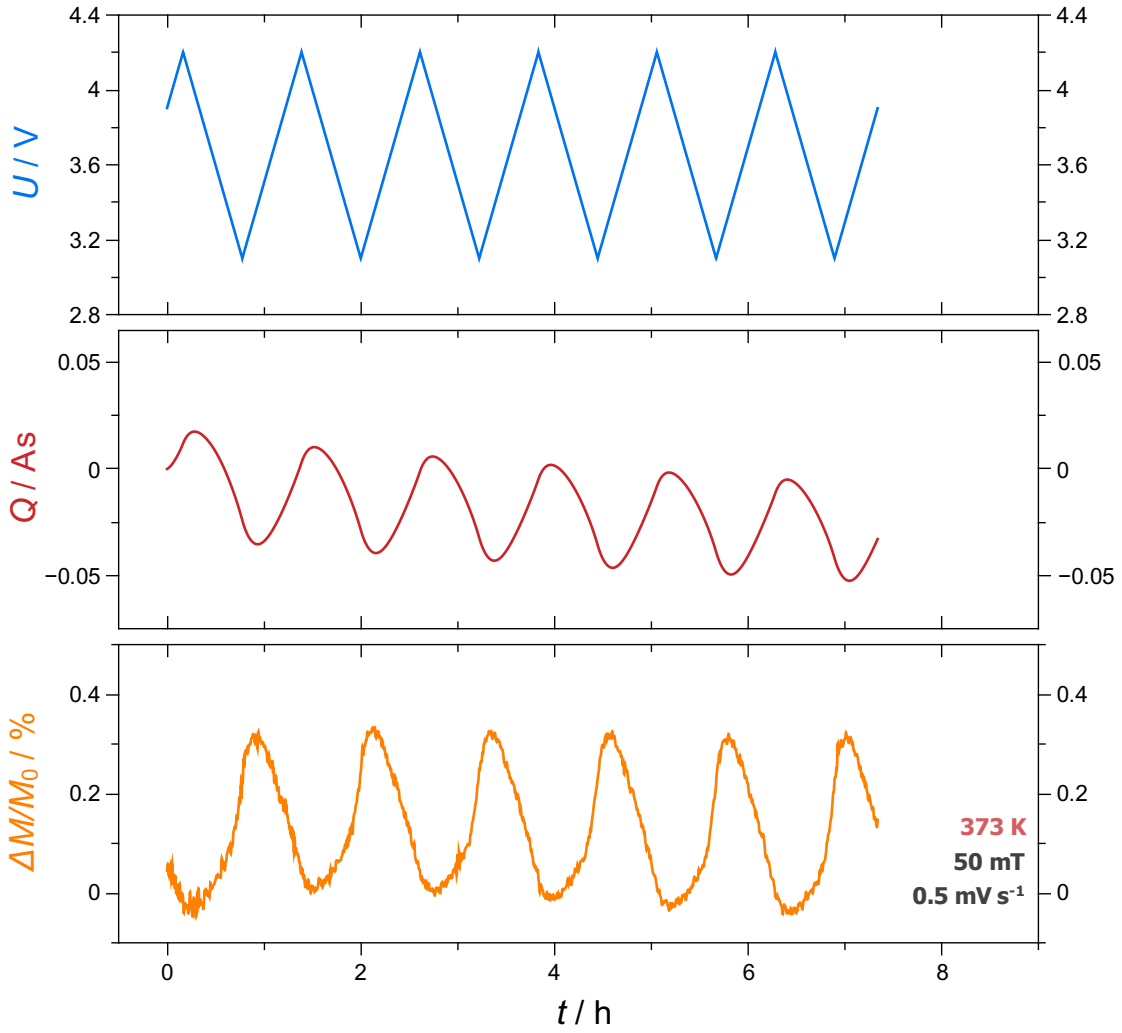

Figure 4.11: Voltage U, charge Q, and corresponding relative change in magnetisation $\frac{\Delta M}{M_0}$ as a function of time t upon *in situ* cycling, for nanoporous palladium, annealed to 373 K, in the pseudocapacitive regime of $LiPF_6$/EC/EMC. Magnetic field: 50 mT, scan rate: 0.5 mV s^{-1}.

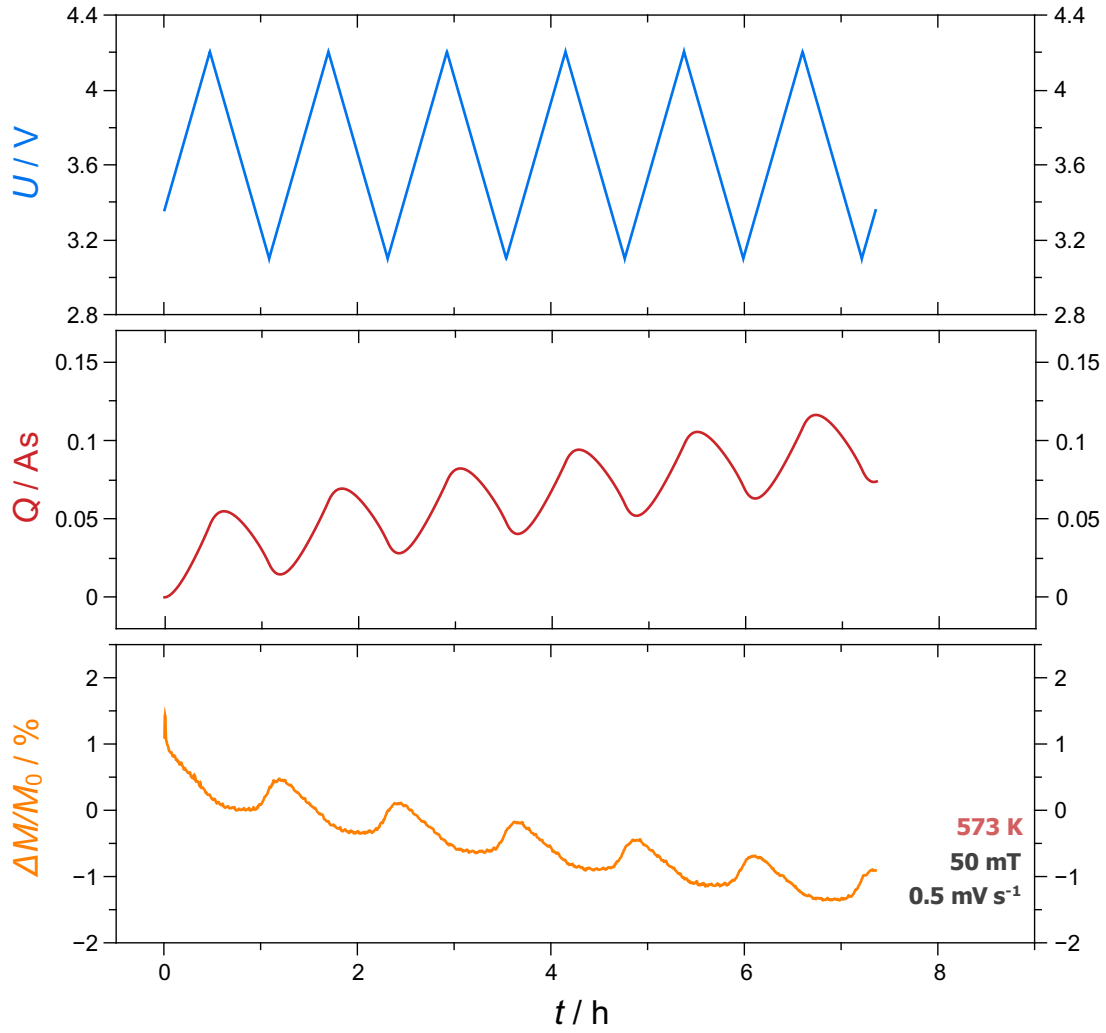

Figure 4.12: Voltage U, charge Q, and corresponding relative change in magnetisation $\frac{\Delta M}{M_0}$ as a function of time t upon *in situ* cycling, for nanoporous palladium, annealed to 573 K, in the pseudocapacitive regime of $LiPF_6$/EC/EMC. Magnetic field: 50 mT, scan rate: 0.5 mV s^{-1}.

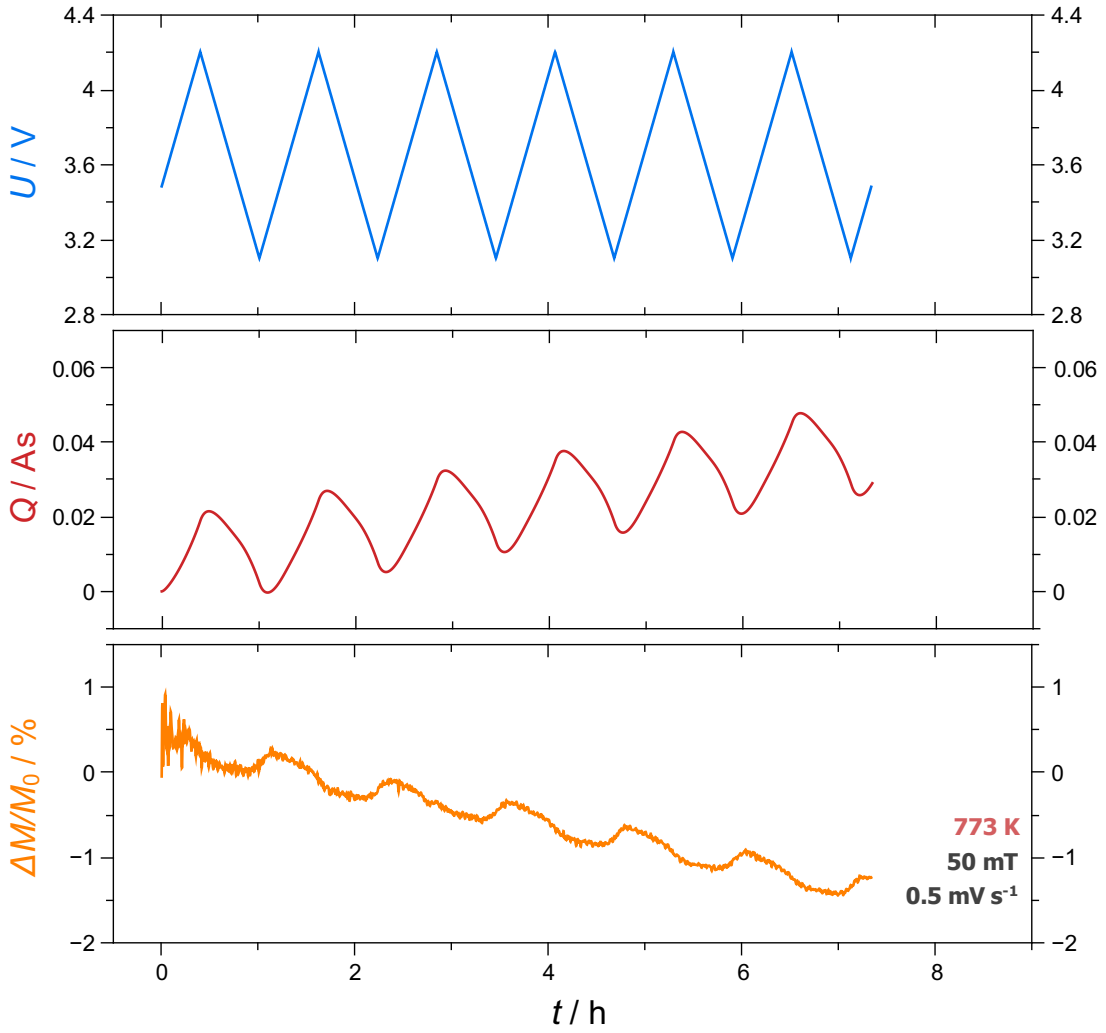

Figure 4.13: Voltage U, charge Q, and corresponding relative change in magnetisation $\frac{\Delta M}{M_0}$ as a function of time t upon *in situ* cycling, for nanoporous palladium, annealed to 773 K, in the pseudocapacitive regime of $LiPF_6$/EC/EMC. Magnetic field: 50 mT, scan rate: 0.5 mV s^{-1}.

4.2.2 KOH as an Electrolyte

In the following section, the measurements of np-Pd(Co) in KOH for charge and relative change in magnetisation under an altering applied potential are presented. The first part deals with a charging in the range of -0.4 to $-0.5\,\mathrm{V}$, which corresponds to a pseudocapacitive behaviour, while the second part pays attention to a potential range (-0.4 to $-0.7\,\mathrm{V}$) where hydrogen adsorption occurs additionally.

Pseudocapacitive Behaviour

Variation of charge and relative magnetisation change in dependence of time upon voltage cycling in the potential range of -0.4 to $-0.5\,\mathrm{V}$ can be seen in figures 4.14 to 4.17. The measurements with a scan rate of $0.1\,\mathrm{mV\,s^{-1}}$ are presented, instead of the $0.1\,\mathrm{mV\,s^{-1}}$-scan rate measurements like in the organic electrolyte, because a jump in magnetisation appeared for a few measurements with $0.5\,\mathrm{mV\,s^{-1}}$ scan rate. This jump is most likely attributed to the necessary refill process of helium in the SQUID apparatus which was performed when some of the $0.5\,\mathrm{mV\,s^{-1}}$-measurements were paused. The triangular shape of the voltage is only shown for the unannealed sample (figure 4.14), since in contrast to the $LiPF_6$-based electrolyte, only a negligible delay between voltage and charge occurs. Also the magnetisation seems to have no delay with respect to voltage. The minima of the charge are at the same time as the maxima of the magnetisation and consequently the magnetisation follows an electron accumulation. In contrast to the measurement in $LiPF_6$/EC/EMC, the CVs in KOH have a more rectangular shape and almost no delay occurred. This is a consequence of a non ideal pseudocapacitive behaviour and can be seen in a comparison of figure 5.7 with figure 5.4.

For the measurements of the relative change in magnetisation, the first non-drifting minimum (stable minima) was set to zero. The amplitudes of the change in magnetisation show no such clear correlation to the annealing temperatures as the measurements in the organic electrolyte. The magnitude of magnetisation change for the unannealed sample and the 373 K-annealed sample (figures 4.14 and 4.15) is about the same, around 0.6 %, while the change of the other two samples is slightly lower (about 0.5 %).

In all measurements, the amplitude of charge and magnetisation change stays about the same over time and a noticeable drift is observable. The magnetisation has a weaker shift

than the charge. In opposite to the measurements of Pd(Co) in $LiPF_6$/EC/EMC (section 4.2.1), in the measurements in KOH, the shifts are not always of constant steepness and direction. The sample annealed to 573 K (figure 4.16) shows a small drift of magnetisation in positive direction, which becomes less steep as time passes. For the annealing temperature of 773 K, figure 4.17, the opposite is visible. The magnetisation change of the as-received sample, seen in figure 4.14, even shows first a weak downward drift and then a weak upward drift. However the drift of the charge is almost constant for all samples. Only at 573 K, figure 4.16, a slight drift of the charge is visible. Also noticeable is, that the drift in charge is not always of opposite direction than the drift in magnetisation (figure 4.17), like it is the case for the previous measurements of Pd(Co) in $LiPF_6$/EC/EMC.

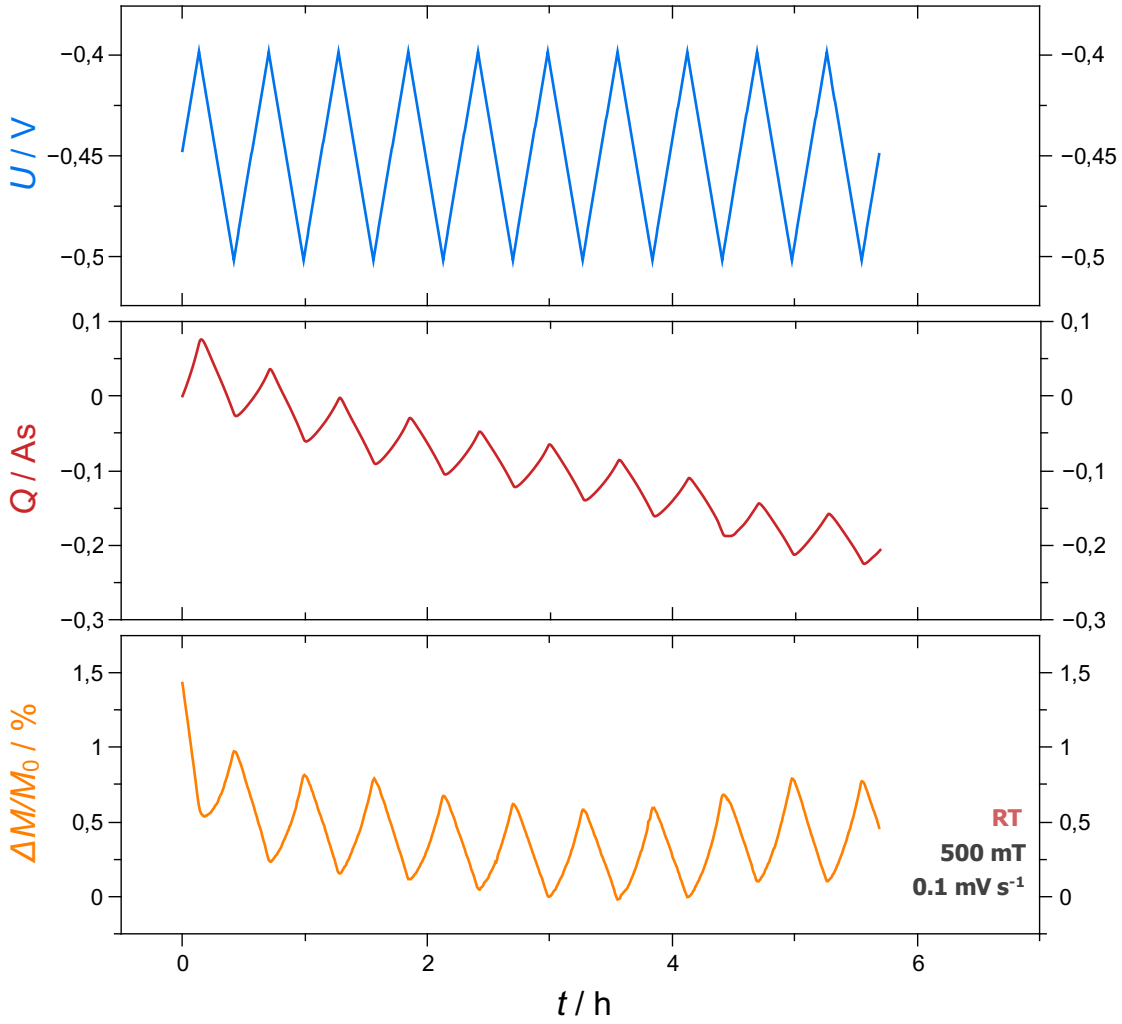

Figure 4.14: Voltage U, charge Q, and corresponding relative change in magnetisation $\frac{\Delta M}{M_0}$ as a function of time t upon *in situ* cycling, for as-dealloyed nanoporous palladium in the pseudocapacitive regime of KOH. Magnetic field: 500 mT, scan rate: 0.1 mV s^{-1}.

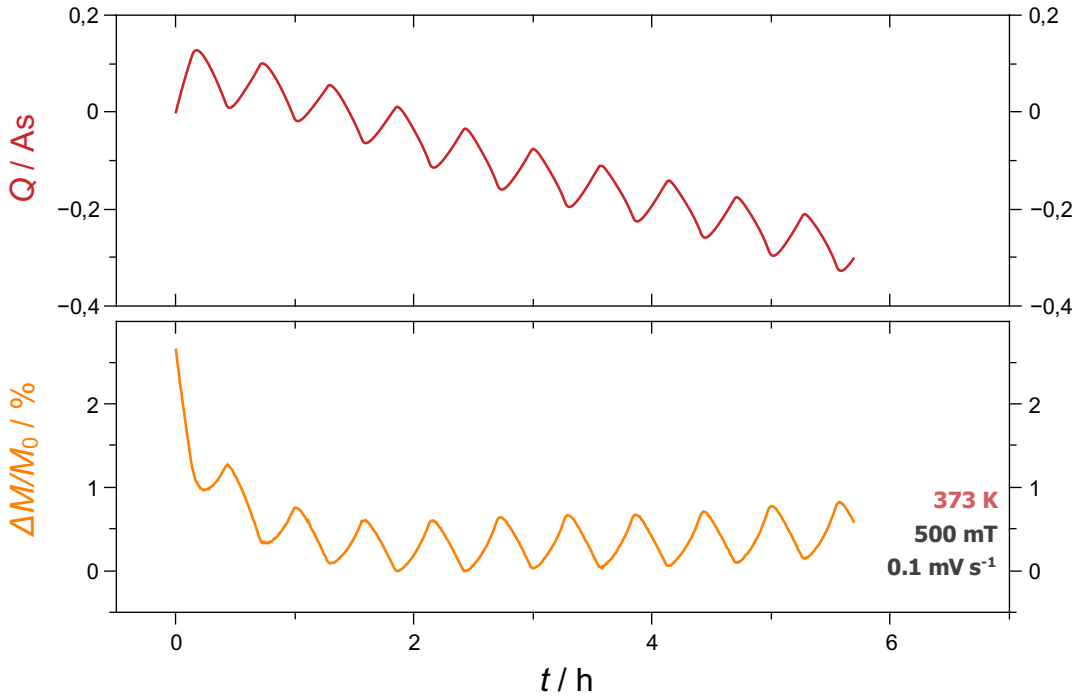

Figure 4.15: Charge Q, and corresponding relative change in magnetisation $\frac{\Delta M}{M_0}$ as a function of time t upon *in situ* cycling, for nanoporous palladium, annealed to 373 K, in the pseudocapacitive regime of KOH. Magnetic field: 500 mT, scan rate: 0.1 mV s^{-1}.

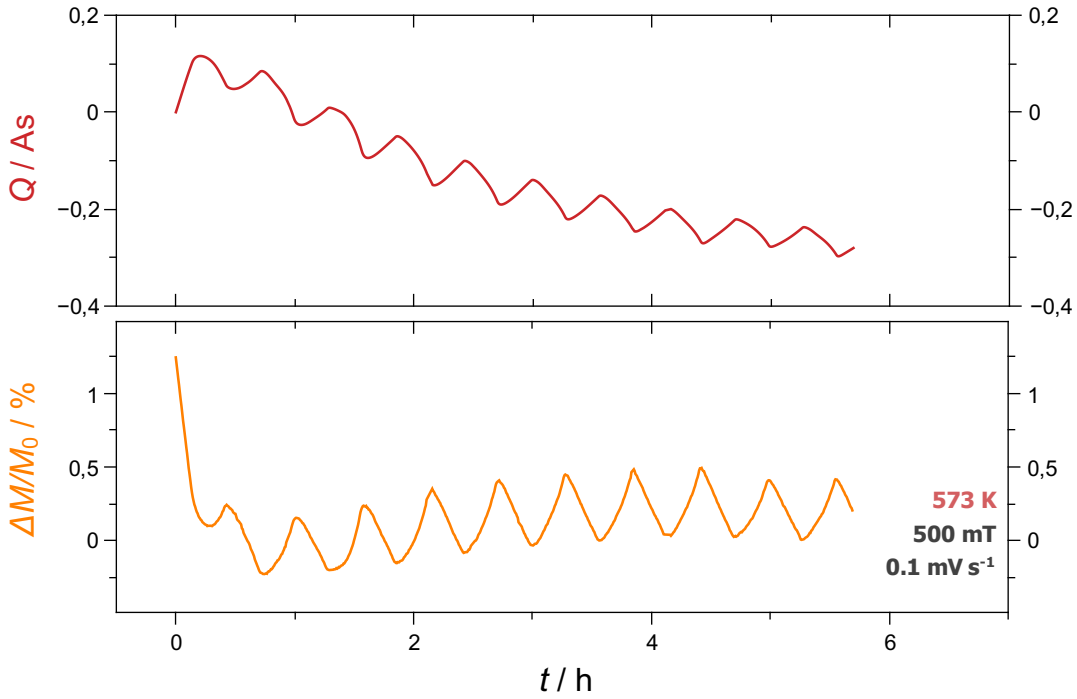

Figure 4.16: Charge Q, and corresponding relative change in magnetisation $\frac{\Delta M}{M_0}$ as a function of time t upon *in situ* cycling, for nanoporous palladium, annealed to 573 K, in the pseudocapacitive regime of KOH. Magnetic field: 500 mT, scan rate: 0.1 mV s^{-1}.

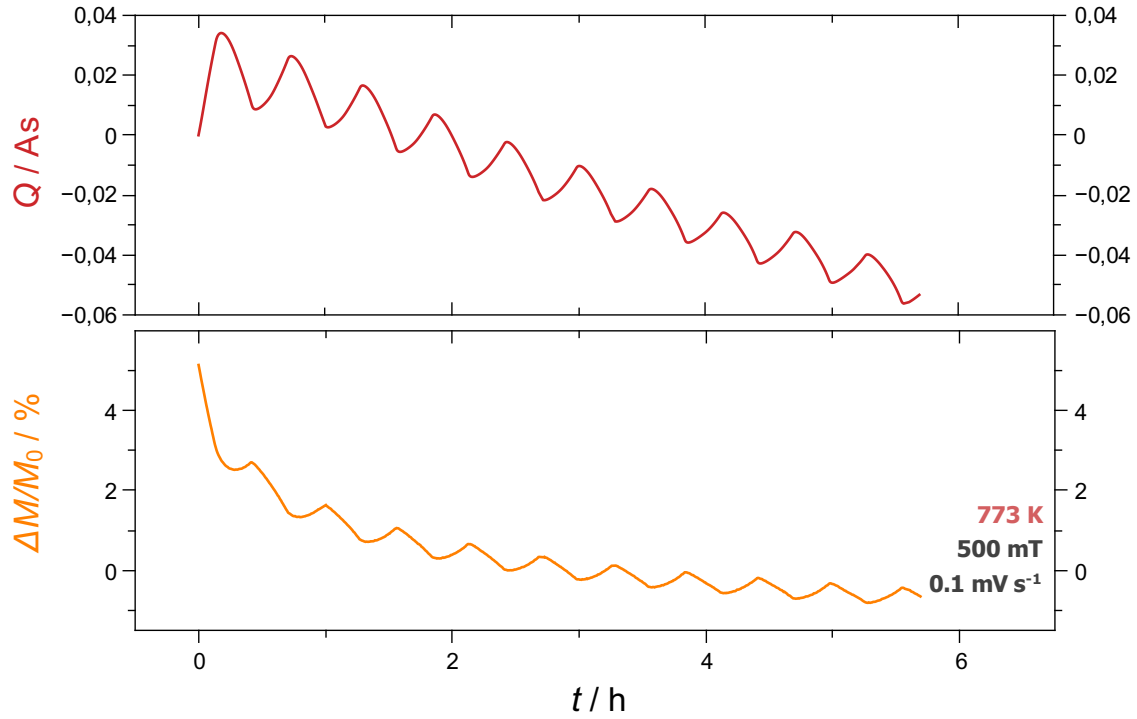

Figure 4.17: Charge Q, and corresponding relative change in magnetisation $\frac{\Delta M}{M_0}$ as a function of time t upon *in situ* cycling, for nanoporous palladium, annealed to 773 K, in the pseudocapacitive regime of KOH. Magnetic field: 500 mT, scan rate: 0.1 mV s^{-1}.

Hydrogen Adsorption

The measurements for voltage, charge and relative magnetisation change in the potential range of -0.4 to $-0.7\,\mathrm{V}$, corresponding to a regime of hydrogen ad- and desorption, are displayed in figures 4.18 to 4.21. The triangular shape of the voltage is again only displayed for the as-received sample (figure 4.18). The maxima of the charge are again synchronised with the maxima of the voltage and consequently with the minima of the relative magnetisation change.

The amplitude of charge stays about the same over time and has almost the same height in all measurements (about $0.4\,\mathrm{A\,s}$). Only the sample annealed to $773\,\mathrm{K}$, seen in figure 4.21, shows a slightly lower amplitude of charge. The amplitude of the relative magnetisation stays also almost the same for each measurement. However in relation to each other, the reachable maximal magnetisation differs. While the sample annealed to $573\,\mathrm{K}$, and the unannealed one, figures 4.18 and 4.20, have a magnetisation change of about $2.8\,\%$, for an annealing temperature of $373\,\mathrm{K}$, a change of about $4.0\,\%$ is reached and for $773\,\mathrm{K}$ about $4.6\,\%$. With the exception of the sample annealed to $573\,\mathrm{K}$, the relative change in magnetisation increases with higher annealing temperature.

Further, it can be seen that also in this potential range a drift occurs. However, only the charge seems to drift noticeable. In all measurements, a slight drift of the charge into negative direction is observable, while the relative change in magnetisation shows no significant drifting. Only in the measurement of the unannealed sample, displayed in figure 4.18, a minor drift during the first hour is visible. Additionally, for the same measurement, it can be seen that the drift of the charge first goes into positive direction during the first hour and then in the negative direction. The drift in charge and magnetisation change behaves the same in this measurement (figure 4.18), in relation to steepness and direction change, but the drifts are of opposite direction.

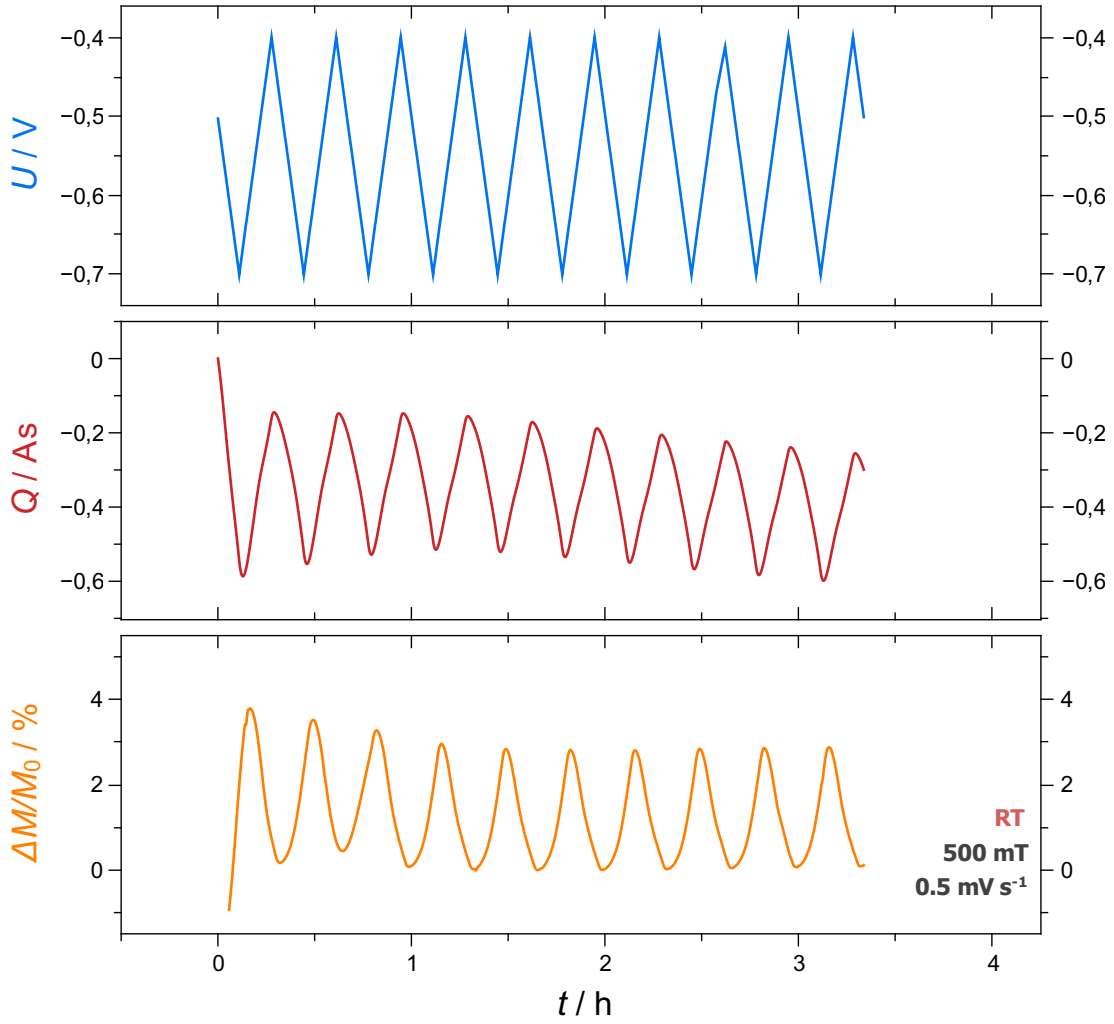

Figure 4.18: Voltage U, charge Q, and corresponding relative change in magnetisation $\frac{\Delta M}{M_0}$ as a function of time t upon *in situ* cycling, for as-dealloyed nanoporous palladium in the hydrogen-adsorption regime of KOH. Magnetic field: 500 mT, scan rate: 0.5 mV s^{-1}.

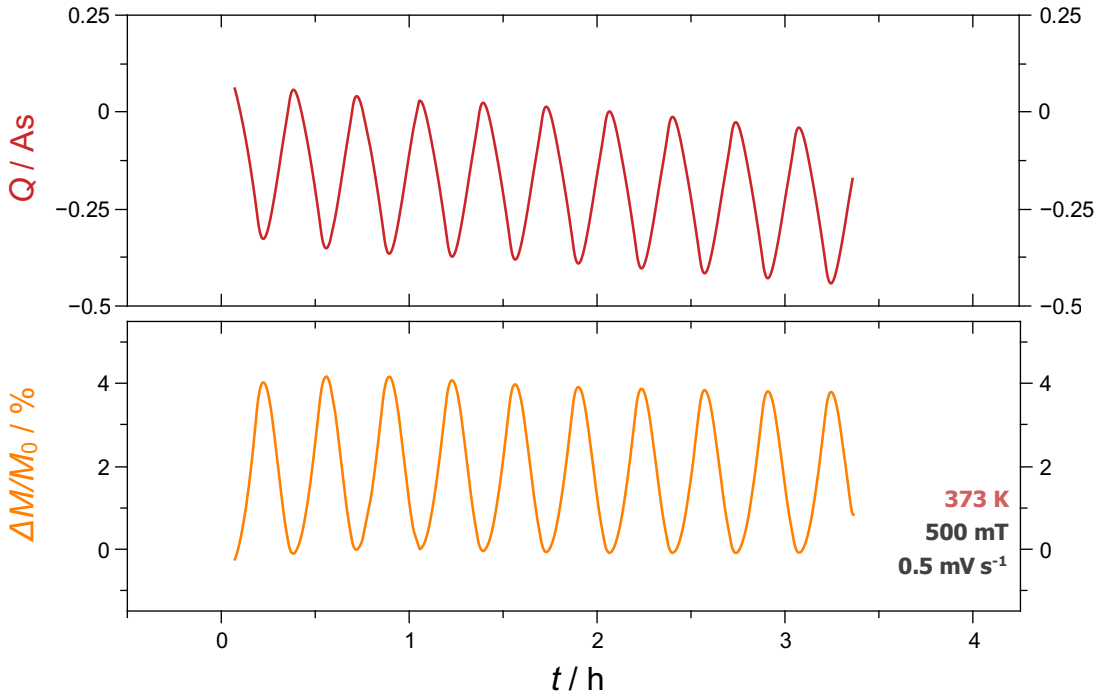

Figure 4.19: Charge Q, and corresponding relative change in magnetisation $\frac{\Delta M}{M_0}$ as a function of time t upon *in situ* cycling, for nanoporous palladium, annealed to 373 K, in the hydrogen-adsorption regime of KOH. Magnetic field: 500 mT, scan rate: 0.5 mV s^{-1}.

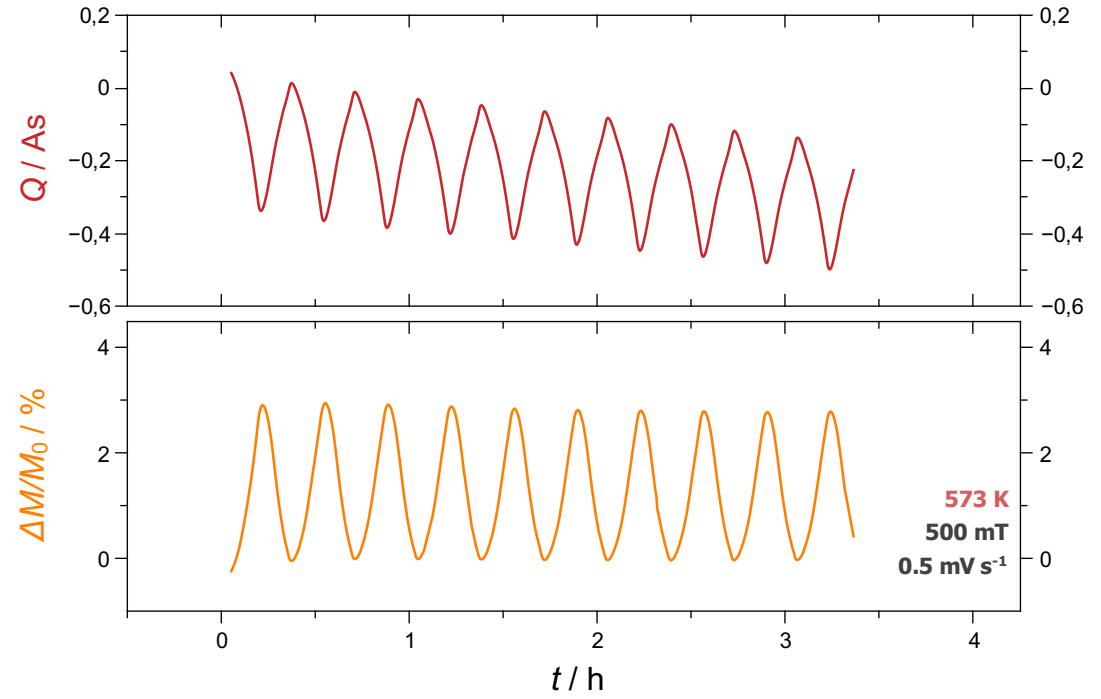

Figure 4.20: Charge Q, and corresponding relative change in magnetisation $\frac{\Delta M}{M_0}$ as a function of time t upon *in situ* cycling, for nanoporous palladium, annealed to 573 K, in the hydrogen-adsorption regime of KOH. Magnetic field: 500 mT, scan rate: 0.5 mV s^{-1}.

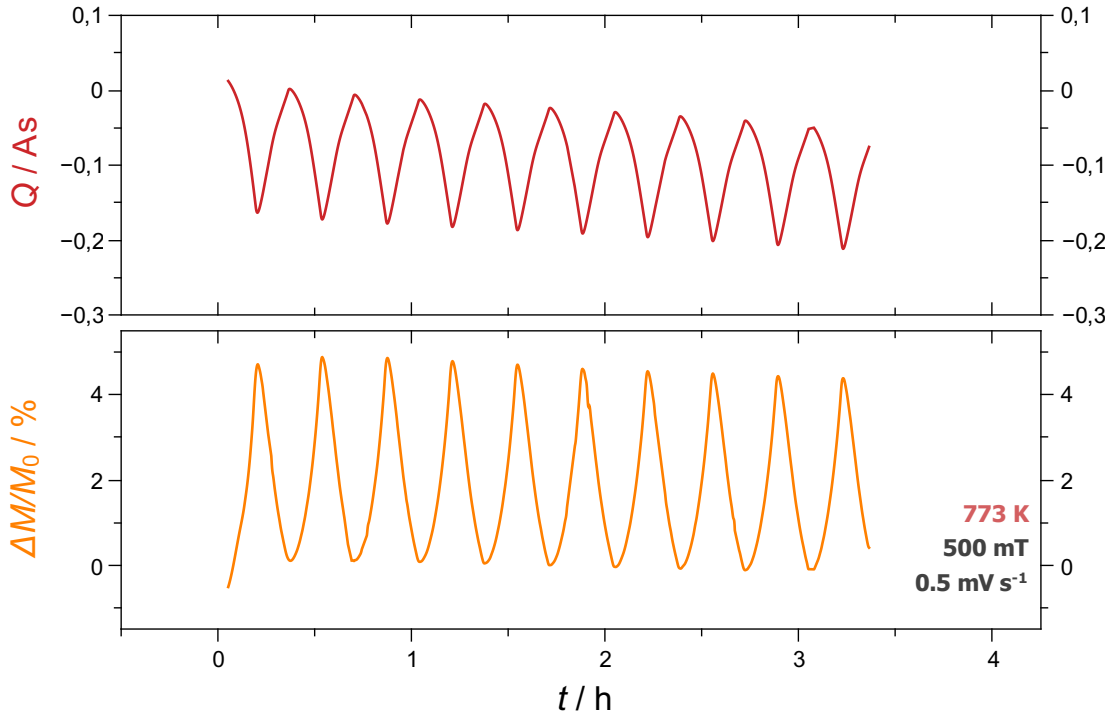

Figure 4.21: Charge Q, and corresponding relative change in magnetisation $\frac{\Delta M}{M_0}$ as a function of time t upon *in situ* cycling, for nanoporous palladium, annealed to 773 K, in the hydrogen-adsorption regime of KOH. Magnetic field: 500 mT, scan rate: 0.5 mV s^{-1}.

Chapter 5

Discussion

5.1 Intrinsic Magnetic Properties of Nanoporous Palladium

5.1.1 Magnetisation Measurements

In this section the measurement of magnetisation for a temperature of 4.2 K, figure 4.1 and 300 K, figure 4.2, will be discussed with respect to the occurring trends in saturation magnetisation, coercivity and remanent magnetisation.

Magnetisation at 4.2 K

The hysteresis loop in the magnetisation measurements at 4.2 K shown in figure 4.1, below the blocking temperature, implies that the nanoporous palladium is ferromagnetic in this temperature range. Due to the fact that by thermal coarsening the ligament size increases, as seen in table 4.2, a rise in saturation magnetisation with higher coarsening temperatures could be expected, similar to what is known for various ferromagnetic nanoparticles [45–49]. On the one hand, this size dependence of saturation magnetisation for nanoparticles can be explained in terms of a core-shell model, which is introduced later. On the other hand the anisotropy energy has also an influence. The proportional dependence of the anisotropy energy E_A of a magnetic particle to its volume causes smaller particle to switch easier. If their energy is in range of the thermal energy, the magnetisation experiences a significant

reduction due to thermal fluctuation. Anisotropy energy would also imply that a larger ligament size causes a higher saturation magnetisation, as reported by the group of Hakamada for nanoporous nickel[50]. As it can be seen in figure 4.1, this is clearly not the case for np-Pd(Co). The saturation magnetisation decreases with higher degree of coarsening, most significantly beyond 773 K annealing temperature. It is assumed that ligament size is not the decisive factor for the value of magnetisation in nanoporous palladium, but rather the residual content and distribution of Co, the sacrificial element during dealloying. In opposite to the work of Hakamada et al., where a master alloy of NiMn (25:75 at%) was used and dealloyed to nanoporous Ni, our samples contained the magnetic phase Co only as a secondary element in the Pd structure, which were dealloyed out of a CoPd (75:25 at%) alloy. The nanoporous palladium samples do not consist out of pure palladium but have a certain content of residual cobalt[51]. The amount of residual cobalt was determined via a XRF measurement to about 8.7 at%, as shown in section 3.2. The saturation magnetisation is influenced by the total amount of Co and the local distribution of the residual cobalt. Krekeler et al. have shown for np-Au(Ag) (residual Ag content of about 5 at%) that the silver cluster distribution changes via a temperature treatment[12]. As the total cobalt concentration does not change upon coarsening, it implies that the cobalt distribution influences the saturation magnetisation.

The effect of cobalt concentration on the magnetoresistance in dilute PdCo alloys was studied by Hamzić and Campbell[52]. They studied palladium cobalt alloys with different amounts of homogeneously distributed cobalt and reported that the concentration of cobalt in the palladium nanostructure has a decisive influence on the magnetic behaviour. It was shown, that lowering the temperature further, after a ferromagnetic state is reached and all spins are aligned, spins begin to disalign[52]. Although a spin glass state was not found, a disalignment of the spins was detected, even at a cobalt concentration of 5 at%[52]. One possible explanation for the spin disalignment given by Hamzić and Campbell was a interaction with random sign between the single spins. As the RKKY coupling is known to be active in CoPd alloys, the disalignment could be a result of the RKKY interaction which leads to a ferromagnetic or antiferromagnetic coupling, dependent on the distance between two Co atoms. One Co atom can lie both, in a maximum and in a minimum of the RKKY interaction with respect to two neighbouring Co atoms, as the distances between Co atoms are random after

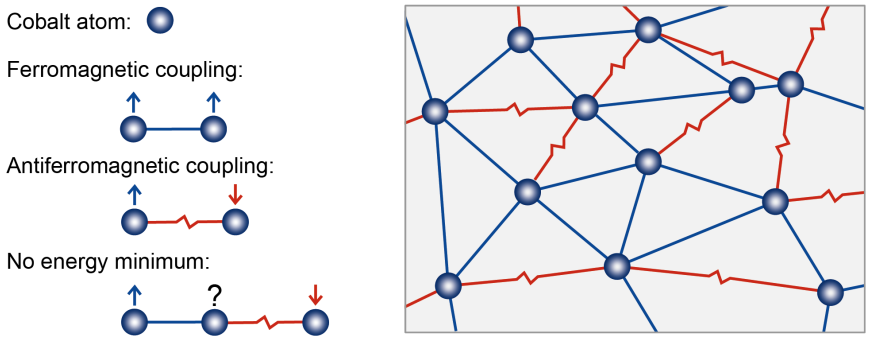

Figure 5.1: Simplified representation of frustrated spin states due to the random distance between cobalt atoms as a result of homogenisation of cobalt concentration.

annealing. As a consequence of competing interactions from different atomic neighbours no clear energy minimum occurs, but a frustrated state with disaligned spins emerges. An illustration of this phenomena is displayed in figure 5.1. There are more disoriented spins as the local cobalt concentration becomes lower. As cobalt begins to redistribute in the sample, via heating, spins become more and more disaligned, which leads to a decrease in saturation magnetisation.

Although the Co concentration in our samples remains globally constant, local Co concentration changes due to the annealing and the following redistribution of Co atoms. Since in our measurements the magnetisation decreases with larger ligament size, it can be assumed that the random distribution of the magnetic cobalt atoms in the nanoporous palladium samples has a much stronger influence on the magnetisation than the ligament size. We can differentiate two magnetic phases, with a continuous transition between them, which determine the magnetisation: Co-rich phase in which clusters of cobalt act like superparamagnets and a phase of diluted CoPd alloy as frustrated spin material. The dilute-Co phase emerges from the cluster phase upon temperature treatment and grows at its expense. The redistribution of Co atoms upon thermal coarsening is schematically depicted in figure 5.2.

Initially cobalt exists as clusters embedded in the Pd structure. Upon annealing, Co atoms begin do distribute over the matrix, which leads to a shrinking of the clusters and to a disalignment of the spins of surrounding atoms. Both reduce the magnetisation. As cobalt distributes further over the structure, the core starts to decouple progressively from the shell until two separate magnetic phases emerge. These two phases are, on the one hand, the

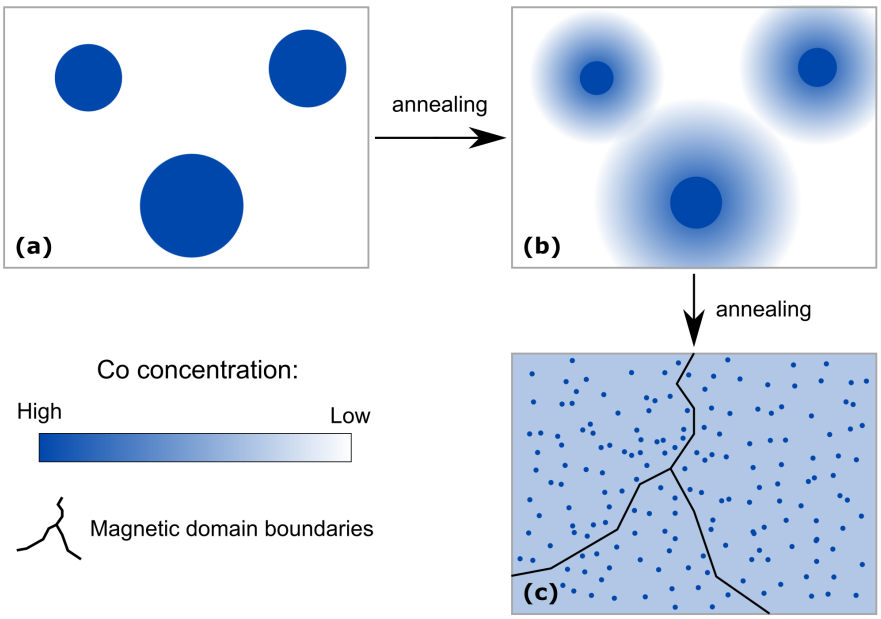

Figure 5.2: Illustration of homogenisation of cobalt concentration due to annealing. (a) Cluster phase: Co atoms lie as clusters in the Pd structure. (b) Co distribute over the structure and two phases begin to coexist. (c) Dilute-Co phase: Co atoms are homogeneously distributed in the Pd structure.

strongly coupled core in which direct exchange might still play a role and, on the other hand, a dilute phase in which RKKY coupling is the dominant interaction. Finally cobalt is fully diluted in the structure, a homogeneous Co distribution is reached and frustrated states are present all over the structure. Flipping of the cluster moment at lower temperatures contributes also to the reduction of magnetisation. Thus, the magnetic two-phase model can account for the lowering in magnetisation upon annealing of np-Pd(Co).

A comparison of the received saturation magnetisations at 4.2 K with the work of Bozorth et al.[22] supports the picture that Co in np-Pd(Co) never attained a fully diluted state in the Pd matrix (even in the one annealed to 973 K). Bozorth et al. measured magnetic properties of solid cobalt-palladium solutions with different Co concentrations. If we compare the saturation magnetisation of the as-dealloyed sample at 4.2 K (seen in figure 4.1), with a Co concentration of 8.7 at% (measured with XRF, seen in section 3.2), with their data for 8.7 at% Co, it can be seen, that the received value is (much) smaller than the value reported by Bozorth et al. While in the present work, a saturation magnetisation of 10.56 emu g^{-1} was measured (values seen in table 4.1), in their work, they received a saturation magnetisation of about 0.46 μ_B per alloy atom for 8.7 at% Co, which corresponds to magnetisation around

$25\,\mathrm{emu\,g^{-1}}$. Since in the as-dealloyed sample, the Co is assumed to lie as clusters in the Pd matrix and Bozorth et al. used a PdCo alloy with a homogeneous Co distribution, one could suggest that this difference in distribution is responsible for the difference in saturation magnetisation. But, we have seen in figure 4.1, that the saturation magnetisation decreases with higher annealing temperature and thus with higher homogenisation of Co. So it is suggested, that even with an annealing temperature of 973 K, the Co distribution is not sufficiently homogeneous to show bulk properties. However, annealing to even higher temperatures must eventually increase the saturation magnetisation as bulk behaviour must be recovered. An other possible explanation might be, that the XRF measurement may overestimate the residual Co content, since spectra, gained from energy-dispersive X-ray spectroscopy (EDXS), of similar samples, yield smaller concentration values [51].

From table 4.1 it can be seen, that at a coarsening temperature of 973 K a saturation magnetisation of only about $0.7\,\mathrm{emu\,g^{-1}}$ is reached. A lowering in remanent magnetisation, which was also observed, is a consequence of the decrease of saturation magnetisation. The measured decrease of coercivity, beyond an annealing temperature of 773 K, is a hint that the frustrated states of disaligned magnetic moments are so significant (at this grade of cobalt dilution), that there is no strong preference of one preferable magnetic orientation. It can be assumed that the local cobalt concentration is homogenised by heat treatment, effectively diluting the cobalt atoms in the palladium matrix. Higher temperature samples can therefore be viewed as more dilute PdCo alloys.

In conclusion, np-Pd(Co) is ferromagnetic at 4.2 K at all measured coarsening degrees. The saturation magnetisation decreases upon coarsening which is a consequence of the internal Co distribution. Due to annealing, residual Co distributes over the structure, resulting in frustrated states which lowers the saturation magnetisation. So, two separate magnetic phases can be distinguished. As Co distributes upon annealing, a dilute-Co phase emerges at expense of a rich-Co phase.

Magnetisation at 300 K

In opposite to the magnetisation at 4.2 K, in the measurement at 300 K, seen in figure 4.2, no hysteresis loop is visible and a remanent magnetisation and a coercivity near zero is observed, which results in a sigmoidal M-$\mu_0 H$-curve. These are typical characteristics of

a superparamagnetic behaviour and hence imply single domain particles. Coercivity values below 2 mT for samples annealed to temperatures lower than 773 K are in the measurement uncertainty. Thus, only the samples annealed to 773 K and 973 K are considered ferromagnetic. A constant magnetisation at higher fields for these samples (773 K and 973 K) confirms this statement. The transition from the superparamagnetism to ferromagnetism bears certain analogies with a magnetic core-shell model[53].

In general, this model states that ferromagnetic nanoparticles consist out of a core of aligned spins and an inactive surface layer which behaves like a spin glass. The disorder in spin orientation of the surface layer modifies the magnetic properties of the whole material. Up to a particular magnetic field, the spins of the core align with the field and the magnetisation increases until a point is reached where all core-spins are aligned. After this point an increase of the magnetic field affects only the surface layer which is reflected in a smaller rise of magnetisation. The M-$\mu_0 H$-curve does not saturate, even at high fields, as a result of disaligned surface-spins. With smaller surface/volume ratio, the influence of the disordered spin layer reduces[53]. For bulk-like structures, the surface layer can not overshadow the spins of the core and the sample becomes ferromagnetic and shows properties like a coercivity and a ferromagnetic saturation.

A sigmoidal, non-saturating magnetisation curve is indeed observable in figure 4.2 for annealing temperatures up to 573 K which suggests that the core-shell model might also be applied to a nanoporous structure like dealloyed CoPd. As it is seen in figure 2.4 for a AgAu alloy, the nanoporous structure consists of the inner less-noble clusters, in our case Co clusters, and the surrounding more-noble species, here Pd. The inner Co clusters represent the ferromagnetic cores which are surrounded by the Pd layer with disordered spins.

However, in contrast to the original core-shell model, the Co core in the nanoporous palladium structure additionally polarises some of the surrounding Pd atoms, depending on the Co concentration (exchange-enhanced RKKY interaction), which enhances the effective cluster size. A rising magnetic field first leads to a strong increase of magnetisation, by aligning the spins of the core. When spins of the core are aligned, a slower increase follows which originates from the spin alignment of the remaining surrounding Pd atoms.

The ferromagnetic behaviour beyond 773 K annealing temperature, which includes a fer-

romagnetic saturation as well as the presence of a low coercivity, may be explained by the redistribution of Co atoms due to the temperature treatment. During the annealing procedure, the Co cluster begin to dissolve in the Pd structure and the core-shell structure vanishes. This leads to a more homogeneous Co distribution, which results in a superposition of a Co-rich phase and a dilute Co phase, as described for the magnetisation measurement at 4.2 K. Since, the core-shell structure vanished, ferromagnetic saturation occurs. The dilute phase consists of RKKY-coupled domains, which become larger upon further Co distribution (upon annealing). This coupling of atoms over larger regions results in an increase of the coercivity.

5.1.2 Zero Field Cooling and Field Cooling

The magnetisation measurements in ZFC mode differs clearly from the measurement in FC mode, both displayed in figure 4.3. This is an indicator for time-dependent effects. As the samples cools down, in zero magnetic field, the magnetic state at room temperature is frozen. It would be expected that the ZFC curve has a value of zero at the minimum temperature of 4.2 K because the randomly oriented spins, which appear at room temperature and freeze upon cooling, compensate each other. Nevertheless a noticeably negative magnetisation for the ZFC curve at low temperatures occurs. This could be explained that in SQUID, switching from zero to strong positive fields (e.g. 500 mT for sample alignment) can trap low negative fields in the magnet[32].

The magnetisation, in a small field, at low temperatures is dependent on the anisotropy of the system. Since in the ZFC curve at 4.2 K a magnetisation value close to zero is observed, it can be assumed that the small applied field of 5 mT is not sufficient enough to flip the orientation of the spins in the direction of the field. This is also typical for a highly anisotropic system[54]. The absolute value of the ZFC curve at 4.2 K (figure 4.3) reduces with rising coarsening temperature. This reduction in magnetisation could have the same origin as the reduction of magnetisation in the hysteresis measurements at 4.2 K and 300 K, shown in figure 4.1 and 4.2. Co cluster reduce in size and frustrated cobalt atoms distribute over the sample which lowers the net magnetisation. With higher temperature the ZFC magnetisation begins to rise because enough energy is provided to align the spins along the applied field. The increase lasts up until a local maximum, which marks the transition to

the superparamagnetic regime.

This maximum, the so-called blocking temperature, is the temperature value at which the system undergoes an abrupt transition from the superparamagnetic to blocked state on the time scale of the measurement device (for the SQUID, here $\sim$25 s). The clusters have enough thermal energy to flip their magnetic moment during the measurement time. However, actually the temperature at the ZFC peak is only a good approximation for the average blocking temperature, which is typically slightly lower[55]. So, the system develops continuously from the blocked to the superparamagnetic regime which results in two distinct contributions for the ZFC and FC curves. One from blocked and one from superparamagnetic particles.

It is seen that the blocking temperature shifts to lower temperatures as the annealing temperature increases. One could suggest that smaller ligaments may be the cause for this shift, since smaller ligaments need less thermal energy to switch and thus the transition to the superparamagnetic regime happens at lower temperature. However, it is already clear that ligament size increases with annealing temperature[12], which would imply and increase of the blocking temperature what obviously is not the case. A suitable explanation would be again the strong effects of the Co redistribution which appear after annealing. Although the ligament size increases, the dilution of larger clusters in the matrix leads to smaller Co cluster sizes with a sharper size distribution, which allows an easier flip of individual cluster spins. This lowers the blocking temperature for the Co clusters.

Due to the existence of two magnetic phases, the magnetisation curves can be seen as a superposition of the magnetisation due to the cluster phase and due to the dilute phase. The bifurcation, described by the irreversibility temperature is a consequence of the emergence of the dilute phase. Progressively flatter FC curves with annealing temperature, especially at temperatures larger than 773 K, are indicative for the appearance of a coupled magnetic phase[56] which might be the RKKY-coupled dilute phase in our case. As a result, nearly constant FC curves are seen in figure 4.3 with an annealing temperature of 773 K and 973 K. So, temperature treatment leads to a reduced Co cluster size and the emergence of larger domains of the dilute phase. Beyond 773 K annealing temperature, the dilute phase is coupled over large enough regions to cause ferromagnetic behaviour, such as the observed coercivity (figure 4.2) and a flatter ZFC-FC curve (figure 4.3).

As for any superparamagnetic system, above the blocking temperature, magnetisation decreases for all annealing temperatures and the sample is located in the superparamagnetic regime. Thermal energy is sufficient to flip individual moments of some cluster, following a typical paramagnetic law ($m \propto \frac{H}{T}$). With higher temperatures this trend continues and the magnetisation converges to zero where all the moments follow random directions.

The magnetic behaviour, as the sample is cooled down in the presence of an applied magnetic field, can be deduced from the shape of the FC curve. With decreasing temperature more and more particles get their spin locked in a certain direction, determined by the applied field. If the material is of low anisotropy, the magnetisation at FC would remain almost constant, while a highly anisotropic material leads to an increase in magnetisation [54]. The rising magnetisation in the FC curve of the untreated sample and the samples annealed to 373 K and 573 K indicates again the anisotropic nature of the nanoporous palladium sample. However, on the contrary, the annealing to 773 K showed a flatter FC curve and an annealing temperature of 973 K, gives an almost constant FC magnetisation curve, which implies low anisotropy.

Magnetic Anisotropy Energy Distribution and Ligament Size Distribution

As reported from Tournus et al.[55], the difference of ZFC and FC magnetisation can be utilised to evaluate the anisotropy energy and thus the particle size distribution [55]. The range, in which the ZFC curve and the FC curve differ from each other, becomes larger as the sample is coarsened because the irreversibility temperature shifts to higher values. This observation matches with the one of Tournus et al., who stated, that with an increase of particles of larger size distribution, a higher irreversibility temperature and thus a broader peak will follow. To receive a measure for the magnetic anisotropy energy distribution $\rho(E_\mathrm{A})$, the following relation can be used [55]:

$$\rho(E_\mathrm{A}) \propto -\frac{1}{T}\frac{\mathrm{d}\Delta M}{\mathrm{d}T}\,, \tag{5.1}$$

where ΔM is the difference in magnetisation between the ZFC and the FC curve (M_FC-M_ZFC). This relation applies also to the crossover temperature distribution, which is almost identical to the blocking temperature distribution, and to the particle size distribution,

assuming the particles have a spherical shape and the anisotropy constant is known. The correlation between the blocking temperature, the volume and the anisotropy energy can be seen in equation 2.3. It is noted that for different sized clusters, different anisotropy constants are possible[57], which means that also the the anisotropy constant is distributed. So the magnetic anisotropy energy distribution corresponds to a combination of anisotropy constant distribution and particle size distribution. The magnetic anisotropy energy distribution, for all samples, is shown in figure 5.3. It should be noted, that the jump-like scattering at the curves arise from the derivation (equation 5.1) and the amplification of noise associated with this procedure.

The distribution is displayed for nanoporous palladium samples, subjected to thermal treatment at different temperatures. A Gaussian distribution (blue) was fitted to the data. A clear shift of the maximum of the peak and a narrowing of the distribution, is indicated by a decrease in variance σ of the Gaussian. This indicates a reduction of the anisotropy energy and thus the Co cluster size with T_{A}. This agrees well with the Co cluster shrinking due to dilution reported in this work. At an annealing temperature of 973 K the distribution shows only a small remaining peak at low temperatures. At this state Co atoms are almost fully diluted in the Pd matrix and a nearly homogeneous Co distribution is reached.

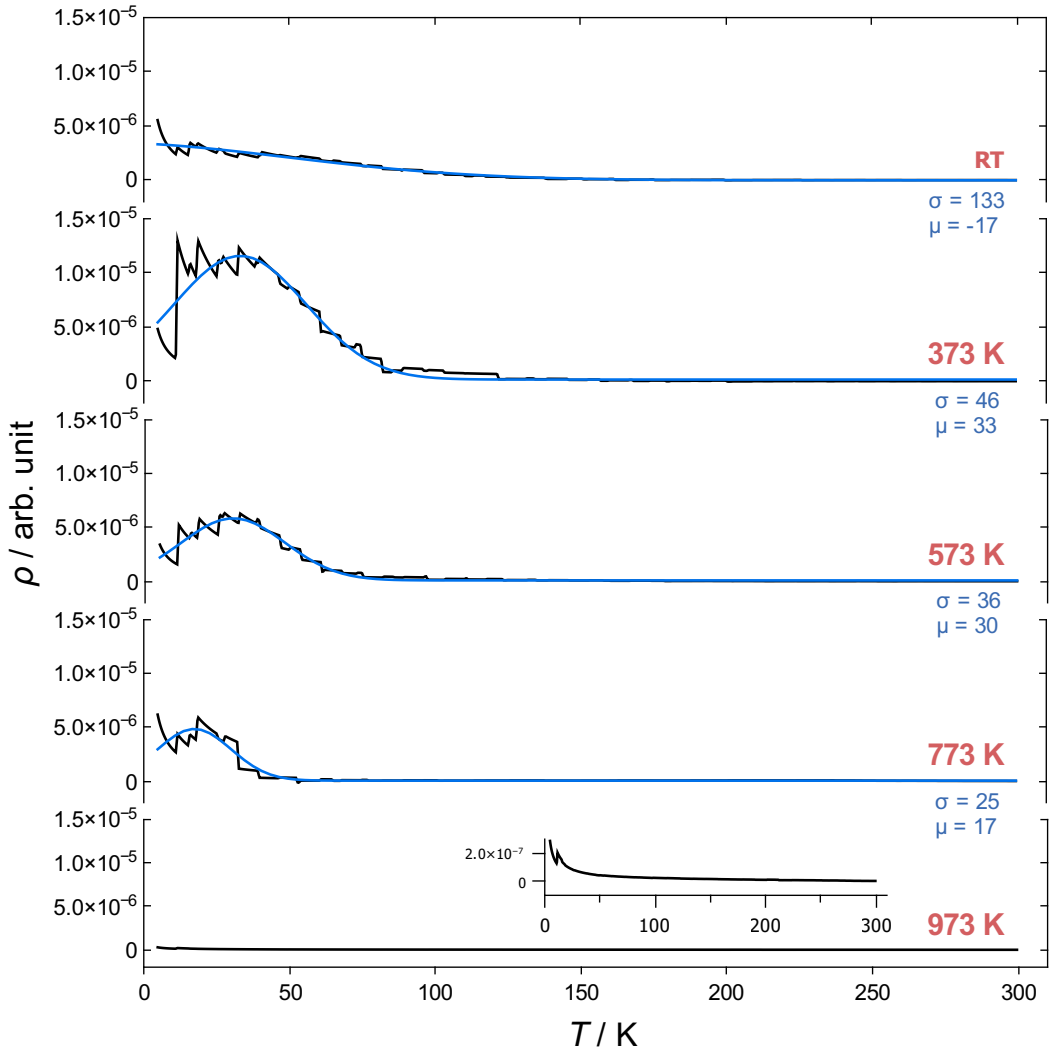

Figure 5.3: Magnetic anisotropy energy distribution with fitted Gaussian distribution (blue) for nanoporous palladium, thermal coarsened with different annealing temperatures. Inset: enlarged view of sample 973 K.

5.2 Magnetic Tuning Measurements

In this section, first several hypotheses, which could describe the alteration of magnetisation via surface charging, are discussed. Then the magnetic tuning measurements of np-Pd(Co) in $LiPF_6$/EC/EMC are analysed with respect to the applicability of the presented models. Afterwards, relevant parameters, which help to characterise the magnetic tuning and its efficiency, are discussed. Finally the same will be carried out for the measurements of np-Pd(Co) in KOH.

5.2.1 Potential Models for Magnetic Tuning

Rigid-Band Model

A simple model for explaining the tuning of the magnetisation by means of applied voltage is given by the rigid band displacement model[58] which was also discussed before by Drings et al.[1]. In ferromagnetic materials narrow bands are observed and the Fermi level E_F lies at or near the maximum of the density of states[13]. This condition can be written as the Stoner criterion[13]:

$$\mathcal{I}\mathcal{N}_{\uparrow,\downarrow}(E_\mathrm{F}) > 1\,. \tag{5.2}$$

Here, $\mathcal{N}_{\uparrow,\downarrow}(E_\mathrm{F}) = \mathcal{D}(E)/2n$ is the density of states per atom for each spin state (n is the number of atoms per unit volume) and $\mathcal{I}$ is the Stoner exchange parameter, which is about 1 eV for $3d$ ferromagnets[13]. If the Stoner criterion is satisfied the susceptibility diverges and spontaneous band splitting occurs which leads to ferromagnetism.

For palladium with a high value of $\mathcal{D}(E_\mathrm{F})$, the Stoner criterion is almost fulfilled[13]. One idea for a voltage induced change in magnetic properties is, that the electric field shifts the Fermi level just enough to satisfy the stoner criterion and forces a band splitting. So the adding (or removing) of electrons to the nearly filled d band[59], decreases (or increases) the density of states and therefore also the susceptibility. According to *ab initio* calculations for palladium, done by MacDonald et al., the Fermi level is just a bit higher than the density of states maximum[60]. Therefore the depletion of electrons on the surface would theoretically increase the susceptibility and thus the magnetisation[61,62]. This corresponds to a increase

in magnetisation upon positive charging $\frac{\Delta M}{\Delta Q} > 0$, as reported by Zhernenkov et al. for a thin $Co_{50}Pd_{50}$ film[3], by Drings et al. for nanocrystalline palladium[1] and by Ghosh for np-$Pd_{74}Ni_{26}$[4].

Magnetoelastic Effects

A magnetoelastic approach was considered by Ghosh et al.[2,4], Drings et al.[1] and also Mishra et al.[63]. In this approach the change in magnetisation is explained via the circumstance that the accumulation of electrons on the surface of a material changes not only its electronic structure but also the strain state on the surface[64,65]. Excess electrons on the surface results in elastic strain and stress, which is balanced by compensating strain and stress in the bulk, as reported for several nanoporous materials, such as Pt[66,67], Au[68,69], PdNi[4] and PdCo[2]. This leads to reversible structural changes, due to out- or inward relaxation of atomic layers near the surface[70], and alters the volume by means of elastic interaction between surface and bulk. Consequently, due to magnetoelastic coupling, an alteration of the magnetisation occur. In this model $\frac{\Delta M}{\Delta Q}$ can be positive or negative, dependent on the magnetoelastic coupling.

Modification of Magnetic Anisotropy Energy

Another potential explanation, discussed by Subkow and Fähnle[71], could be that a charging-induced change in magnetic surface energy, reorientates the macroscopic magnetic moment. In their *ab initio* study, nanoporous materials are approximated as several polyhedral particles linked by metallic grain boundaries to a contiguous chain with multiple branches. The nanoparticles and their surfaces, due to their polyhedral character, are oriented in different directions. Surface anisotropy tends to align the atomic magnetic moments close to the different surfaces in a certain direction. Due to the various different surfaces and surface orientations of the polyhedral particles, different surface anisotropies are present. These different surface anisotropies lead to a non-collinearity between the atomic magnetic moments and to a change in the orientation of the magnetic moment of the whole particle. Consequently the macroscopic magnetic moment and thus the magnetisation is modified. Subkow and Fähnle simulated, for the sake of simplicity, one nanoparticle of cubic shape with edge length 3.5 nm. They reported, that the non-collinearities of the atomic magnetic moments are too small to be responsible for the change of magnetisation upon charging. Also the

modification of the orientations of the magnetic moments of the particles was rather small. However, this changes if two parallel faces of the cube remain uncharged. This anisotropic charging is a suitable assumption for nanoporous materials since not all surfaces are in contact with the electrolyte and not all surfaces have the same size. This allows different charge modifications for different surfaces. With this adjustment, Subkow and Fähnle found a strong shift of the magnetic anisotropy energy upon charging and thus a modification of the magnetisation. So, an anisotropic charging of the free surfaces of a nanoporous material, can change its surface anisotropy and the orientation of the total magnetic moment.

5.2.2 Organic Lithium-based Electrolyte

The current-voltage curve of a non-ideal capacitor is not exactly rectangular (figure 2.3). So at the reversal point of the voltage, some time passes until charge, and thus magnetisation, reach their reversal points. This is a delay due to kinetics and is an expected phenomenon which is known for a charging behaviour which differs from the one of an ideal capacitor.

As can be seen in each measurement in the lithium-based electrolyte (figures 4.7 to 4.13), the magnetisation has a direct response to the variation of the charge and thus varies in phase (with a small delay) with voltage and charge at all fields and all coarsening degrees. The increase of the charge with increasing voltage originates from the positively charged working electrode which attracts negative charged ions. These ions repress the electrons on the surface of the sample and cause an electron depletion at the surface in the double layer regime. In opposite to other works of tuning measurements, e.g. nanocrystalline Pd[1], thin CoPd films[3] or $Pd_{74}Ni_{26}$[4], in the present work, for np-Pd(Co) in $LiPF_6$/EC/EMC, an increase of magnetisation with decreasing charge is observable. This means a lowering on magnetisation upon positive charging, $\frac{\Delta M}{\Delta Q} < 0$, which was previously observed for np-PdCo in $1\,\mathrm{mol\,L^{-1}} LiClO_4$ dissolved in ethyl acetate (EA) by Ghosh et. all[2] and for other nanoporous materials, just like $Pd_{35}Ni_{65}$[4] and AuFe[63]. This sign is not compatible with the rigid-band model. Also the observation that magnetisation lags behind the voltage, but not the charge, makes the direct approach of a charge-induced band filling in the rigid-band model unlikely, but rather indicates chemical or pseudocapacitive reactions as origin for the change of magnetic properties.

A hint for occurring chemical reactions is also the visible drift in all charge and magnetisa-

tion measurements (figures 4.7 to 4.13). It is seen that for the sample of 373 K annealing temperature (figure 4.8 and 4.11) the chemical drift is weaker and of opposite direction. Due to the drift, the initial value of magnetisation can not be recovered anymore. It is assumed, that the occurring chemical reactions have a reversible contribution, which represents the main part of these side reactions, and an irreversible contribution. The reversible reactions contribute to the pseudocapacitive behaviour of the sample and the weak irreversible reactions may cause the drift of magnetisation and charge, and may cause the degradation of the sample.

Magnetic Key Parameters

For a characterisation of magnetic tuning measurements several important parameters, such as the absolute and relative change in magnetisation, the magnetoelectric-voltage coefficient and the tunability have to be taken into consideration. These parameters are presented in table 5.1 and will be discussed, *inter alia*, later on.

Table 5.1: Absolute change in magnetisation, relative change in magnetisation after drift-correction, tunability and magnetoelectric-voltage coefficient of np-Pd(Co) in $LiPF_6$/EC/EMC in dependence of annealing temperature.
T_A.....Annealing temperature
ΔM.....Absolute change in magnetisation
$\frac{\Delta M}{M_0}$.....Relative change in magnetisation
$\frac{\Delta M}{\Delta Q}$.....Tunability (defined as the change in absolute magnetisation per charge)
$\alpha_{C,V}$.....Magnetoelectric-voltage coefficient, converted into units of magnetic field

T_A / K	ΔM / 10^{-3} emu g^{-1}	$\frac{\Delta M}{M_0}$ / %	$\frac{\Delta M}{\Delta Q}$ / 10^{-2} emu A^{-1} s^{-1} g^{-1}	$\alpha_{C,V}$ / Oe V^{-1}
RT	(3.6 ± 0.3)	0.144 ± 0.015	(-3.1 ± 0.4)	0.49 ± 0.05
373	(2.67 ± 0.06)	0.240 ± 0.006	(-4.5 ± 0.5)	0.360 ± 0.009
573	(3.28 ± 0.15)	0.64 ± 0.03	(-5.6 ± 1.5)	0.44 ± 0.03
773	(1.8 ± 0.3)	0.65 ± 0.07	(-6 ± 2)	0.24 ± 0.05

Figure 5.4 shows the variation of $\frac{\Delta M}{M_0}$ after drift correction by means of a baseline subtraction. With this correction, several minima were forced on the same level by applying linear interpolation between the minima and a subtraction of the interpolated data from the original values. This procedure was carried out in order to improve comparability and avoid contributions of chemical drift in the following quantitative analysis.

In all measurements a CV with the same scan rate and potential limits was carried out, thus the magnetisation peaks can be found at the same time intervals for all samples. It is clearly seen that the relative magnetisation change increases with increasing coarsening, although the current decreases. While, at the unannealed sample, an amplitude of about 0.14 % is reached, after annealing at 573 K the amplitude increased to about 0.64 %. An even higher annealing does not increase the relative change significantly anymore, seen on the sample annealed to 773 K.

However, the absolute value of magnetisation change ΔM, also seen in table 5.1, decreases with higher annealing temperature. For the thermally untreated sample, a change in magnetisation around $3.6 \cdot 10^{-3}$ emu g^{-1} was reached, while the sample, annealed to 773 K,

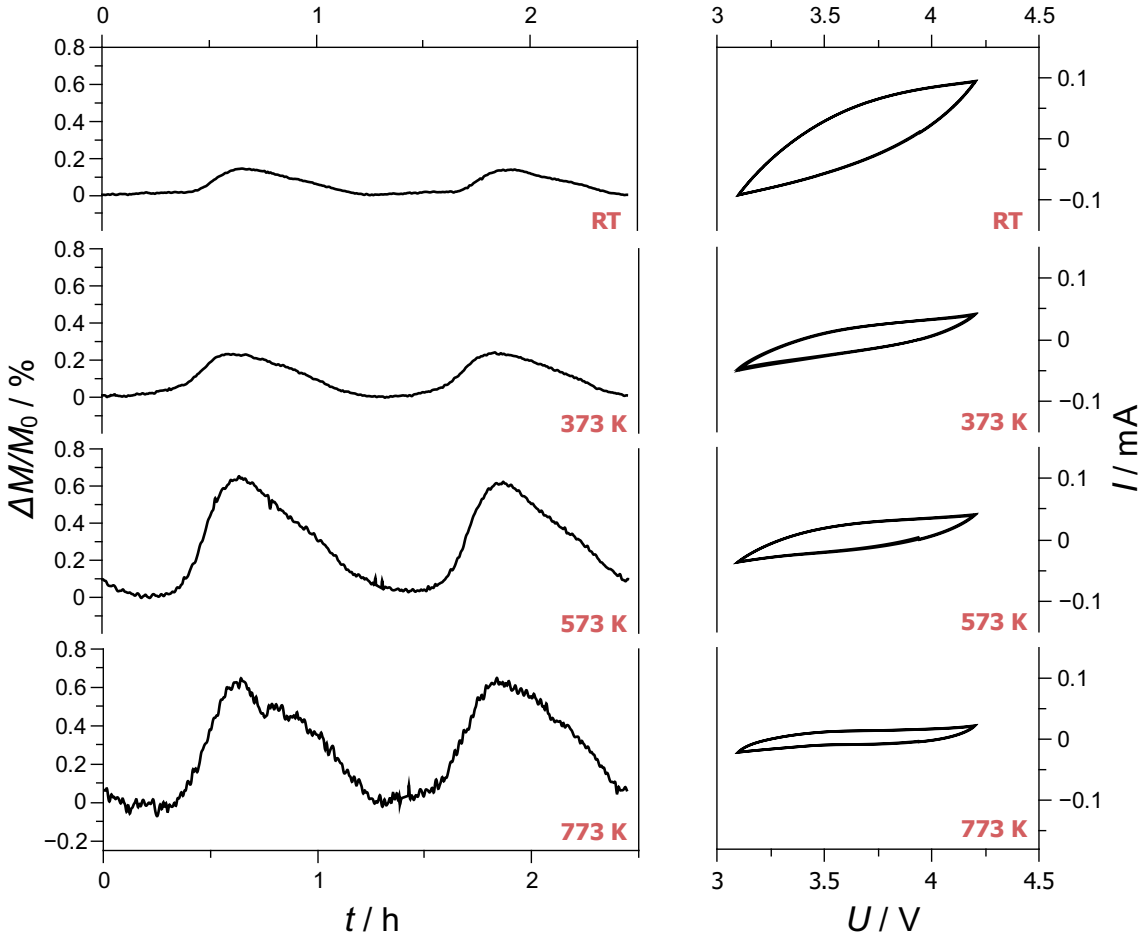

Figure 5.4: CVs with a scan rate of $0.5\,\mathrm{mV\,s^{-1}}$ and baseline-corrected data for the relative change in magnetisation of np-Pd(Co) in $LiPF_6$/EM/EMC for different thermal treatments upon surface charging and an applied magnetic field of 500 mT.

showed a magnetisation change of about $1.8 \cdot 10^{-3}\,\mathrm{emu\,g^{-1}}$. Also in *ex situ* magnetisation measurements, the saturation magnetisation decreased with higher coarsening degree as seen in figure 4.2. So, the magnetisation for coarsened sample is smaller, but has a (much) stronger response to the surface charging. This is a consequence of thermal treatment and may be explained via the cobalt atoms, which increasingly occur on the surface due to thermal dilution.

In a comparison to other works, where magnetisation-charge characteristics also follow a magnetisation increase upon negative charge ($\frac{\Delta M}{\Delta Q} < 0$), it is seen that these changes in magnetisation are quite small. For a surface charging (in the capacitive regime) on np-$Pd_{90}Co_{10}$ alloys at 100 mT [2] and np-$Pd_{35}Ni_{65}$ at 90 mT [4], both in $1\,\mathrm{mol\,L^{-1}}$ $LiClO_4$ dissolved in ethyl acetate, a change of about $15 \cdot 10^{-3}\,\mathrm{emu\,g^{-1}}$ was reported for both materials, corresponding

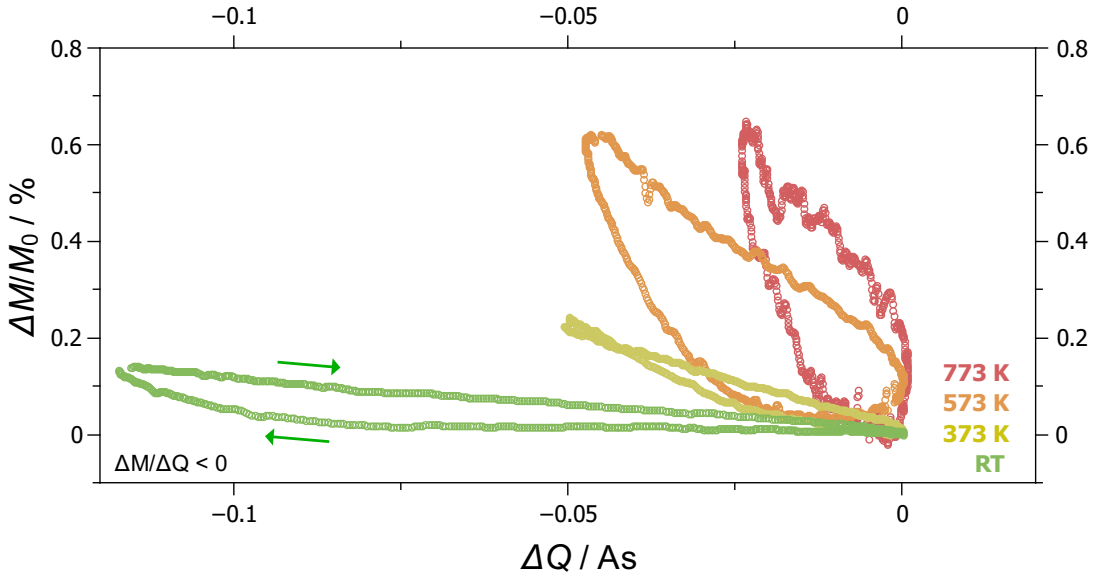

Figure 5.5: Relative change in magnetisation, for one cycle, in dependence of charge of np-Pd(Co) in $LiPF_6$/EC/EMC for different thermal treatments upon surface charging and an applied magnetic field of 500 mT.

to a relative change of about 3 % for both materials, was reported.

Figure 5.5 shows the baseline-corrected values of relative change in magnetisation over the corrected values of charge. It shows, how well magnetisation can be tuned, for a certain amount of charge and thus how efficient the modification of magnetisation upon surface charging for different thermally treated samples is.

Like it is seen before, a higher magnetisation change is reached with the more coarsened samples. All of the measurements form closed loops. These loops originate from the pseudocapacitive reactions while charging, which indicates that the processes involved in the switching mechanism are reversible but with a hysteresis. In all samples the magnetisation increases upon negative charging ($\frac{\Delta M}{\Delta Q} < 0$), which results in negative slopes of the loops. Although loops were not visible in the work of Ghosh et al., they observed the same sign of $\frac{\Delta M}{\Delta Q}$ for np-$Pd_{35}Ni_{65}$[4] and for np-PdCo alloys[2] in 1 mol L^{-1} $LiClO_4$ dissolved in ethyl acetate.

From the $\frac{\Delta M}{M_0}$-ΔQ-plot, the slope $\frac{\Delta M}{\Delta Q}$ was deduced as summarised in table 5.1. The steepness of these slopes (absolute change in magnetisation over charge), here denoted as the tunability, are a scale for the efficiency of the surface charging. The steeper the slope, the stronger the magnetisation is affected by the charging mechanism. In figure 5.5 a stronger steepness is

observable with higher annealing temperatures. In table 5.1, it is seen that the slope for the sample, annealed to 773 K is steeper than the one for 573 K, although the same change in magnetisation is reached. This means, that although the magnetisation change can only reach up to 0.65 % in both samples, the more coarsened sample needs a smaller amount of charge for the same result, but also reaches a smaller absolute change in magnetisation (also seen in table 5.1). Hence, the most coarsened sample delivers the smallest magnetisation (also after surface charging), but is the most efficient one when it comes to magnetisation change due to surface charging.

Another important coefficient to characterise the efficiency of the charging mechanism is the magnetoelectric-voltage coefficient $\alpha_{\mathrm{C,V}} = \frac{\Delta M}{\Delta V}$ [6], where ΔM denotes the absolute change in magnetisation and ΔV the applied potential range for charging (1.1 V). This coefficient is a scale for the magnitude of the magnetoelectric effect. The magnetoelectric-voltage coefficient for np-Pd(Co), annealed to different temperatures, is displayed in table 5.1. For comparability, ΔM was formally converted into units of magnetic field H ($\Delta H = 4\pi\Delta M$). It is seen that $\alpha_{\mathrm{C,V}}$ decreases with increasing annealing temperature. This is to be expected, since the absolute change in magnetisation shows the same behaviour and the voltage range is the same for all samples. These magnetoelectric-voltage coefficients are quite small in comparison to other experiments with solid-liquid interfaces [6]. For materials in electrolytes, in which magnetisation is changed by ion intercalation, particular large $\alpha_{\mathrm{C,V}}$ values are reported. Fe_3O_3 in $LiPF_6$/EC + DC [72] shows a $\alpha_{\mathrm{C,V}}$ of 58 Oe V^{-1}. $ZnFe_2O_4$ in $LiPF_6$/EC + DC [73] reached 370 Oe V^{-1} and $CuFe_2O_4$ in $LiPF_6$/EC + DC [73], 530 Oe V^{-1}. $\alpha-Fe_2O_3$ in $LiPF_6$/PC [74] reached even 4400 Oe V^{-1}. However, in comparison to a system where changes in magnetisation are caused via magnetoelastic effects, $\alpha_{\mathrm{C,V}}$ is about the same magnitude as in the measurements received in this work. $Pd_{90}Co_{10}$ in $LiClO_4$ dissolved in ethyl acetate from the work of Ghosh et al. [2] shows a magnetoelectric-voltage coefficient of 1 Oe V^{-1}. In conclusion the change in magnetisation, which can be reached in a certain voltage range due to magnetoelectric coupling, decreases with coarser samples and is a lot smaller than the magnetisation change obtained by intercalation [2,4,72–74]. This is quite plausible since intercalation affects the whole volume and not only the surface (in case of surface charging). This can also be seen in the measurements with KOH as a electrolyte, which is discussed later on.

Which Model Suits?

As chemical reactions, associated with the adsorption of ions, also alter the electronic structure, they could be responsible for the magnetisation change upon charging. However, since in our experiments, adsorption is limited by choosing moderate potential limits (3.1 to 4.2 V) and the use of a non-aqueous electrolyte ($LiPF_6$ in EC/EMC(1:1)), chemical reactions, as a cause for the reversible modification of the magnetisation, seem to be unlikely. Also in the measured CVs, displayed in figure 5.4, it is seen, that no adsorption peaks and a nearly rectangular shapes were observed. So, strong redox reactions can be excluded. This supports the consideration, that chemical reactions are not the right approach to describe the changes in magnetisation.

Also the rigid-band model can be excluded. Since the rigid-band model would manifest itself in an increase of magnetisation upon positive charging ($\frac{\Delta M}{\Delta Q} > 0$), whereas in this work the opposite was measured ($\frac{\Delta M}{\Delta Q} < 0$), it is reasonable to assume that this simplified model can not be used to explain the interaction between surface charging and magnetic properties of np-Pd(Co). In fact, a look at electronic structure calculations[13] (figure 5.6) reveals, that neither for pure Pd nor for $Pd_{98.5}Co_{1.5}$ the band model would lead to an increase in magnetisation upon negative charging (negative charging would add electrons to the surface and shift the Fermi energy to the right.) One might suspect a scenario for an increasing Co content where a filling of the band structure leads to an increase of the magnetisation. However, considering the band structures of various compositions[75,76] and for pure Co[13], one can tell that filling always equals the imbalance between the density of states of up-spin electrons and down-spin electrons and thus leads always to a reduction of magnetisation. Therefore, the rigid-band model predicts $\frac{\Delta M}{\Delta Q}$ to be always positive, regardless of the composition. This implies that the rigid-band model can not describe the magnetisation change due to surface charging for Co, Pd, or any possible alloy between them.

Having excluded chemical reactions and band filling, the magnetoelastic model and the modification of magnetic anisotropy energy are the most suitable models yet. The magnetoelectric-voltage coefficient for $Pd_{90}Co_{10}/LiClO_4$ in EA, which possesses magnetoelastic attributes[2], shows even the same magnitude as in this work for np-Pd(Co) in $LiPF_6$/EC/EMC.

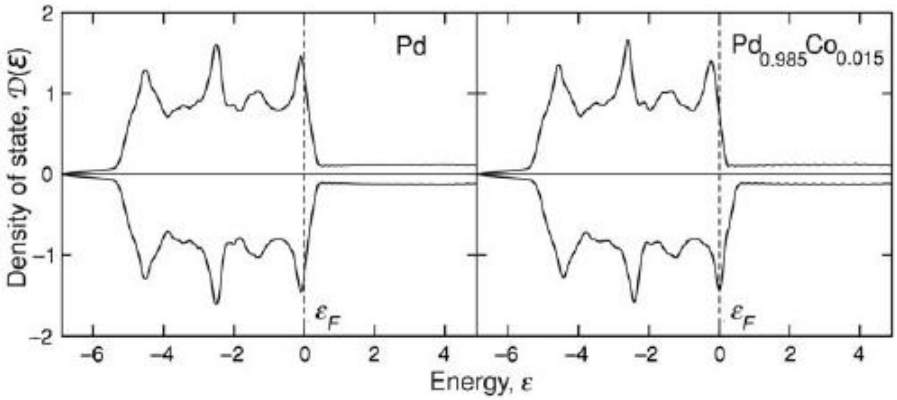

Figure 5.6: Electronic structure calculations: a dilute alloy PdCo; pure Pd is not magnetic, but doping with 1.5 at% Co introduces a giant moment of 18 μ_B per cobalt atom. Here, ε_F is the Fermi energy. (Data courtesy of Stefano Sanvito.)[13]

5.2.3 KOH as an Electrolyte

Voltage, charge and magnetisation measurements over time for different annealing temperatures in the voltage range of −0.4 to −0.5 V are displayed in figures 4.14 to 4.17. The measurements for −0.4 to −0.7 V can be seen in figures 4.18 to 4.21. Again, the magnetisation decreases upon electron depletion, seen in the increase of magnetisation with the decrease of charge. In comparison to the measurements in $LiPF_6$/EC/EMC no significant delay between the voltage and the reacting charge is visible. This applies also for the magnetisation. This suggests that, in relation to the organic electrolyte, the current in KOH has a steeper increase at the turning points of the CVs and thus the whole CV has a more rectangular shape. This can be seen in a comparison to the CVs of the 0.1 V-voltage range, in figure 5.7, with the CVs of the organic electrolyte, in figure 5.4.

In all charge and magnetisation measurements in KOH, in the potential range of −0.4 to −0.5 V, drifts are visible, which indicates again chemical and pseudocapacitive reactions. In comparison to the measurements in the lithium-based electrolyte the drifts differ strongly from each other and show no uniform direction nor a constant steepness.

In opposite, the measurements in the potential range of −0.4 to −0.7 V show almost no drifts. This is explainable due to the circumstance, that always a single sample was used for measurements in both potential windows. Because the measurements in the range of −0.4 to −0.7 V come last, any reactions had presumably come to a halt by the time the measurement

started and are not visible anymore. The magnetisation change in this potential range is much higher than for −0.4 to −0.5 V and the measurements in $LiPF_6$/EC/EMC. This higher magnetisation could be a consequence of hydrogen adsorption. Hydrogen adsorption occurs on Pd versus Ag/AgCl in KOH at about −0.6 V[43] which corresponds to a potential of about −0.5 V versus Au (reference electrode is a Au wire).

It should be noted that Gößler et al.[7] also studied magnetic tuning by charging in KOH, in a potential range known for hydrogen absorption. In contrast, the focus of the present thesis was on the magnetic tuning behaviour by charging in the pseudocapacitive regime and only partly on the hydrogen-adsorption regime in KOH. The consequences of different Co distributions, within the nanoporous structure, on the magnetic properties, as a result of thermal annealing, is of central interest in the current work. Additionally, Pd samples underwent a slight different fabrication method compared to the work of Gößler et al. Gößler et al. used a dealloying potential of 700 mV versus Ag/AgCl and dealloyed down to a residual current of 100 µA. In this thesis, the dealloying was performed with a dealloying potential of 550 mV versus Ag/AgCl, down to a residual current of 10 µA. The large changes upon hydrogenation in the reference paper up to 600 %, were a result of hydrogen incorporation in the Pd lattice, which was not investigated in this thesis. However, the mechanism of an RKKY-enhancement upon hydrogenation was adopted to account for tuning measurements in the hydrogen adsorption regime below.

For hydrogen intercalation in np-Pd(Co) in KOH, occurring at sufficiently low potentials[43], it is reported that the magnetisation increases with the amount of hydrogen stored[43]. It is explained via the hydrogen atoms which interacts with the cobalt atoms in the sample. The additional electrons, provided by the hydrogen, increase the number of conduction electrons and thus, since the RKKY interactions is transmitted via conduction electrons, the range of the RKKY interaction. Also for other materials a change in magnetisation upon intercalation is reported[72–74]. The increasing magnetisation upon a change in the range of the RKKY interaction due to additional electrons could be also applied to the adsorbed hydrogen atoms. The effect due to adsorption is expected to be weaker as the one due to absorption, since the hydrogen atoms can not penetrate the bulk and thus a higher distance between them and the internal Co atoms is the consequence. Since a nanoporous material has a high surface area, high amount of hydrogen can be adsorbed, which would explain the noticeable higher

magnetisation in the potential range of -0.4 to $-0.7\,\mathrm{V}$. This increase in magnetisation, in particular, is attributed to chemical reactions (hydrogen adsorption) and thus can not be assigned to pseudocapacitive effects.

Magnetic Key Parameters

The absolute and relative change in magnetisation, the magnetoelectric-voltage coefficient and the tunability, for both potential ranges, are displayed in table 5.2.

Table 5.2: Absolute change in magnetisation, relative change in magnetisation, tunability and magnetoelectric-voltage coefficient of np-Pd(Co) in KOH in dependence of annealing temperature at different potential ranges.
T_A.....Annealing temperature
ΔM.....Absolute change in magnetisation
$\frac{\Delta M}{M_0}$.....Relative change in magnetisation
$\frac{\Delta M}{\Delta Q}$.....Tunability (defined as the absolute change in magnetisation per charge)
$\alpha_\mathrm{C,V}$.....Magnetoelectric-voltage coefficient, converted into units of magnetic field

Potential Range: -0.4 to $-0.5\,\mathrm{V}$

T_A / K	ΔM / 10^{-3} emu g^{-1}	$\frac{\Delta M}{M_0}$ / %	$\frac{\Delta M}{\Delta Q}$ / 10^{-2} emu A^{-1} s^{-1} g^{-1}	$\alpha_\mathrm{C,V}$ / Oe V^{-1}
RT	(4.1 ± 0.4)	0.63 ± 0.05	(-6 ± 2)	6.1 ± 0.6
373	(4.21 ± 0.14)	0.64 ± 0.02	(-4.5 ± 0.9)	6.2 ± 0.3
573	(2.9 ± 0.3)	0.47 ± 0.04	(-4.9 ± 0.7)	4.3 ± 0.5
773	(3.07 ± 0.09)	0.444 ± 0.012	(-20 ± 8)	4.60 ± 0.14

Potential Range: -0.4 to $-0.7\,\mathrm{V}$

T_A / K	ΔM / 10^{-3} emu g^{-1}	$\frac{\Delta M}{M_0}$ / %	$\frac{\Delta M}{\Delta Q}$ / 10^{-2} emu A^{-1} s^{-1} g^{-1}	$\alpha_\mathrm{C,V}$ / Oe V^{-1}
RT	(13.98 ± 0.09)	2.81 ± 0.04	(-4.2 ± 1.4)	6.91 ± 0.05
373	(26.9 ± 0.6)	3.96 ± 0.08	(-7.6 ± 0.9)	13.3 ± 0.3
573	(17.5 ± 0.3)	2.83 ± 0.04	(-5.3 ± 1.9)	8.65 ± 0.15
773	(31.5 ± 0.6)	4.61 ± 0.08	(-19 ± 5)	15.6 ± 0.3

The drift-corrected magnetisation at a field of 500 mT and the corresponding CVs are plotted, for the pseudocapacitive potential range (-0.4 to $-0.5\,\mathrm{V}$), in figure 5.7. Note that the measurement in the pseudocapacitive range had a smaller scan rate ($0.1\,\mathrm{mV\,s^{-1}}$). For both measurements five out of ten cycles were plotted (cycles 5 to 9) and the starting time of the fifth cycle was set to zero.

Since for each measurement in a certain electrolyte the same scan rate was used, maxima and minima of the magnetisation occur at the same time intervals. The measurements in the pseudocapacitive potential range show no clear variation with the annealing temperature

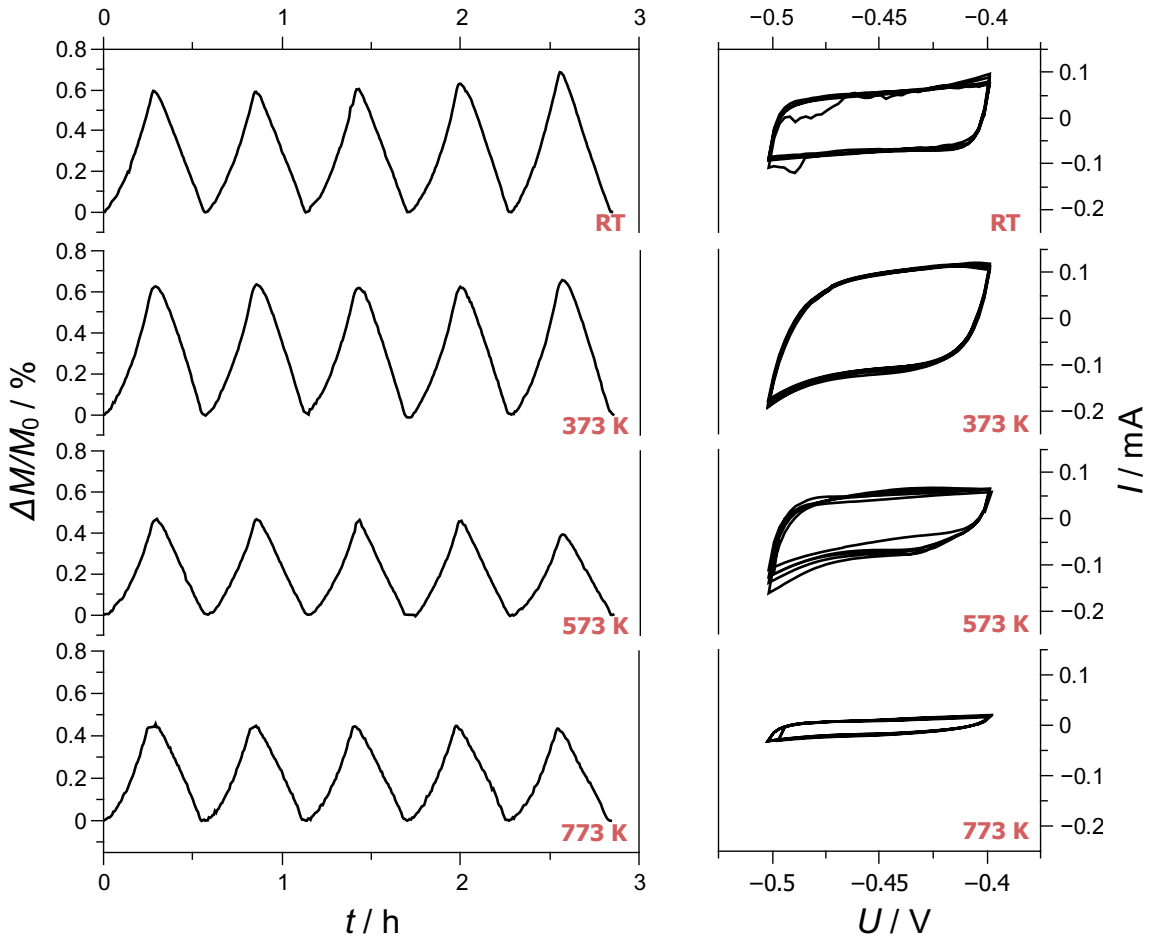

Figure 5.7: CVs with a scan rate of 0.1 mV s^{-1} and baseline-corrected data for the relative change in magnetisation of np-Pd(Co) in KOH for the potential range of −0.4 to −0.5 V and different thermal treatments upon surface charging and an applied magnetic field of 500 mT.

like in $LiPF_6$/EC/EMC. The relative change in magnetisation shows the highest value for the as-dealloyed sample and for the sample annealed to 373 K (0.63 % and 0.64 %). The other two show a slight lower value, 0.47 % for 573 K annealing temperature and about 0.44 % for 773 K. The corresponding currents, seen in the CVs of figure 5.7, seem to be also not strongly influenced by the annealing temperature. Here, the sample annealed to 773 K shows the lowest currents, which was also observed for the previous measurements in $LiPF_6$/EC/EMC. However, the sample annealed to 373 K has the highest currents and the other two samples (no temperature treatment and 573 K annealing temperature) show about the same currents. If we compare the correlation between current and magnetisation of the measurements, it stands out, that the two measurements which show almost the same currents (RT and 573 K) exhibit different relative changes in magnetisation. Additionally the

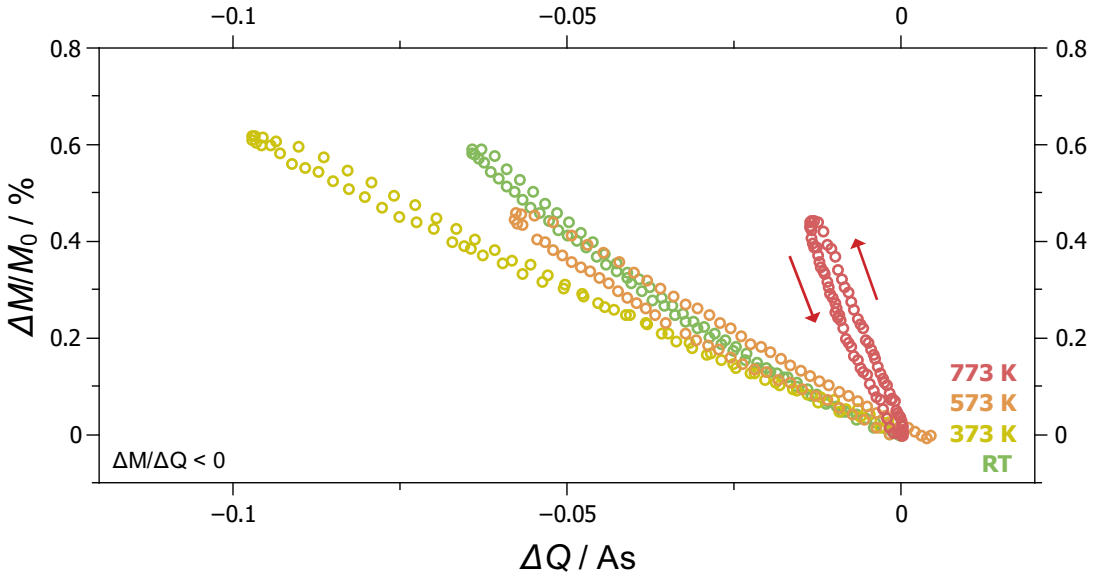

Figure 5.8: Relative change in magnetisation, for one cycle, in dependence of charge of np-Pd(Co) for different thermal treatments upon surface charging in the potential range of −0.4 to −0.5 V and an applied magnetic field of 500 mT.

samples with nearly the same change in magnetisation (RT and 373 K or 573 K and 773 K) show strongly different currents. So, no definite conclusion can be drawn regarding the way, the higher coarsening degree influences the current or the magnetisation. At the turning point at −0.5 V in the CVs, small tips are visible, which marks the beginning of hydrogen adsorption. In more negative potential values, these tips would transform to high peaks due to the hydrogen intercalation[43].

The baseline-corrected values of relative change in magnetisation over charge, for the pseudocapacitive range, are shown in figure 5.8. For every temperature treatment, one cycle is presented. It can be seen, that the magnetisation, as shown before in figure 5.7, does not increase with higher coarsening degree. However, the highest annealed sample (773 K) exhibits again the strongest influence to charging, indicated by the steepest slope, which is a measure for the tunability. The values for tunability are listed in table 5.2. The tunabilities of the as-dealloyed, 373 K-annealed and 573 K-annealed sample lie close together and one could not tell clearly, how the coarsening affected the tunability between these coarsening degrees. Like in the measurement in $LiPF_6$/EC/EMC (figure 5.5), also in this measurement tight loops are seen. These are discussed later on together with the measurement in the hydrogen-adsorption range.

The drift-corrected relative magnetisation change at 500 mT in the hydrogen-adsorption

range is displayed, together with the corresponding CVs, in figure 5.9. The CVs show again little tips at the left turning points (−0.7 V), which indicates hydrogen adsorption. These tips are small compared to the y-axis scaling. In this potential range, the currents seem also not to be strongly influenced by the coarsening degree. This applies also for the relative change in magnetisation, since no trend (increasing or decreasing magnetisation) with higher coarsening is observable. The sample annealed to 773 K has magnetisation change of 4.61 %, which is the highest observed, in this work and about the same magnitude as the achieved change by Ghosh et al. for np-$Pd_{90}Co_{10}$ alloys at 100 mT[2] and np-$Pd_{35}Ni_{65}$ at 90 mT[4] (both around 3 %). The lowest change in this potential range is shared with the as-dealloyed sample with 2.81 % and the one annealed to 573 K with 2.83 %. So no increase of relative magnetisation change with annealing temperature, like in $LiPF_6$/EC/EMC, is observable. As the data clearly show, in table 5.1 and 5.2, that the surface charging in KOH and this potential range (−0.4 to −0.7 V) leads to the highest relative changes in magnetisation.

Also the absolute change in magnetisation is the highest for the surface charging between −0.4 to −0.7 V in KOH. The sample annealed to 773 K shows the highest absolute change in magnetisation observed in this work (about $32 \cdot 10^{-3}$ emu g^{-1}). It is about 10 × as high as the magnetisation changes in the pseudocapacitive range, which lie around $3 \cdot 10^{-3}$ to $4 \cdot 10^{-3}$ emu g^{-1}. If we compare the absolute magnetisation change of both pseudocapacitive charging methods with the charging in hydrogen-adsorption range (table 5.1 and 5.2), it can be seen, that in the hydrogen-adsorption range even the charging at the as-dealloyed sample, which has the lowest change in magnetisation, gives a higher change than all of the chargings in the pseudocapacitive regimes. This holds even for the untreated sample where magnetic tuning is expected to be weaker as a result of the larger distance of the adsorbed hydrogen atoms to the internal Co clusters. Chemical reactions tend to have a stronger influence on the magnetic properties in an electrolyte than pure magnetoelastic effects would have[6]. In comparison to other works mentioned above, the magnetisation change is not remarkably higher. Capacitive surface charging on np-$Pd_{90}Co_{10}$ alloys at 100 mT[2] and np-$Pd_{35}Ni_{65}$ at 90 mT[4], both in 1 mol L^{-1} $LiClO_4$ dissolved in ethyl acetate reported a change around $15 \cdot 10^{-3}$ emu g^{-1}.

The baseline-corrected relative magnetisation change plotted over charge, for the hydrogen adsorption range, is seen in figure 5.10. The tunabilities of the as-received sample and the

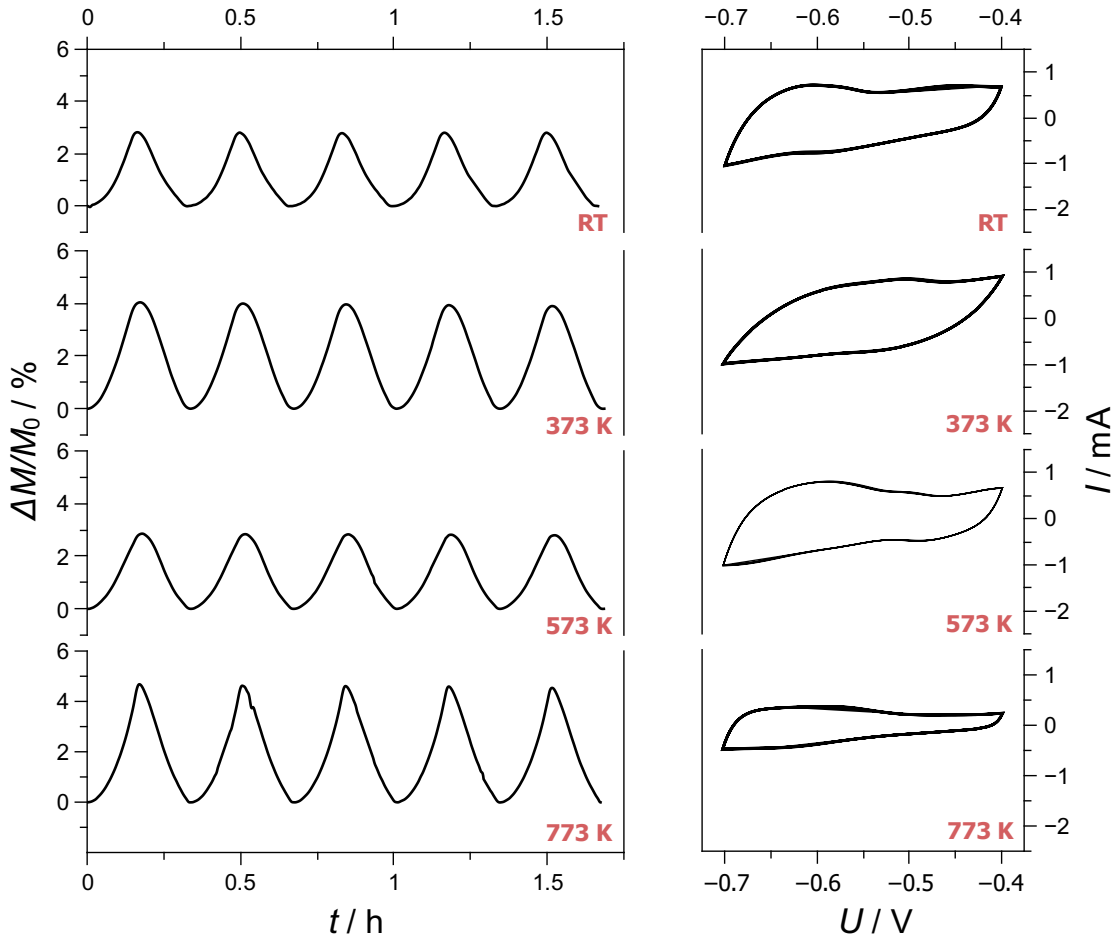

Figure 5.9: CVs with a scan rate of $0.5\,\mathrm{mV\,s^{-1}}$ and baseline-corrected data for the relative change in magnetisation of np-Pd(Co) in KOH for the potential range of -0.4 to $-0.7\,\mathrm{V}$ and different thermal treatments upon surface charging and an applied magnetic field of 500 mT.

samples annealed to 373 K and 573 K lie close together and it is not clearly understandable how the thermal treatment affected the tunability between those coarsening degrees. This behaviour is also known from the measurements in the pseudocapacitive range (figure 5.8). The tunability of the as-dealloyed sample and the ones annealed to 373 K and 573 K are about the same magnitude, while that of the 773 K-annealed sample exceeds strongly. So it is assumed that at this coarsening degree (annealed to 773 K) the Co content on the surface is much higher in relation to the other thermal treatments, which gives a stronger response to the surface charging.

In hydrogen adsorption range (figure 5.10) as in the pseudocapacitive range (figure 5.8), tight loops can be observed. These loops are visibly closer packed than the ones from the measurement in $LiPF_6$/EC/EMC (figure 5.5). This could indicate more reversible reactions

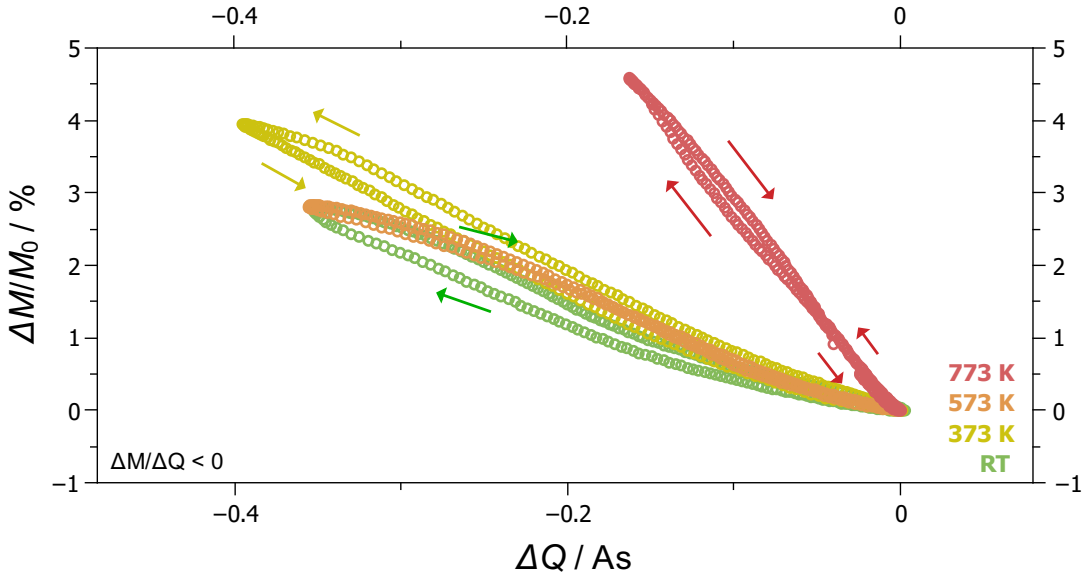

Figure 5.10: Relative change in magnetisation, for one cycle, in dependence of charge of np-Pd(Co) for different thermal treatments upon surface charging in the potential range of −0.4 to −0.7 V and an applied magnetic field of 500 mT.

as in $LiPF_6$/EC/EMC (since a perfect reversible reaction would manifest as a single slope). In the pseudocapacitive range, the magnetisation changes with the charge counter-clockwise (indicated by the arrow), while in the hydrogen-adsorption range (5.10) it is not always the case. The sample, annealed to 373 K shows the same rotation, but all other magnetisation changes rotate clockwise. It can be observed, that with lower charges the loops of the 573 K- and the 773 K-annealed samples show a cross-point after which the direction inverses and thus, the loops have, in this charge range, the same counter-clockwise orientation as the measurements in the pseudocapacitive regime (figure 5.8). The intercept represents the transition from the pseudocapacitive charging mechanism to the hydrogen-absorption effect at a charge of about −0.15 A s for the 573 K-annealed sample and −0.05 A s for the 773 K-annealed sample. An exception for this loop-orientation inversion is the as-dealloyed sample. It can be observed that this measurement never has an intersection and forms a closed loop instead of a cross-over. This could be a consequence of the circumstance, that this sample was tested before for hydrogen intercalation (which is not a part of this work) and thus the initial state of the sample could have been slightly changed.

The magnetoelectric-voltage coefficients for the different samples and potential ranges are shown in table 5.2. Both measurements in KOH give significantly higher values compared to $LiPF_6$/EC/EMC. The magnetoelectric-voltage coefficient for the measurements between

$-0.4\,\mathrm{V}$ and $-0.5\,\mathrm{V}$ seems to decrease with higher annealing temperature (as the absolute change in magnetisation does). The highest values of $\alpha_{\mathrm{C,V}}$, in this work, is obtained by the charging in KOH in the hydrogen-adsorption range. Yet, magnetisation changes and thus magnetoelectric-voltage coefficients due to intercalation are much higher [6]. In opposite to the pseudocapacitive regime, in the hydrogen-adsorption regime, $\alpha_{\mathrm{C,V}}$ shows no decreasing trend with annealing temperature. Nevertheless the highest value of $\alpha_{\mathrm{C,V}}$, $15.6\,\mathrm{Oe\,V^{-1}}$, is obtained by the most coarsened sample (annealed to 773 K). This can be explained via the increasing Co content on the surface with higher annealing temperature. The surface of the coarser sample is smaller, and thus fewer hydrogen atoms can adsorb, but more cobalt atoms are located on the surface. Thus hydrogen can reach more cobalt, which increases the range of the RKKY interaction.

Which Model Suits?

Again, the decrease of magnetisation upon electron depletion can be observed, which implies that the rigid-band model can not be responsible for the occurring change in magnetisation, for the same reasons outlined already in section 5.2.2. Chemical or pseudocapacitive reactions seems also to be unlikely in the pseudocapacitive range, since the corresponding CVs (figure 5.7) exhibit almost constant currents, typical for capacitive behaviour. Again, the magnetoelastic approach or the modification of anisotropy energy are the most likely models. However for the hydrogen-adsorption range, the shape of a CV varies from the rectangular shape, giving higher currents at the lower potential limit, and much stronger changes in magnetisation were observed. This indicates, that in this potential range indeed chemical reactions (hydrogen adsorption) are responsible for the underlying change in magnetisation. Since in different potential ranges, different effects explain the occurring change in magnetisation, it is assumed that in each case several effects are present, which compete with each other.

In the hydrogen regime the sample shows a clear hierarchy when it comes to the magnitude of the parameters (absolute and relative change in magnetisation, tunability and magnetoelectric-voltage coefficient). The sample annealed to 773 K shows for every parameter the highest values. The 373 K-annealed sample has the second highest values in every field, the 573 K-annealed sample the third highest and the sample, which had no thermal

Table 5.3: Amplitude of charge of np-Pd(Co) in $LiPF_6$/EC/EMC (3.1 to 4.2 V) and np-Pd(Co) in KOH (−0.4 to −0.5 V), in dependence of annealing temperature.
T_A.....Annealing temperature
ΔQ_{Li}.....Amplitude of charge in lithium-based electrolyte
ΔQ_{KOH}...Amplitude of charge in KOH
ΔM_{Li}.....Absolute change in magnetisation in lithium-based electrolyte, table 5.1
ΔM_{KOH}...Absolute change in magnetisation in KOH, table 5.2

T_A / K	ΔQ_{Li} / A s	ΔQ_{KOH} / A s	ΔM_{Li} / 10^{-3} emu g^{-1}	ΔM_{KOH} / 10^{-3} emu g^{-1}
RT	0.117 ± 0.003	0.063 ± 0.003	(3.6 ± 0.3)	(4.1 ± 0.4)
373	0.0509 ± 0.0011	0.101 ± 0.003	(2.67 ± 0.06)	(4.21 ± 0.14)
573	0.0472 ± 0.0002	0.063 ± 0.007	(3.28 ± 0.15)	(2.9 ± 0.3)
773	0.0241 ± 0.0008	0.0138 ± 0.0012	(1.8 ± 0.3)	(3.07 ± 0.09)

treatment, the lowest. This suggests, that in this potential range (in KOH), one of the competing effects is clearly dominant and is the major contribution to the change in magnetic properties. The dominant effect in KOH in this potential range (−0.4 to −0.7 V) is determined to the hydrogen adsorption.

In the pseudocapacitive regime (−0.4 to −0.5 V) of KOH chemical reactions are too weak, due to the moderate potential limits, to explain the difference in magnetic properties. It is assumed that in this regime magnetoelastic effects or the modification of the magnetic anisotropy energy play the major role in analogy to the $LiPF_6$/EC/EMC system. If we compare the amplitude of charge and the absolute change in magnetisation of the measurements in the lithium-based electrolyte with the ones in KOH, displayed in table 5.3, we see, that the change in magnetisation and the change of the charge are about the same magnitude.

Since the voltage range in KOH (−0.4 to −0.5 V) was much smaller than in $LiPF_6$/EC/EMC (3.1 to 4.2 V) and the change in charge is about the same, according to equation 4.1, the capacitance has to be higher for KOH. An estimation of the double layer capacitance in $LiPF_6$/EC/EMC and in KOH, using equation 4.1, reveals, that the difference in the capacitances becomes smaller with higher annealing temperatures, as displayed in table 5.4. The calculated double layer capacitances were divided by the masses of the samples, to provide a better comparability, and are referred as the mass specific double layer capacitance. Normally the capacitance would be scaled to the area, but since the surface area is not known of the samples inside the cells, their masses were used for scaling.

It can be seen, that the ratio of the capacitances in KOH and $LiPF_6$/EC/EMC, for the same

Table 5.4: Estimation of the mass specific double layer capacitances of thermal treated np-Pd(Co) in $LiPF_6$/EC/EMC and thermal treated np-Pd(Co) in KOH and the ratio between them. (Note: No errors are given, because these calculations are only rough estimations, in contrast to the surface area determination in H_2SO_4 shown in table 4.2.)
T_A.....Annealing temperature
$C_{DL,\ Li}$.....Mass specific double layer capacitance in $LiPF_6$/EC/EMC
$I_{DL,\ Li}$.....Double layer current in $LiPF_6$/EC/EMC
$C_{DL,\ KOH}$...Mass specific double layer capacitance in KOH
$I_{DL,\ KOH}$....Double layer current in KOH
$\frac{C_{DL,\ KOH}}{C_{DL,\ Li}}$.....Ratio of the mass specific double layer capacitances

T_A / K	$C_{DL,\ Li}$ / F g^{-1}	$I_{DL,\ Li}$ / A	$C_{DL,\ KOH}$ / F g^{-1}	$I_{DL,\ KOH}$ / A	$\frac{C_{DL,\ KOH}}{C_{DL,\ Li}}$
RT	~ 7	~ 0.06	~ 55	~ 0.06	~ 8
373	~ 4	~ 0.02	~ 96	~ 0.10	~ 24
573	~ 6	~ 0.03	~ 58	~ 0.06	~ 10
773	~ 3	~ 0.02	~ 11	~ 0.01	~ 4

degree of coarsening, becomes smaller with higher annealing temperatures. An exception forms the as-dealloyed sample. The specific double layer capacitance in KOH is always larger than in the organic electrolyte. This difference in specific double layer capacitance is a consequence of the different ion sizes. The size of the ions influences the double layer capacitance in two ways. Firstly, the area of the double layer becomes larger, because the ions have a bigger radius. If the double layer is seen as a parallel-plate capacitor, a larger width d of the capacitor leads to a smaller capacitance, since the capacitance is inverse proportional to the width of the capacitor. Secondly, smaller ions can be more closed packed and thus more charge on a given area is possible[77]. This optimises the packing of charge carriers which provides again a larger double layer capacitance. The ions in $LiPF_6$/EC/EMC are PF_6^- which have a diameter of 5.10 Å[78], while the ions in KOH are OH^- which have a diameter of 1.10 Å[79]. This explains the higher capacity occurring in KOH. For nanoporous materials, the size of the ions is an important property because ions have to diffuse in the nanoporous material. Especially when the size of the ions is in the range of the structures size, which applies to PF_6^- and the as-dealloyed sample (ligament size of about 4 nm, seen in table 4.2), slow diffusion would be expected, which would be suboptimal for reactions and double layer capacity. To conclude, chemical reactions in aqueous electrolytes limit the accessible voltage window, which limits the applicable charge. On the other hand, aqueous electrolytes provide smaller ions, which lead to a large double layer capacitance, which compensates this

limitation. This explains the same charge amplitude (and the following similar absolute change in magnetisation, both seen in table 5.3) of np-Pd(Co) in $LiPF_6$/EC/EMC and np-Pd(Co) in KOH, in spite of the smaller voltage window in KOH. This explanation would be justifiable for the magnetoelastic approach and the modification of the magnetic anisotropy energy. It can also be seen, that the capacitance in KOH is about $24\times$ as high as the one in $LiPF_6$/EC/EMC for the 373 K-annealed samples and for 773 K annealing temperature, the capacitance in KOH is only about $4\times$ as high. This different in ratio may be a consequence of a larger pseudocapacitive contribution to the specific double layer capacitance for different degrees of coarsening.

So, in conclusion more than one effect influences the magnetisation. In pseudocapacitive regimes the changes in magnetic properties is dominated by either the magnetoelastic effects or the modification of the magnetic anisotropy energy. In suitable potential ranges hydrogen-adsorption prevails, which has a much stronger effect on the magnetisation and overshadows other effects. The changes due to adsorption are significantly higher, than the changes due to magnetoelastic effects or the modification of magnetic anisotropy energy, but still not as high as magnetisation changes induced by intercalation. If a magnetoelastic effect, a change in the magnetic anisotropy energy or an interplay of both is the basic process for the change in magnetisation, could not be determined with our measurements.

Chapter 6

Conclusion

Nanoporous Pd samples were produced by dealloying $Co_{75}Pd_{25}$ in $0.1\,\mathrm{mol\,L^{-1}}$ H_2SO_4. After dealloying, five different thermal treatments were chosen to investigate the effect of annealing on the nanoporous samples. The core of this thesis was to study changing magnetic properties upon an applied voltage (in the pseudocapacitive potential range) in an electrolyte. To realise this, two different electrolytes and the corresponding pseudocapacitive voltage regimes were chosen. Additionally, a voltage range which is known for hydrogen adsorption was investigated in KOH.

Magnetic *ex situ* measurements revealed that residual Co concentration and its distribution were the decisive factors for the magnetic behaviour, rather than the size of the ligaments. As the sample was annealed, residual Co was redistributed over the nanoporous structure which resulted in a magnetic two-phase system. A Co-rich phase in which Co clusters behave like superparamagnets and a dilute-Co phase in which frustrated states couple over large regions. The magnetic behaviour was viewed as a result of the superposition of these two phases. From the blocking temperature of the Co-rich phase, the size distribution and the distribution of the anisotropy energy of the Co clusters could be derivated. It was found out that with higher annealing temperature the maximum of the distribution of the anisotropy energy and of the Co cluster size shifted to smaller cluster sizes.

In situ measurements showed that the magnetisation change upon surface charging was always positive with negative charge, which corresponds to a increase of magnetisation due to electron accumulation ($\frac{\Delta M}{\Delta Q} < 0$). This suggested that the rigid-band displacement model

can not describe observed processes, rather than magnetoelastic effects or a modification of the magnetic anisotropy energy seem to be more likely. The charging in $LiPF_6$/EC/EMC revealed that coarser samples showed a higher relative magnetisation change, although the absolute change in magnetisation decreased. The higher relative change in magnetisation was attributed to the Co atoms which are found increasingly on the surface due to annealing and provide a stronger response to the charge. Charging in the pseudocapacitive potential range of KOH gave a higher absolute change in magnetisation than a charging in $LiPF_6$/EM/EMC, but showed no clear dependence on the annealing temperature. The highest change in magnetisation (absolute and relative) was provided by a charging in the hydrogen-adsorption range of KOH. This was interpreted as a consequence of the hydrogen adsorption, which was found to yield stronger influences on the magnetisation than pseudocapacitive effects. As well, in this potential range, superficial Co gave a higher sensitivity to charging. The overall higher magnetisation change in KOH was associated with the higher specific double layer capacitance of KOH compared to $LiPF_6$/EC/EMC. A charging in the pseudocapacitive range yielded overall smaller changes in magnetisation as hydrogen adsorption or as intercalation.

Bibliography

[1] H. Drings, R. N. Viswanath, D. Kramer, C. Lemier, J. Weissmüller and R. Würschum. Tuneable magnetic susceptibility of nanocrystalline palladium. *Applied Physics Letters*, **88** (2006) 253103.

[2] S. Ghosh, C. Lemier and J. Weissmuller. Charge-dependent magnetization in nanoporous Pd−Co alloys. *IEEE Transactions on Magnetics*, **42** (2006) 3617.

[3] M. Zhernenkov, M. Fitzsimmons, J. Chlistunoff, J. Majewski, I. Tudosa and E. Fullerton. Electric-field modification of magnetism in a thin CoPd film. *Physical Review B*, **82** (2010) 024420.

[4] S. Ghosh. Charge-response of magnetization in nanoporous Pd−Ni alloys. *Journal of Magnetism and Magnetic Materials*, **323** (2011) 552.

[5] C. Navarro-Senent, A. Quintana, E. Menéndez, E. Pellicer and J. Sort. Electrolyte-gated magnetoelectric actuation: Phenomenology, materials, mechanisms, and prospective applications. *APL Materials*, **7** (2019) 030701.

[6] A. Molinari, H. Hahn and R. Kruk. Voltage-control of magnetism in all-solid-state and solid/liquid magnetoelectric composites. *Advanced Materials*, **31** (2019) 1806662.

[7] M. Gößler, M. Albu, G. Klinser, E.-M. Steyskal, H. Krenn and R. Würschum. Magneto-ionic switching of superparamagnetism. *Small*, **15** (2019) 1904523.

[8] M. Hakamada and M. Mabuchi. Fabrication of nanoporous palladium by dealloying and its thermal coarsening. *Journal of Alloys and Compounds*, **479** (2009) 326.

[9] C. Hamann and W. Vielstich. Elektrochemie, 3. Auflage (1998).

[10] A. A. Isse and A. Gennaro. Absolute potential of the standard hydrogen electrode and the problem of interconversion of potentials in different solvents. *The Journal of Physical Chemistry B*, **114** (2010) 7894.

[11] R. G. Compton and C. E. Banks. *Understanding Voltammetry*. World Scientific (2011).

[12] T. Krekeler, A. V. Straßer, M. Graf, K. Wang, C. Hartig, M. Ritter and J. Weissmüller. Silver-rich clusters in nanoporous gold. *Materials Research Letters*, **5** (2017) 314.

[13] J. M. Coey. *Magnetism and Magnetic Materials*. Cambridge university press (2010).

[14] J. Friedel. Metallic alloys. *Il Nuovo Cimento*, **7** (1958) 287.

[15] M. A. Ruderman and C. Kittel. Indirect exchange coupling of nuclear magnetic moments by conduction electrons. *Physical Review*, **96** (1954) 99.

[16] T. Kasuya. A theory of metallic ferro-and antiferromagnetism on Zener's model. *Progress of Theoretical Physics*, **16** (1956) 45.

[17] K. Yosida. Magnetic properties of Cu−Mn alloys. *Physical Review*, **106** (1957) 893.

[18] J. Stöhr and H. C. Siegmann. *Magnetism*. Springer (2006).

[19] Y. Takahashi. Interlayer exchange coupling mediated by a nonmagnetic spacer layer with a large electron-electron exchange interaction. *Physical Review B*, **56** (1997) 8175.

[20] F. W. Constant. The magnetic properties of certain Pt−Co and Pd−Co alloys. *Physical Review*, **36** (1930) 1654.

[21] D. Gerstenberg. Magnetische Untersuchungen an Pd-Mischkristallen mit Übergangselementen. *Annalen der Physik*, **457** (1958) 236.

[22] R. Bozorth, P. Wolff, D. Davis, V. Compton and J. Wernick. Ferromagnetism in dilute solutions of cobalt in palladium. *Physical Review*, **122** (1961) 1157.

[23] W. Eerenstein, N. Mathur and J. F. Scott. Multiferroic and magnetoelectric materials. *Nature*, **442** (2006) 759.

[24] Y.-H. Chu, L. W. Martin, M. B. Holcomb, M. Gajek, S.-J. Han, Q. He, N. Balke, C.-H. Yang, D. Lee, W. Hu et al. Electric-field control of local ferromagnetism using a magnetoelectric multiferroic. *Nature Materials*, **7** (2008) 478.

[25] D. Chiba, M. Yamanouchi, F. Matsukura and H. Ohno. Electrical manipulation of magnetization reversal in a ferromagnetic semiconductor. *Science*, **301** (2003) 943.

[26] H. Ohno, D. Chiba, F. Matsukura, T. Omiya, E. Abe, T. Dietl, Y. Ohno and K. Ohtani. Electric-field control of ferromagnetism. *Nature*, **408** (2000) 944.

[27] E. Y. Tsymbal. Spintronics: Electric toggling of magnets. *Nature Materials*, **11** (2012) 12.

[28] J. Heron, J. Bosse, Q. He, Y. Gao, M. Trassin, L. Ye, J. Clarkson, C. Wang, J. Liu, S. Salahuddin et al. Deterministic switching of ferromagnetism at room temperature using an electric field. *Nature*, **516** (2014) 370.

[29] D. Chiba, S. Fukami, K. Shimamura, N. Ishiwata, K. Kobayashi and T. Ono. Electrical control of the ferromagnetic phase transition in cobalt at room temperature. *Nature Materials*, **10** (2011) 853.

[30] T. Maruyama, Y. Shiota, T. Nozaki, K. Ohta, N. Toda, M. Mizuguchi, A. Tulapurkar, T. Shinjo, M. Shiraishi, S. Mizukami et al. Large voltage-induced magnetic anisotropy change in a few atomic layers of iron. *Nature Nanotechnology*, **4** (2009) 158.

[31] Y. Shiota, T. Nozaki, F. Bonell, S. Murakami, T. Shinjo and Y. Suzuki. Induction of coherent magnetization switching in a few atomic layers of FeCo using voltage pulses. *Nature Materials*, **11** (2012) 39.

[32] A. Ney, T. Kammermeier, V. Ney, K. Ollefs and S. Ye. Limitations of measuring small magnetic signals of samples deposited on a diamagnetic substrate. *Journal of Magnetism and Magnetic Materials*, **320** (2008) 3341.

[33] M. McElfresh. Fundamentals of magnetism and magnetic measurements featuring quantum design's magnetic property measurement system. *Quantum Design*, **11578** (1994) 132.

[34] J. Clarke and A. I. Braginski. *The SQUID Handbook. Vol. 2. Applications of SQUIDs and SQUID Systems.* Wiley-VCH (2006).

[35] H. Warlimont and W. Martienssen. *Springer Handbook of Materials Data.* Springer Handbooks. Springer International Publishing (2018).

[36] P. Pichler. *Electrochemical double-layer charging of nanoporous palladium in Li-ion-based electrolyte.* Bachelor's thesis, Institute of Materials Physics at Graz University of Technology (2018).

[37] L.-l. Fang, Q. Tao, M.-f. Li, L.-w. Liao, D. Chen and Y.-x. Chen. Determination of the real surface area of palladium electrode. *Chinese Journal of Chemical Physics*, **23** (2010) 543.

[38] E. Detsi, E. De Jong, A. Zinchenko, Z. Vuković, I. Vuković, S. Punzhin, K. Loos, G. Ten Brinke, H. De Raedt, P. Onck et al. On the specific surface area of nanoporous materials. *Acta Materialia*, **59** (2011) 7488.

[39] D. Rand and R. Woods. The nature of adsorbed oxygen on rhodium, palladium and gold electrodes. *Journal of Electroanalytical Chemistry and Interfacial Electrochemistry*, **31** (1971) 29.

[40] A. Correia, L. Mascaro, S. Machado and L. Avaca. Active surface area determination of Pd−Si alloys by H-adsorption. *Electrochimica Acta*, **42** (1997) 493.

[41] M. Grdeń, M. Łukaszewski, G. Jerkiewicz and A. Czerwiński. Electrochemical behaviour of palladium electrode: oxidation, electrodissolution and ionic adsorption. *Electrochimica Acta*, **53** (2008) 7583.

[42] I. McCue, E. Benn, B. Gaskey and J. Erlebacher. Dealloying and dealloyed materials. *Annual Review of Materials Research*, **46** (2016) 263.

[43] M. Gößler. *Hydrogen Storage and Actuation Properties of Nanoporous Palladium Prepared by Dealloying.* Master's thesis, Institute of Materials Physics at Graz University of Technology (2017).

[44] Q. Kong, L. Lian, Y. Liu, J. Zhang, L. Wang and W. Feng. Bulk hierarchical nanoporous palladium prepared by dealloying PdAl alloys and its electrochemical properties. *Microporous and Mesoporous Materials*, **208** (2015) 152.

[45] Q. Li, C. W. Kartikowati, S. Horie, T. Ogi, T. Iwaki and K. Okuyama. Correlation between particle size/domain structure and magnetic properties of highly crystalline Fe_3O_4 nanoparticles. *Scientific Reports*, **7** (2017) 9894.

[46] C. Liu and Z. J. Zhang. Size-dependent superparamagnetic properties of Mn spinel ferrite nanoparticles synthesized from reverse micelles. *Chemistry of Materials*, **13** (2001) 2092.

[47] X. He, W. Zhong, C.-T. Au and Y. Du. Size dependence of the magnetic properties of Ni nanoparticles prepared by thermal decomposition method. *Nanoscale Research Letters*, **8** (2013) 446.

[48] T. Sato, T. Iijima, M. Seki and N. Inagaki. Magnetic properties of ultrafine ferrite particles. *Journal of Magnetism and Magnetic Materials*, **65** (1987) 252.

[49] W. Gong, H. Li, Z. Zhao and J. Chen. Ultrafine particles of Fe, Co, and Ni ferromagnetic metals. *Journal of Applied Physics*, **69** (1991) 5119.

[50] M. Hakamada, M. Takahashi, T. Furukawa and M. Mabuchi. Surface effects on saturation magnetization in nanoporous Ni. *Philosophical Magazine*, **90** (2010) 1915.

[51] M. Hakamada, H. Nakano, T. Furukawa, M. Takahashi and M. Mabuchi. Hydrogen storage properties of nanoporous palladium fabricated by dealloying. *The Journal of Physical Chemistry C*, **114** (2009) 868.

[52] A. Hamzić and I. Campbell. The ferromagnetic to spin glass transition. *Journal de Physique Lettres*, **42** (1981) 17.

[53] S. Gubbala, H. Nathani, K. Koizol and R. Misra. Magnetic properties of nanocrystalline Ni−Zn, Zn−Mn, and Ni−Mn ferrites synthesized by reverse micelle technique. *Physica B: Condensed Matter*, **348** (2004) 317.

[54] P. Joy, P. A. Kumar and S. Date. The relationship between field-cooled and zero-field-cooled susceptibilities of some ordered magnetic systems. *Journal of Physics: Condensed Matter*, **10** (1998) 11049.

[55] F. Tournus and A. Tamion. Magnetic susceptibility curves of a nanoparticle assembly ii. simulation and analysis of ZFC/FC curves in the case of a magnetic anisotropy energy distribution. *Journal of Magnetism and Magnetic Materials*, **323** (2011) 1118.

[56] A. F. Gross, M. R. Diehl, K. C. Beverly, E. K. Richman and S. H. Tolbert. Controlling magnetic coupling between cobalt nanoparticles through nanoscale confinement in hexagonal mesoporous silica. *The Journal of Physical Chemistry B*, **107** (2003) 5475.

[57] S. Oyarzún, A. Tamion, F. Tournus, V. Dupuis and M. Hillenkamp. Size effects in the magnetic anisotropy of embedded cobalt nanoparticles: from shape to surface. *Scientific Reports*, **5** (2015) 14749.

[58] C. Teodorescu and G. Lungu. Band ferromagnetism in systems of variable dimensionality. *J. Optoelectron. Adv. Mat*, **10** (2008) 3058.

[59] F. Mueller, A. J. Freeman, J. Dimmock and A. Furdyna. Electronic structure of palladium. *Physical Review B*, **1** (1970) 4617.

[60] A. H. MacDonald, J. Daams, S. Vosko and D. D. Koelling. Influence of relativistic contributions to the effective potential on the electronic structure of Pd and Pt. *Physical Review B*, **23** (1981) 6377.

[61] Y. Sun, J. D. Burton and E. Y. Tsymbal. Electrically driven magnetism on a Pd thin film. *Physical Review B*, **81** (2010) 064413.

[62] Y. B. Kudasov and A. Korshunov. Surface ferromagnetism of palladium induced by strong electric field. *Physics Letters A*, **364** (2007) 348.

[63] A. Mishra, C. Bansal, M. Ghafari, R. Kruk and H. Hahn. Tuning properties of nanoporous Au−Fe alloys by electrochemically induced surface charge variations. *Physical Review B*, **81** (2010) 155452.

[64] J. Coey, M. Viret and S. Von Molnar. Mixed-valence manganites. *Advances in Physics*, **48** (1999) 167.

[65] C. Ahn, A. Bhattacharya, M. Di Ventra, J. N. Eckstein, C. D. Frisbie, M. Gershenson, A. Goldman, I. Inoue, J. Mannhart, A. J. Millis et al. Electrostatic modification of novel materials. *Reviews of Modern Physics*, **78** (2006) 1185.

[66] J. Weissmüller, R. Viswanath, D. Kramer, P. Zimmer, R. Würschum and H. Gleiter. Charge-induced reversible strain in a metal. *Science*, **300** (2003) 312.

[67] R. Viswanath, D. Kramer and J. Weissmüller. Variation of the surface stress-charge coefficient of platinum with electrolyte concentration. *Langmuir*, **21** (2005) 4604.

[68] D. Kramer, R. N. Viswanath and J. Weissmüller. Surface-stress induced macroscopic bending of nanoporous gold cantilevers. *Nano Letters*, **4** (2004) 793.

[69] J. Biener, A. Wittstock, L. Zepeda-Ruiz, M. Biener, V. Zielasek, D. Kramer, R. Viswanath, J. Weissmüller, M. Bäumer and A. Hamza. Surface-chemistry-driven actuation in nanoporous gold. *Nature Materials*, **8** (2009) 47.

[70] Y. Umeno, C. Elsässer, B. Meyer, P. Gumbsch and J. Weissmüller. Reversible relaxation at charged metal surfaces: An ab initio study. *Europhysics Letters*, **84** (2008) 13002.

[71] S. Subkow and M. Fähnle. Potential explanation of charge response of magnetization in nanoporous systems. *Physical Review B*, **84** (2011) 220409.

[72] T. Yamada, K. Morita, K. Kume, H. Yoshikawa and K. Awaga. The solid-state electrochemical reduction process of magnetite in Li batteries: In situ magnetic measurements toward electrochemical magnets. *Journal of Materials Chemistry C*, **2** (2014) 5183.

[73] S. Dasgupta, B. Das, Q. Li, D. Wang, T. T. Baby, S. Indris, M. Knapp, H. Ehrenberg, K. Fink, R. Kruk et al. Toward on-and-off magnetism: Reversible electrochemistry to control magnetic phase transitions in spinel ferrites. *Advanced Functional Materials*, **26** (2016) 7507.

[74] Q. Zhang, X. Luo, L. Wang, L. Zhang, B. Khalid, J. Gong and H. Wu. Lithium-ion battery cycling for magnetism control. *Nano letters*, **16** (2016) 583.

[75] S. Kaprzyk, A. Maksymowicz and K. Zakrzewska. Calculations of electron spin polarization in PdCo alloys by KKR-CPA-LSD method. *Journal of Magnetism and Magnetic Materials*, **104** (1992) 2019.

[76] H. Ebert, A. Vernes and J. Banhart. Anisotropic electrical resistivity of ferromagnetic Co−Pd and Co−Pt alloys. *Physical Review B*, **54** (1996) 8479.

[77] J. N. Neal, D. J. Wesolowski, D. Henderson and J. Wu. Electric double layer capacitance for ionic liquids in nanoporous electrodes: Effects of pore size and ion composition. *Journal of Molecular Liquids*, **270** (2018) 145.

[78] A. Berthod, J. J. Kozak, J. L. Anderson, J. Ding and D. W. Armstrong. Ionic liquid-alkane association in dilute solutions. *Theoretical Chemistry Accounts*, **117** (2007) 127.

[79] Y. Marcus. Volumes of aqueous hydrogen and hydroxide ions at 0 to 200 °C. *The Journal of Chemical Physics*, **137** (2012) 154501.

Acknowledgement

At this point, I would like to sincerely thank the following people which contributed to the success of this thesis.

Univ.-Prof. Dr. Roland Würschum, Institute of Materials Physics, TU Graz
For the opportunity to write my thesis on the institute, for supervising the project and for his advice in academic research.

Univ.-Prof.i.R. Dr. Heinz Krenn, Institute of Physics, University of Graz
For the possibility to perform magnetisation measurements in the SQUID laboratory and for his assistance and advice, which helped in understanding complex subjects.

Ao.Univ.-Prof. Dr. Roland Resel, Institute of Solid State Physics, TU Graz
For the use of the XRF.

Dipl.-Ing. Markus Gößler, Institute of Materials Physics, TU Graz
For co-supervising this thesis and his assistance, guiding and advice during the whole work. For several discussion and suggestions which strongly improved this work and my knowledge about underlying subjects.

My colleagues at the Institute of Materials Physics, TU Graz
For the pleasant working environment and several coffee breaks.

My family and friends